BIOCHEMICAL CHARACTERIZATIONS OF NICASTRIN, BARIUM BLOCKAGE OF POTASSIUM CHANNELS AND CALCIUM BLOCKAGE OF CYCLIC NUCLEOTIDE-GATED CHANNELS

APPROVED BY SUPERVISORY COMMITTEE

_____

Youxing Jiang, Ph.D.

_____

Daniel Rosenbaum, Ph.D.

_____

Chad Brautigam, Ph.D.

_____

Jose Rizo-Rey, Ph.D.

_____

Gang Yu, Ph.D.

To my family, Grace, Keung and Yee Chuen Lam and my husband Ruddie Chau who encouraged and supported me throughout this journey.

BIOCHEMICAL CHARACTERIZATIONS OF NICASTRIN, BARIUM BLOCKAGE OF POTASSIUM CHANNELS AND CALCIUM BLOCKAGE OF CYCLIC NUCLEOTIDE-GATED CHANNELS

by

YEE LING LAM

DISSERTATION

Presented to the Faculty of the Graduate School of Biomedical Sciences

The University of Texas Southwestern Medical Center at Dallas

In Partial Fulfillment of the Requirements

For the Degree of

DOCTOR OF PHILOSOPHY

The University of Texas Southwestern Medical Center

Dallas, Texas

August, 2015

BIOCHEMICAL CHARACTERIZATIONS OF NICASTRIN, BARIUM BLOCKAGE OF POTASSIUM CHANNELS AND CALCIUM BLOCKAGE OF CYCLIC NUCLEOTIDE-GATED CHANNELS

YEE LING LAM, Ph.D.

The University of Texas Southwestern Medical Center at Dallas, 2015

YOUXING JIANG, Ph.D.

This dissertation is divided into three independent chapters dedicated to research work in biochemical characterizations of nicastrin, barium blockage of potassium channels and calcium blockage of cyclic nucleotide-gated channels. The first chapter describes studies on an intramembrane protease called γ-secretase. This protease complex is known to generate the pathogenic peptide species in Alzheimer's disease, a neurodegenerative disease affecting billions around the

globe. In particular, the study focused on understanding one subunit of the protease complex, the substrate receptor nicastrin. While the ultimate goal of crystallizing nicastrin was not achieved, the purification processes have revealed that glycosylation is important for folding or trafficking of the protein and disulfide bonds are crucial to maintain the tertiary structure of nicastrin. The second chapter focuses on a classic blocking phenomenon in potassium channels known as barium blocking. Previous studies on barium blocking have fueled our understanding on the ion conduction pore of potassium channels. A model of blockage has been proposed but has yet to be proven. This study recapitulated properties of barium blocking in the potassium channel NaK2K and provided structural evidence for the model of barium block. The crystal structure of NaK2K in the presence of sodium and barium showed a barium-binding pattern different from that of a structure in the presence of potassium and barium. The difference in binding explains the different blocking behaviors in the presence and absence of low concentrations of external potassium. The third chapter details a study on the weak calcium block of monovalent ion current in *Drosophila* cyclic nucleotide-gated (CNG) channel. Calcium blockage in the CNG channel arises from preferential but slow conduction of calcium. This blocking phenomenon is observed in all CNG channels, but to various extents. In this study, a threonine immediately outside of the selectivity filter was found to modulate the calcium block of *Drosophila* CNG channels, likely by causing the channel to adopt a

selectivity filter structure different from canonical CNG channels. This threonine is unique to the CNG channels of *Drosophila* and a few insects, whereas most other CNG channels have a proline at the equivalent position. These findings have allowed us to identify a structure-function relationship for calcium blockage in *Drosophila* CNG channels.

TABLE OF CONTENTS

PRIOR PUBLICATIONS

Lam, Y.L., Zeng, W., Derebe, M., Jiang, Y. 2015. Structural implications of weak Ca2+ block in Drosophila cyclic nucleotide-gated channels. *The Journal of general physiology. In press.*

Lam, Y.L., Zeng, W. Sauer, D.B., Jiang, Y. 2014. The conserved potassium channel filter can have distinct ion binding profiles: structural analysis of rubidium, cesium, and barium binding in NaK2K. *The Journal of general physiology.* 144:181-192

Deng, M., Lu, Z., Zheng, J., Wan, X., Chen, X., Hirayasu, K., Sun, H., Lam, Y., Chen, L., Wang, Q., Song, C., Huang, N., Gao, G.F., Jiang, Y., Arase, H., Zhang, C.C. 2014. A motif in LILRB2 critical for Angptl2 binding and activation. *Blood*. 124:924-935

Sauer, D.B., Zeng, W., Canty, J., Lam, Y., Jiang, Y. 2013. Sodium and potassium competition in potassium-selective and non-selective channels. *Nature communications*. 4:2721.

Kong, C., Zeng, W., Ye, S., Chen, L., Sauer, D.B., Lam, Y., Derebe, M.G., Jiang, Y. 2012. Distinct gating mechanisms revealed by the structures of a multi-ligand gated K(+) channel. *eLife*. 1:e00184.

LIST OF FIGURES

LIST OF TABLES

LIST OF ABBREVIATIONS

ADAM	A disintegrin and metalloprotease
APP	Amyloid precursor protein
Aph-1	Anterior pharynx defective-1
cAMP	3',5'-cyclic adenosine monophosphate
cGMP	3',5'- cyclic guanosine monophosphate
CNBD	Cyclic nucleotide-binding domain
CNG	Cyclic nucleotide-gated
DM	n-decyl-β-D-maltoside
DTT	Dithiothreitol
EDTA	Ethylenediaminetetraacetic acid
EGTA	Ethylene glycol tetraacetic acid
ELISA	Enzyme-linked immunosorbent assay
EM	Electron microscopy
ER	Endoplasmic reticulum
FAD	Familial Alzheimer's disease
HPLC	High performance liquid chromatography
IPTG	β-D-1-thiogalactopyranoside
IgG	Immunoglobulin G
LB	Luria-Bertani

MES	2-(N-morpholino)ethanesulfonic acid
MPD	(±)-2-methyl-2,4-pentanediol
NMR	Nuclear magnetic resonance
NicD	Notch intercellular domain
OD	Optical density
OHSU	Oregon Health and Science University
PEN-2	Presenilin enhancer 2
POPE	1-palmitoyl-2-oleoyl-phosphatidylethanolamine
POPG	1-palmitoyl-2-oleoyl-phosphatidylglycerol
PSEN	Presenilin
RMSD	Root-mean-square deviation
S2P	Site-2 protease
SDS-PAGE	Sodium dodecyl sulphate-polyacrylamide gel electrophoresis
SPP	Signal peptide peptidase
SREBP	Sterol-regulatory element-binding proteins
TBA	Tetrabutylammonium
TCEP	Tris(2-Carboxyethyl) phosphine
TM	Transmembrane span
TPeA	Tetrapentyl ammonium
β-ME	β-mercaptomethanol

CHAPTER 1

BIOCHEMICAL CHARACTERIZATIONS OF NICASTRIN

A. Summary

Nicastrin is a component of the heterotetrameric intramembrane protease complex γ-secretase. Like other intramembrane proteases, γ-secretase is capable of cleaving transmembrane helices within the membrane and releasing the digestion products out of the membrane. Proteolysis of γ-secretase is carried out by the catalytic core presenilin but assisted by the other three components, Aph-1, Pen-2 and nicastrin. Nicastrin has a large extracellular domain that can interact with substrates of γ-secretase. The interaction has led researchers to speculate that nicastrin is the substrate receptor of the protease complex. In order to further our understanding of nicastrin, this project was undertaken to determine the crystal structure of nicastrin. Human nicastrin extracellular domain was expressed in insect cells and purified for crystallization trials. However, nicastrin did not crystallize as hoped. To improve the homogeneity of the purified protein, deglycosylation assays and limited proteolysis were performed. Since purified nicastrin was found to both degrade and aggregate over time, protease inhibitor and reducing agents were used in attempts to slow down both events. Antibodies against nicastrin were also generated to find a stabilized nicastrin-fab complex suitable for crystallization. Although none of the strategies has led to the

crystallization of human nicastrin, the results have provided insights into various biochemical properties of nicastrin, such as the importance of glycosylations and disulfide bonds.

B. Literature review

1. Intramembrane proteases

Regulated intramembrane proteolysis is a crucial process for various signal transduction and metabolic pathways. Initially discovered in the sterol regulatory pathway (Brown and Goldstein, 1997), the idea of hydrolytic proteolysis occurring inside the hydrophobic membrane environment was not well received until several transmembrane proteases were independently identified (Brown et al., 2000). We now know of intramembrane proteases from all kingdoms of life, from bacteria to humans (Urban, 2009) (Figure 1). Although their cellular functions are very diverse, they share several common features. First, prior to intramembrane proteolysis, most substrates are first subjected to a proteolytic cleavage at the extracellular juxtamembrane region. This process, termed shedding, separates the extracellular domain (also known as ectodomain) from its transmembrane helix, so that the helix becomes a substrate of intramembrane proteases. Sheddings are almost always carried out by transmembrane proteases with active site in the extracellular domain (Brown et al., 2000). Second, all substrates of intramembrane proteases are single–span helices. Nonetheless, each kind of protease can only cleave either type I or type II transmembrane helices. Third, there is little sequence specificity on intramembrane protease cleavage, but most proteases cleave at a position harboring residues with low helical propensity

(Lemberg and Freeman, 2007). Besides these three common features, intramembrane proteases come in all shapes and forms. Some are stand-alone with a single domain, while others have multiple domains or even exist as a protein complex. Intramembrane proteases are categorized into three classes based on their proteolytic mechanisms: serine, aspartyl and metallo- proteases. They utilize proteolytic mechanisms similar to soluble proteases, as indicated by the name of their categories. Below is a brief description of each mechanistic class of intramembrane protease and our current understanding on the proteases.

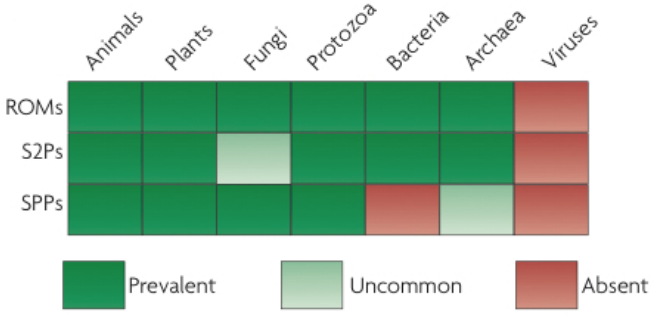

Figure 1. Prevalence of intramembrane proteases (Adapted from Urban, 2009). Romboid (ROM) and Site 2 protease (S2P) can be found in all kingdoms of life except for viruses. Signal peptide peptidase (SPP) is prevalent only in eukaryotes with few homologs in Achaea.

a. Intramembrane serine protease

Intramembrane serine protease, also known as rhomboid, severs peptide bonds by using serine as a nucleophile and histidine or lysine as a general base. Initially

discovered in *Drosophila*, rhomboid was found to liberate a key ligand for the epidermal growth receptor from the membrane (Urban, 2009). Malaria and related parasites use rhomboid to cleave adhesins in one of the steps of host invasion. To date, more than nine crystal structures of rhomboid from bacteria have been determined (Wang et al., 2006; Wu et al., 2006; Ben-Shem et al., 2007; Lemieux et al., 2007; Wang and Ha, 2007). These structures reveal that the catalytic core is embedded deep inside the protease, implying that the proteolysis indeed takes place inside the membrane (Figure 2 A, top). The active site of the protease has an opening towards the periplasm, which is suggested to allow water to access for the proteolytic hydrolysis (Lemberg and Freeman, 2007) (Figure 2 A, bottom). The gating mechanism of the protease was subjected to debate for some time, but a combination of structural and mutational analysis suggests that helix five is the mostly likely gate for the protease (Baker et al., 2007; Lemberg and Freeman, 2007; Brooks et al., 2011). Rhomboid is currently the best understood class of intramembrane protease.

b. Intramembrane metallo-protease

Intramembrane metallo-protease is often called site-2-protease (S2P). It has a signature sequence of HExxH in its transmembrane domain, which coordinates the zinc ion essential to the proteolysis. S2P was the first intramembrane protease to be discovered. It was first identified in the sterol-regulatory element-binding

proteins (SREBP), and S2P cleaves the membrane-bound transcription factor for cholesterol metabolism (Brown et al., 2000). S2P is functionally diverse. In the opportunistic pathogen *Pseudomonas aeruginosa*, intramembrane metallo-protease, MucP, processes a protein responsible for antibiotic resistance (Urban, 2009). The functions of S2P in *Escherichia coli* and *Bacillus subtilis* are also well characterized (Kroos and Akiyama, 2013). Functional studies of S2P from different species have revealed a common theme in that the activities of S2P are in general tightly regulated. All substrates of S2P have their extracellular domain shedded by metalloprotease, ADAM, before they are subjected to S2P cleavage. As an additional layer of regulation, most S2P's have a PDZ domain that regulates their activity, likely by binding to the C-terminus of a substrate. The crystal structure of the proteolytic core of S2P from *Methanocaldococcus jannaschii* (Feng et al., 2007) (Figure 2 B) shows that S2P has a channel that connects the cytosol and the active site to allow entrance of water for the hydrolytic proteolysis (Kroos and Akiyama, 2013) (Figure 2 B, bottom). The water molecule used in the catalytic reaction is thought to be coordinated by the glutamate residue in the signature sequence HExxH. While the structure of the catalytic core has provided insights on the catalytic mechanism, some of the fundamental properties of the enzyme such as the gating mechanism and substrate specificity are still under active research.

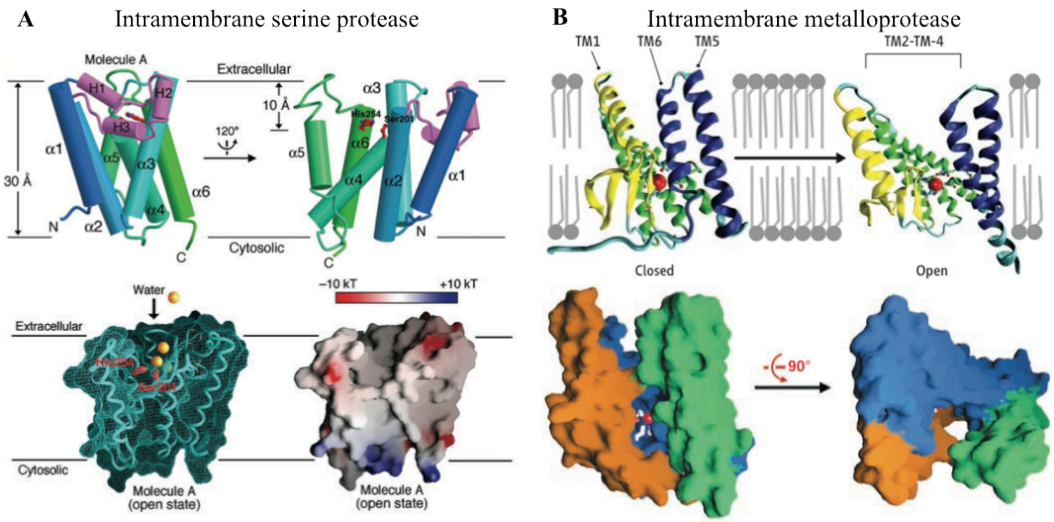

Figure 2. Crystal structures of intramembrane serine protease and metalloprotease. (A) *Top* Overall arrangement of transmembrane helices of *Escherichia coli* intramembrane serine protease, GlpG (Adapted from Wu et al., 2006). Residues involved in catalysis are shown as red sticks. *Bottom* Surface representation of the structure showing how water can access the catalytic core. (B) *Top* Overall arrangement of the open and closed state of *Methanocaldococcus jannaschii* intramembrane metalloprotease (Adapted from Feng et al., 2007). *Bottom* Surface representation of the structure in open state showing how water can access the catalytic core.

c. Intramembrane aspartyl protease

Intramembrane aspartyl protease is characterized by a GxGD motif and consists of two sub-families of protease, signal peptide peptidase (SPP) and γ-secretase.

SPP localizes to the endoplasmic reticulum (ER) and degrades signal peptides, releasing them from the membrane. Like S2P, the proteolytic cleavage of SPP is a secondary cleavage. Preceding the proteolysis by SPP, signal peptidase cleaves off the luminal domains of substrates of SPP, leaving a type II single transmembrane helix of signal peptide for SPP cleavage. With some exceptions, most products of SPP have no known downstream function. It is thought that cleavages of SPP release signal peptides from the membrane and allow them to be degraded and recycled. There is currently one structure of intramembrane aspartyl protease from archaebacteria, but it is not clear whether this protease is more closely related to SPP or the catalytic core of γ-secretase. Details of the structure will be discussed in section 2.c.i below together with other structural information about γ-secretase. The other member of the intramembrane aspartyl proteases, γ-secretase, has been intensively studied and is well known for its role in generating the pathogenic peptide species in Alzheimer's disease. γ-secretase localizes to the plasma membrane and cleaves exclusively type I transmembrane helices. Multiple cryo-electron microscopy (cryo-EM) structures of γ-secretase have been determined, with one of them having a near-atomic resolution (Lazarov et al., 2006; Osenkowski et al., 2009; Lu et al., 2014). The structure provided the overall shape and architecture of the enzyme but lacked molecular details that can lead to mechanistic models. Since γ-secretase is a major focus of the research described

in this chapter, the next section will be devoted to additional literature review of the enzyme.

2. γ-secretase

a. Functions

i. Amyloid precursor protein processing

Alzheimer's disease is the most common age-associated neurodegeneration. In 2015, an estimated 5.3 millions Americans suffered from Alzheimer's disease, and it is the 6th leading cause of death in the United States (Statistics from Alzheimer's association). One of the neuropathological hallmarks of Alzheimer's disease patients is the presence of senile plaques in their brains. These amyloid plaques are mainly fibrillar aggregation of a 42 amino acid long peptide called Aβ42. Aβ42 originates from amyloid precursor protein (APP), and γ-secretase plays a key role in the processing of APP that leads to Aβ42. In humans, APP can undergo two different processing pathways. In one pathway, APP is subjected to cleavage by α-secretase at the juxtamembrane region and a subsequent cleavage by γ-secretase. The first cut sheds the ectodomain of APP, while the second cut generates peptides that are not aggregation prone. In the alternative pathway, β-secretase takes the lead to shed the ectodomain of APP by cleaving at a site N-terminal to the α-secretase cleavage site, and the product is processed by γ-secretase to generate peptides that are 37-43 amino acids in length. The 42-

residue peptide, Aβ42, is the most neurotoxic and aggregation-prone species. Mutations in γ-secretase can alter the cleavage-site preference of the enzyme, generating more Aβ42.

ii. Notch Signaling

Notch signaling pathway is central to cell differentiation and development. Although there are a lot of interests in developing molecules that can inhibit γ-secretase to relieve Alzheimer's disease, this strategy has limited success because inhibitors of γ-secretase tend to interrupt Notch signaling and cause significant side effects. The basic framework of notch signaling is straightforward, but the effects and signals vary in different tissues and different organisms. Both notch receptors and ligands are transmembrane proteins with an extracellular domain localized on plasma membrane (Bray, 2006). When a ligand binds to a notch receptor on the neighboring cell, the notch receptor undergoes a conformational change that allows transmembrane protease ADAM to cleave off the extracellular ligand-binding domain. After shedding of the ectodomain, γ-secretase makes a second cleavage at the transmembrane region, releasing the Notch intercellular domain (NicD) from the membrane. The released NicD translocates to the nucleus and interacts with transcription factors to alter gene expression patterns that determine the cell fate.

iii. Others

To date, more than 90 different substrates of γ-secretase have been identified (Haapasalo and Kovacs, 2011). In addition to APP processing and cell-cell communication, the enzyme has been implicated to in a wide range of biological processes. For example, in neuronal cells, Netrin-1 is an early guidance cue for proper positioning of synaptic connections. As the development passes the early stage and crosses the midline, Netrin receptors must be processed by γ-secretase, so that the axon becomes insensitive to Netrin-1 and sensitive to other guidance cues. Temporally and spatially accurate cleavage of Netrin receptors by γ-secretase is crucial for early stage of axon guidance (Jurisch-Yaksi et al., 2013). From the Netrin receptor in axon guidance to the notch receptor in T-cell development, the substrates of γ-secretase imply the enzyme's involvements in such a wide spectrum of vital physiological processes that the protease is now often regarded as a general protease for degradation or release of transmembrane helices from the membrane (Jurisch-Yaksi et al., 2013).

b. Biochemical properties

Unique to all other intramembrane proteases, γ-secretase is a protein complex consists of four subunits in 1:1:1:1 stoichiometry (De Strooper, 2003). The four proteins and their biochemical and functional properties will be described below.

i. Anterior pharynx defective-1 (Aph-1)

Aph-1 has two homologs in humans, Aph-1a and Aph-1b. Aph-1a has in two splice variants, Aph-1aL (long variant) and Aph-1aS (short variant). All three isoforms of Aph-1 were found in γ-secretase complex and are thought be functionally redundant (Shirotani et al., 2004). Although Aph-1 is indispensable for γ-secretase function, the precise role of the protein has yet to be clearly defined. Aph-1 is predicted to have seven transmembrane helices. Several highly conserved residues, including the motif GxxxG in the 4th transmembrane helix as well as residues 82, 83, 97, 171 and 191, are found to be critical for the assembly or activity of γ-secretase (Niimura et al., 2005; Pardossi-Piquard et al., 2009; Chiang et al., 2012). Many of these residues interact with nicastrin, and the two proteins are known to form stable sub-complex *in vivo*. With the limited functional and biochemical characterizations, Aph-1 has been postulated to be a stabilizing scaffold in the assembly of the protease complex (Niimura et al., 2005).

ii. Nicastrin (NCT)

Nicastrin is the largest component of γ-secretase. It comprises of an extracellular domain, one transmembrane helix and a small cytosolic domain. Part of the extracellular domain resembles a peptidase, but it does not exhibit any peptidase activity. One remarkable feature of nicastrin is that it has 15 N-linked glycosylation sites. A mature γ-secretase complex always consists of a nicastrin

with complex glycosylation (Kimberly et al., 2002), even though the glycosylation is found to be important only for the folding and trafficking of nicastrin but not the proteolytic activity of the protease complex (Herreman et al., 2003). Despite being somewhat controversial, nicastrin has been proposed to be the substrate receptor of γ-secretase (Shah et al., 2005). The extracellular domain is thought to participate in substrate selection by preventing other transmembrane proteins with ectodomains from approaching the protease. Glu 333 has been shown to interact with the free N-terminus of the substrate in type I orientation and plays a key role in substrate recognition. In addition, nicastrin can adapt more than one conformations, termed mature and immature conformation. The two conformations adopt different combinations of disulfide bonds. Active γ-secretase complex consists only of nicastrin in its mature confirmation and is resistant to trypsin digestions.

iii. Presenilin (PSEN)

PSEN is the catalytic core of γ-secretase and the only subunit with proteolytic activity. More than 150 mutations that are found in familial Alzheimer's disease (FAD) patients are mapped to PSEN (Alzheimer Disease & Frontotemporal Dementia Mutation Database), and many of these mutations cause γ-secretase to preferentially generate the aggregation-prone Aβ42. PSEN has two homologs, PSEN-1 and PSEN-2. They share 67% sequence identity and are functionally

redundant (Lai et al., 2003). PSEN is predicted to have 9 transmembrane helices. As the proteolytic core, it has the signature motif of aspartyl intramembrane protease GxGD, as well as both the aspartate residues key to proteolytic cleavage, so presenilin alone has the full enzymatic potential for proteolysis. However, full-length intact presenilin is a zymogen. As part of the maturation process of γ-secretase, PSEN must undergo endoproteolysis, i.e. it catalyzes a self-proteolytic cleavage. The endoproteolysis cleaves PSEN at a loop region between TM 6 and TM 7, and the two halves, termed N-terminal fragment (NTF) and C-terminal fragment (CTF), form a heterodimer that is proteolytically active.

iv. Presenilin enhancer 2 (PEN-2)

PEN-2 is the smallest subunit in γ-secretase having only two transmembrane spans. Its primary role is to facilitate the endoproteolysis of PSEN such that it converts to its enzymatically active state. Some recent studies suggest that PEN-2 is also important for the stability of the γ-secretase complex and its enzymatic activity (Holmes et al., 2014). Mutation studies have shown that the C-terminal region of PEN-2, in particular the DYLSF motif, appears to be critical for γ-secretase assembly (Hasegawa et al., 2004).

v. Assembly of the protein complex.

The assembly of γ-secretase is sequential and tightly regulated. Nicastrin and Aph-1 first form a stable sub-complex (LaVoie et al., 2003). PSEN then binds to nicastrin-Aph-1 sub-complex, and the trimer subsequently recruits PEN-2. The incorporation of PEN-2 triggers endoproteolysis of PSEN, which is the final maturation step. With the requirements of subcomplex formation, glycosylation and endoproteolysis, the biogenesis of γ-secretase is subjected to many layers of regulations. The three isoforms of Aph-1 and two homologs of PSEN render six possible combinations of γ-secretase complex. Although all the isoforms are considered functionally redundant, their expression levels vary and show different phenotypes when they are knocked down, suggesting that the genes are regulated by different factors. Therefore, despite its promiscuous nature, γ-secretase activity is controlled by sophisticated regulations of expression and trafficking as well as a carefully orchestrated mechanism of assembly and maturation. It is very possible that γ-secretase is the most tightly regulated intramembrane protease.

c. Structure

As a key player in Alzheimer's disease and notch signaling, structural information of γ-secretase is highly sought-after. To date, there is one nuclear magnetic resonance (NMR) structure of PSEN-CTF (Sobhanifar et al., 2010), one 1.95 Å crystal structure of nicastrin, one 3.3 Å crystal structure of an archaeal

intramembrane aspartyl protease (Li et al., 2013), one cyro-EM structure of γ-secretase with near atomic resolution (Lu et al., 2014), and multiple low-resolution EM structures of γ-secretase (Lazarov et al., 2006; Osenkowski et al., 2009; Renzi et al., 2011). All these structures together have provided some valuable information of γ-secretase.

i. Structure of PSEN-CTF and bacterial intramembrane aspartyl protease

A structure of human PSEN-CTF was obtained through NMR in sodium dodecyl sulfate (SDS) micelles (Sobhanifar et al., 2010). The structure shows one long helix as helix 8 and multiple shorter helices separated by loops (Figure 3 A). The overall topology of this NMR structure is similar to the crystal structure of the archaebacteria homolog of intramembrane aspartyl protease from *Methanoculleus marisnigri*, named PSH as in PSEN/SPP homolog. Nonetheless, the conformations that the two proteins adopt are significantly different (Li et al., 2013). PSH has nine transmembrane helices that are long enough to traverse the lipid bilayers and has no short helices like the human PSEN-CTF NMR structure (Figure 3 B). The active site of PSH has channel open to the surface of the protein, which presumably allows water to enter the active site for catalysis (Figure 3 B, lower right). This observation is consistent with that of the other intramembrane proteases. Although PSH contains all signature motifs characteristics of the protease family and shares a relatively high sequence homology with PSEN and

SPP, it has only been shown to cleave substrates of a rhomboid, which is an intramembrane serine protease. Neither does PSH require any cofactor for its proteolytic cleavage like presenilin. While PSH probably uses the same catalytic mechanism as PSEN and SPP, it is unclear how well PSH can model the functionality of SPP and PSEN.

ii. Structure of nicastrin

In 2014, a 1.95 Å crystal structure of a nicastrin homolog from *Dictyostelium purpureum* gave the first glimpse of the extracellular domain of nicastrin (Xie et al., 2014). It shows that the extracellular domain of nicastrin has a large lobe and a small lobe, and the two lobes are linked through hydrophobic interactions (Figure 3 C). A pocket found in the large lobe is speculated to be a substrate-binding site because it is positioned in a similar manner as the active site of a bacterial aminopeptidase, which share some homology with nicastrin (Xie et al., 2014). Residues that are previously found to interact with substrate are also in this pocket, such as Glu 289, which corresponds to Glu 333 in human nicastrin, and Tyr 293, which corresponds to Tyr 337 in human nicastrin (Shah et al., 2005; Dries et al., 2009; Xie et al., 2014). Even though DpNCT may be a distant homolog of nicastrin, its structure shows features that are consistent with previous biochemical findings on human nicastrin, suggesting that it may be a good functional model for human nicastrin for further structural analysis.

iii. EM structures of γ-secretase

As discussed section 2.b.iv., the trafficking, maturation and assembly of γ-secretase are regulated by a multitude of factors. The protein complex cannot be expressed in high quantity even in an over-expression system, making crystallization of protein complex relatively difficult. Cryo-electron microscopy, which requires much less protein sample for structure determination, is an attractive alternative. With the recent advances in the detection techniques and data analysis of cryo-electron microscopy, obtaining a high-resolution structure of γ-secretase becomes a viable option. A near atomic 4.5 Å cryo-EM structure was published in 2014 (Lu et al., 2014), and this was preceded by several low-resolution structures presented in the past (Lazarov et al., 2006; Ogura et al., 2006; Osenkowski et al., 2009). Only the 4.5 Å structure will be discussed here since it provides the most information for structural analysis. The transmembrane domain of γ-secretase takes a horseshoe shape, with the extracellular domain of nicastrin on top of the hollow space of the horseshoe (Figure 3 D). 19 helical TMs of various lengths are observed in the structure, although it is not yet possible to assign the helices to different components of the protein complex (Figure 3 D). The crystal structure of extracellular domain of nicastrin from *D. purpureum* docked well into the density in the extracellular domain of the cryo-EM structure

(Lu et al., 2014), partially validating the accuracy of the near-atomic cryo-EM structure of γ-secretase.

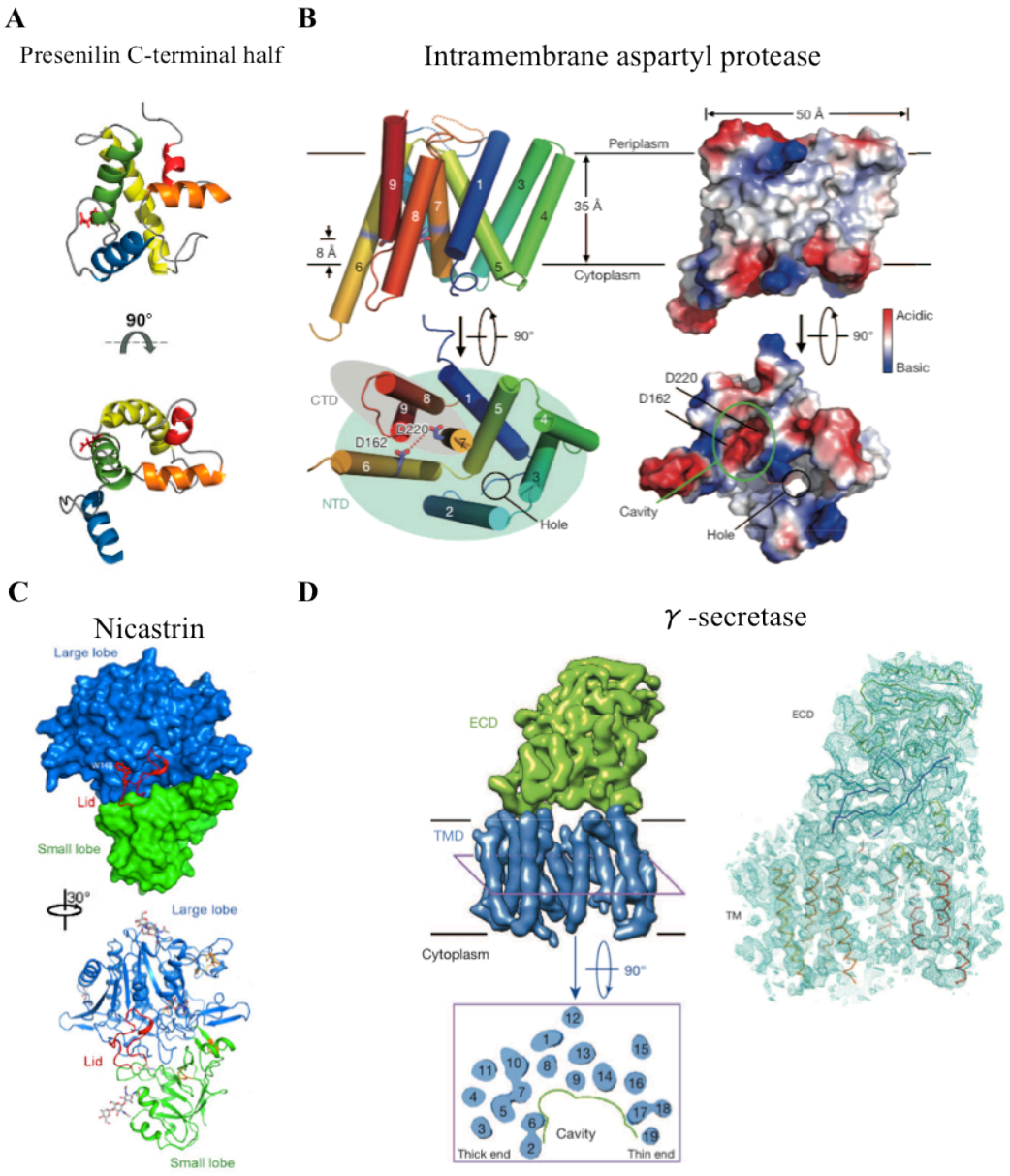

Figure 3. Structures of γ-secretase, its homologs and components. (A) Overall arrangement of human presenilin C-terminal domain (Sobhanifar et al., 2010). (B) *Left* Overall structure of intramembrane aspartyl protease from *Methanoculleus marisnigri* (PSH) (Li et al., 2013). *Right* Surface representation of the structure with the catalytic residues and opening for water access labeled. (C) Structure of nicastrin shown in surface and cartoon representation (Xie et al., 2014). The large loop and small loop are colored in blue and green respectively. (D) *Left* Shape of γ-secretase in surface representation. The transmembrane domains of the complex arrange in a horseshoe shape. *Right* Electron density of γ-secretase fitted with secondary structural elements (Lu et al., 2014).

C. Methodology

1. Overall goal and strategy

The project is an initial phase of a long-term goal in the laboratory to understand the structural basis of γ-secretase function and regulation. Among all the different components and domains in γ-secretase, the substrate receptor nicastrin appears to be the most attractive crystallographic target. Nicastrin comprises a large extracellular domain, a single transmembrane span and a short cytosolic domain. The large soluble domain is expected to be easier to purify and handle compared to the transmembrane domain in the other components. The goal of this project was to prepare a homogenous and pure nicastrin in large quantities for crystallization screening. Described below are the methods used in the attempt to crystallize the extracellular domain of nicastrin.

2. Cloning and expression

Since much of the function of nicastrin relies on its extracellular domain, efforts were focused to obtain a structure of the extracellular domain. Part of the challenge anticipated for the crystallization of nicastrin is the large number of N-linked glycosylation sites. Hence, an insect cell expression system was selected for its lack of complex glycosylation. The extracellular domain of human nicastrin (residue 1 – 669) was cloned to pFastBac1 vector. A TEV cleavage site, linker and 10-histidine tag for affinity purification were added to the 3' end of the gene.

Bac-to-Bac Baculorvirus Expression (Invitrogen) was used to prepare virus for insect cell expression. First, pFastBac1 plasmid containing nicastrin gene and tag was transformed into DH10Bac cells for a blue and white screen. White colonies contained recombinant bacmid and were amplified. Their DNA's were isolated and transfected into wells of a cell line of *Spodoptera frugiperda*, Sf9. Cellfectin was used as a transfection agent, and the protocol used was from the Bac-to-Bac Baculovirus Expression System user manual from Invitrogen. After transfection, cell were left to grow for 7 days at 27 °C as a monolayer. Seven days later, the media (about 1ml) containing the baculovirus was harvested. These viruses are generally regarded as P1 virus. 500 µl of P1 virus was added to 50 ml of Sf9 cells in suspension, and the cells were incubated in a shaker at 130 rpm at 27 °C for 5-7 days until the cells began to die off, an indication of virus infection. After 5-7 days, cells were centrifuged at 4000 g, and the media was collected as P2 virus stock. At 1: 500 dilution, another 50 ml of cells were infected by P2 virus for 2-3 days until signs of infection appeared. The media was then harvested as P3 virus stock by centrifugation. The P3 virus was stored at 4 °C and wrapped with foil to protect it from light.

To determine the optimal condition for expression, 3 flasks of 50 ml of Sf9 cells were infected in a virus to cell ratio of 1:100, 1: 300 and 1: 600 (v/v). Since the

expressed protein is an extracellular domain, it is secreted to the media during expression. 30 μl of media was collected from each flask every 24 hours for four days. 10 μl of each media sample was mixed with 6x SDS loading buffer for Western blot analysis using α-His antibodies. Based on the result of this experiment, 72 hours of infection in 1:500 virus to cell ratio (v/v) was used for all the subsequent nicastrin expression.

3. Purification

Various strategies have been attempted to purify the secreted nicastrin extracellular domain from the media. They include: affinity purification directly from the media, vacuum-assisted compression of media followed by affinity purification, ion-exchange purification followed by affinity purification and ammonium sulfate precipitation followed by affinity purification. Ultimately, ammonium sulfate precipitation was found to be the most efficient and economical, and, thus, it was adopted to be the primary method for nicastrin purification.

After approximately 72 hours of baculovirus infection, media was harvested by centrifugation at 4000 g for 10 minute. The media was then transferred to 4 °C. Ammonium precipitation began with 30% saturation to remove non-nicastrin proteins, followed by a 70% saturation that precipitated nicastrin. 170 g/L of

$(NH4)_2SO_4$ was added to the media and stirred for 30 minutes at 4 °C. The salted media was then centrifuged at 11,000 g for 40 minutes at 4 °C. Pellet were discarded and 257 g/L of $(NH4)_2SO_4$ was added to the supernatant to reach 70 % saturation. When all the added salt dissolved, the salted media was stirred for 1 hour before being centrifuged at 11,000 g for 45 – 60 minutes. Pellets were resuspended in buffer A (50 mM NaCl, 50 mM Tris pH 8, 5 % glycerol) and the resuspended pellet was stirred in 4 °C for 30 minutes to wait for the pellet to be completely dissolved. The resuspended pellet was then subjected to another centrifugation at 15,000 rpm for 25 minutes to remove the undissolved precipitation. Protease inhibitors, including leupeptin, pepstatin, aprotinin, and PMSF (Sigma), were added to the supernatant of the centrifugaton. During the centrifugation, 1 ml of Qiagen Ni-NTA affinity resin per liter of media was equilibrated with buffer B (200 mM NaCl and 50 mM Tris pH 8). The supernatant from the centrifugation was mixed with the equilibrated resin at 4 °C and gently agitated for about 60 minutes. After batch binding, the sample was centrifuged at 1000 g for 10 min. The supernatant was carefully removed and about 40 ml of buffer B (200 mM NaCl and 50 mM Tris pH 8) was added to resuspend the pelleted resin. The resuspended resin was centrifuged in 1000 g for 10 minutes and the supernatant was carefully removed. The same wash was repeated three more times. After the fourth wash, small amount of buffer B (about 10ml) was added to resuspend the resin, and the slurry was transferred to a gravity column

that was connected to a ultra-violet (UV) spectrometer. On the gravity column, the resin was washed with about 10 column volumes (CV) of buffer B with 30 mM imidazole or until the UV peak returned to baseline. After the wash, nicastrin was eluted by adding buffer B with 300 mM imidazole. Unless otherwise noted, TEV protease and PNGase F were added to the eluate. The eluate and protease were incubated at room temperature for about 4-5 hours, and then were transferred to a dialysis bag (8 kD cut-off) to be dialyzed overnight in 200 mM NaCl and 20 mM Tris pH 8 in 4 °C.

The next day, 1 ml of Ni-NTA resin was equilibrated in a gravity column with the dialysis buffer. The dialyzed and digested eluate was transferred to the gravity column, and the flow through was collected. Using an Amicon Ultra centrifugal filtration device of 50 kDa molecular mass cut-off, the flow through was concentrated to 500 – 1000 µl. The concentrated protein was then injected into a Superdex 200 10/300 or HiLoad 16/60 column (GE Health Care) that had been equilibrated with 200 mM NaCl and 20 mM Tris pH 8. Monomers of nicastrin eluted at 13 – 15 ml. Purified nicastrin extracellular domain was used for crystallization screens and experiments described below. Changes in the purification protocol for specific experiments are specified below.

4. Glycosylation minimization

Glycosylation has been one of the major concerns for the heterogeneity of the purified nicastrin for crystallization. One of the strategies was to use an antibiotic to suppress glycosylation in *vivo* such that proteins were not glycosylated during expression. The protocol used was based on methods previously described (LaPorte et al., 2008). As an initial test, two flasks 50 ml of Sf9 cell culture were prepared with one containing 2.5 mg/L tunicamycin (Sigma). After expression, samples of media and cells were collected from both flasks and the cells were lysed by sonication. Western blot was used to determine the presence of nicastrin in each sample.

Deglycosylation was another strategy tested to minimize the heterogeneity caused by glycosylation. A total of five deglycosylases were tested. They were PNGase F (New England Biolab), Endo H, Endo F1, Endo F2 and Endo F3 (Sigma). All reactions were performed according to the suggested protocols in the respective manuals.

PNGase F was ultimately chosen to be the deglycosylase for nicastrin purification. To determine whether PNGase F was able to remove all glycans from nicastrin, Pro-Q Emerald 300 Glycoprotein Gel and Blot Stain Kit (Molecular Probes) was used to stain one of the samples of nicastrin before and after PNGase F treatment.

The staining procedures used were from the manual of the staining kit. Briefly, samples of nicastrin were first separated in a SDS-PAGE gel. The gel was then fixed with 50 % methanol and 5 % acetic acid. After fixation, the gel was washed and then oxidized with oxidizing solution supplied by the staining kit. The oxidizing solution was then washed away and replaced with Pro-Q Emerald 300 staining solution. When the signals could be clearly observed after about 30 minutes, the gel was washed to remove the stain. The gel was then dried for permanent storage.

5. Limited proteolysis

Since neither the glycosylated nor deglycosylated full-length nicastrin crystallized, limited proteolysis was performed to seek a stable subdomain. Monomers nicastrin was prepared in 0.948 μg/μl. The purified nicastrin was mixed with trypsin in a protease to protein ratio of 1:300 (w/w). The digestion was performed either in 4 °C or room temperature as specified in the result section when the experiment was described. Samples were collected in 5, 15, 30 minutes, and 1, 2, 4, 7 and 17 hours after the reaction began, unless specified otherwise. To stop the digestion in a reaction, 1 μl of irreversible trypsin inhibitors was added to the sample, and the sample was heated at 95 °C for 5 minutes. SDS-PAGE was used to monitor the progress of the digestion. In the later half of the project, a TCEP-induced oligomer of nicastrin was observed. The stability of the oligomer was

analyzed by the same limited proteolysis protocol described above, with the exception that the purified protein sample was prepared in 1.12 μg/μl.

6. Crystallization screens

Purified nicastrin was concentrated to approximately 30 mg/ml using Amicon Ultra centrifugal filtration device (50 kD molecular mass cut-off). Crystal screens were set up with Phoenix robot (Art Robbins Instruments), mixing protein with solutions from commercial crystal screening blocks in 1:1 ratio. Each nicastrin construct or Fab-nicastrin complex is screened with 10-12 different commercial screening blocks.

7. Antibody

As a last resort to facilitate the crystallization of nicastrin, antibodies were developed for native nicastrin. This part of work was a collaboration with Oregon Health and Science University (OHSU) Monoclonal Antibody core. OHSU injected purified nicastrin into multiple mice, and two mice with the best response were sacrificed to derive hybridomas. The enzyme-linked immunosorbent assay (ELISA) was adopted to screen the efficacy of the antibodies, and the assays were done by the OHSU antibody core. To form hybridomas, the spleen cells from mice with the best immuno-responses were fused with P3X mouse myeloma cells. In the next 24-26 days, ELISA assays were repeatedly used to screen for cells that

produced antibodies that bound to native nicastrin. Candidate cell lines were expanded and supernates of these cells were tested by a pull down assays, high performance liquid chromatography (HPLC) and Western blots to confirm the binding of the antibody.

Antibodies with the best binding were cloned by limiting dilution at OHSU, and 400 ml of cells were cultured for each clone. Immunoglobulin G's (IgG) were purified from the supernatants at OHSU. IgG molecules are flexible in nature, so for the purpose of crystallization, it is necessary to use only the Fab region of the IgG to form complex with nicastrin. Therefore, purified to IgG's were subjected to papain (Worthington) cleavage to remove the F_c segment first in a small testing scale and then in a large preparative scale. The buffer condition for the digestion was adopted from the manual of the papain from Worthington, which contained phosphate buffered saline, 20 mM EDTA, 20 mM L-Cys-HCl and 20 mM β-mercaptomethanol (β-ME) and the reaction buffer was adjusted to pH 7.0 by 1 M NaOH. The enzymes to papain ratio and digestion time were optimized through small scale digestion. Digestion was stopped by addition of 17.5 mM of iodoacetamide. To isolate the Fab fragment, the digestion product was dialyzed in 20 mM Tris pH 8, 30-100 mM NaCl and then loaded onto a Fast Q ion exchange column. Fab does not bind to the Q column and thus stayed in the flow through. The F_c fragments that bound to the Q column were eluted upon the addition of

500 mM NaCl, 20 mM Tris pH 8 elution buffer. The concentration of NaCl in the dialysis buffer was first set to 100 mM and subsequently lowered if the F_c fragments were found in the flow through.

To generate a Fab and nicastrin complex, Fab and purified nicastrin were mixed in a 2:1 molar ratio. The mixture was incubated in room temperature for one hour and was then concentrated and injected in to a superdex 200 (10/30) size exclusion column (GE Life Sciences) equilibrated in 150 mM NaCl and 20 mM Tris pH 8. With the significant difference in the molecular weight between Fab-nicastrin complex and Fab alone, the mixture was well separated into two peaks on the size exclusion column. The complex peaks were collected for crystallization screen, and the Fab peak was collected to be recycled for future use.

D. Results

1. Expression and purification strategies

The aim of this project was to crystallize and determine a structure of human nicastrin. I have chosen to focus only on crystallizing the extracellular domain of nicastrin because the domain will most likely reveal most of the structural and information one can get from nicastrin. Hence, from here onward, all descriptions of nicastrin refer only to the extracellular domain of human nicastrin, which is residue 1 to 669 of the protein (Figure 7 A construct 1).

In the absence of the transmembrane span, the extracellular domain of nicastrin was secreted during expression. Multiple purification strategies were initially attempted to purify nicastrin from the media. Ultimately, ammonium sulfate precipitation followed by nickel affinity purification was chosen for its ease and relatively short purification time. The purification allowed nicastrin to be purified to virtually 100% pure based on assessment on SDS-PAGE (Figure 4 A).

At the initial phase of the project, the possibility of generating glycosylation-free nicastrin through the use of an antibiotic called tunicamycin was explored. Tunicamycin blocks the first step of N-linked glycosylation by inhibiting the formation of protein N-glycosidic linkages. This strategy turned out to be

infeasible. When tunicamycin was added to cell culture, nicastrin was no longer secreted to the media (Figure 4 B, lane 6 and 7). Western blot detected the presence of nicastrin inside the cells, but the protein was insoluble, which was evidenced by its failure to remain in the supernatant after the cells were lysed and centrifuged (Figure 4 B, lane 9).

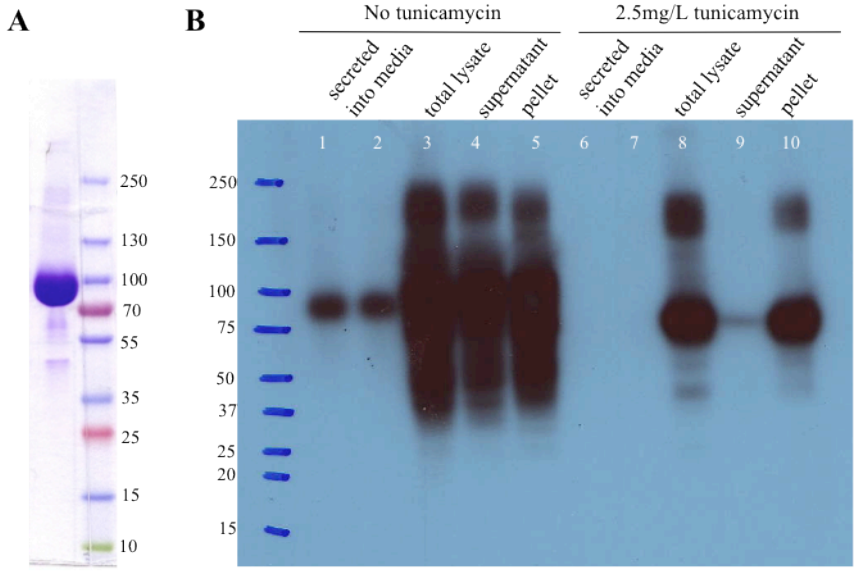

Figure 4. Purified nicastrin and the use of tunicamycin to suppress glycosylation. (A) Nicastrin is very pure after purification, as shown in this Coomassie blue-stained SDS-PAGE gel. (B) Comparison of nicastrin expression in the presence and absence of tunicamycin by Western blot using anti-nicastrin antibodies. Lane 1-5 are media and cells from no tunicamycin. Lane 6-10 are media and cells with

tunicamycin. In the presence of tunicamycin, nicastrin is not secreted to the media (lane 6-7) and the expressed nicastrin is not soluble (lane 9).

2. Deglycosylation of Nicastrin

Full-length nicastrin (i.e. the whole extracellular domain) was subjected to crystallization screening but no protein crystal was observed. The strategy was then changed to deglycosylate nicastrin in hopes of minimizing the heterogeneity possibly caused by glycosylation. Notably, the Sf9 cell line was selected to express nicastrin because it has no capability of complex glycosylation. This implies that the glycosylation will be much simpler to deal with than the complex glycosylations on nicastrin if it was expressed in mammalian cell line such as HEK cells or CHO cells.

Various deglycosylases were individually tested for their abilities to digest the glycans on the purified nicastrin. The digestion products were resolved using SDS-PAGE to compare the change in molecular weight of nicastrin after digestion (Figure 5 A). Among all the deglycosylases, PNGase F appeared to have removed the most glycosylations from nicastrin, so it became the enzyme of choice to deglycosylate nicastrin in all future protein purifications. After the digestion by PNGase F reached equilibrium and no further digestion of nicastrin could be observed, the molecular weight of nicastrin still appeared to be slightly

larger than its theoretical value on a SDS-PAGE. A highly sensitive fluorescent dye of glycans was used to determine if there was any sugar remaining on nicastrin after PNGase F digestion. Although PNGase F was able to remove most glycosylations from nicastrin, glycans were detected on the digested nicastrin (Figure 5 B, lane 4). Purified nicastrin treated with PNGase F was screened for crystallization, but no crystal was observed.

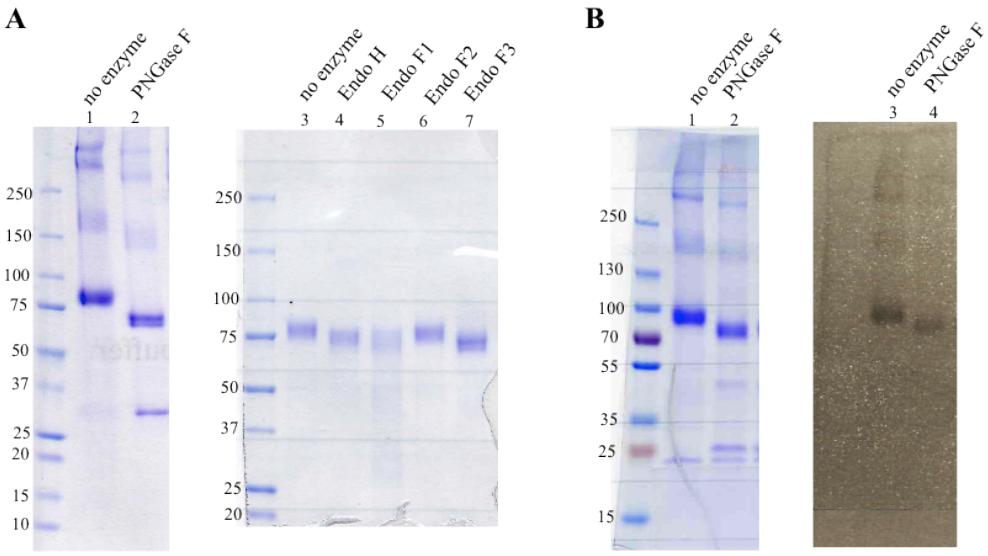

Figure 5. Deglycosylation assays of nicastrin. (A) Purified nicastrin was deglycosylated by various deglycosylases as indicated. The molecular weight of the digestion product of PNGase F, lane 2, is the smallest, suggesting that PNGase F removed the largest amount of glycans from nicastrin. (B) *Left* Purified nicastrin with or without PNGase F digestion were ran on a SDS-PAGE gel as a

control. *Right* The same samples were stained by Pro-Q Emerald 300 stain, revealing that some glycans remained on nicastrin even after it was digested by PNGase F.

3. Degradation and aggregation

The purified nicastrin was monitored by SDS-PAGE, and over time, the protein was found to degrade (Figure 6 A). The degradation was likely caused by metalloproteases, as EDTA effectively slowed down the degradation of the protein (Data not shown). Limited proteolysis by trypsin also showed that nicastrin was quickly digested to a subdomain of similar size as the degradation products (Figure 6 B, arrows). The degradation product was investigated to explore the possibility of finding a stable sub-domain of nicastrin that is suitable for crystallization. N-terminal sequencing, namely Edman degradation, was used to analyze the digestion product. The sequencing was performed by Protein Chemistry Technology Center at UT Southwestern. The sequencing results showed that the degraded nicastrin was cleaved at different sites. The top hit, however, matched all but one residue at residue 151-155, which is located in a long loop region according to the secondary structure prediction. The observed degradation highlighted the multi-domain nature of nicastrin, leading to a careful examination of the secondary structure prediction of nicastrin. An insertion construct was designed with a 3C protease cut site inserted between residue 150

and 151 (Figure 7 A, construct 2). When the construct was purified and treated with 3C protease, it behaved like wild-type nicastrin. It eluted in the same position as the wild-type protein on a size exclusion column (Figure 7 B). In a SDS-PAGE, it appeared to be the same size as the wild-type protein in the absence of β-ME (Figure 7 C, lane 2), but separated into two bands in the presence of β-ME (Figure 7 C, lane 4 black arrow). In addition, multiple truncations of the nicastrin constructs were generated with the intention to minimize the loop region to optimize crystal packing (Figure 7 A, constructs 3-8). All truncation constructs were purified, but their size exclusion profiles revealed that all but one truncation existed in multiple oligomeric states (Figure 7 D). Such solution behavior makes them undesirable for crystallization, as monodispersity is critical. The only truncation construct that appeared to be oligomerized as a single species spanned residues 249 to 669 (Figure 7 D, blue trace on left). This construct was purified in large quantity for crystallization screening, but no crystal has been observed.

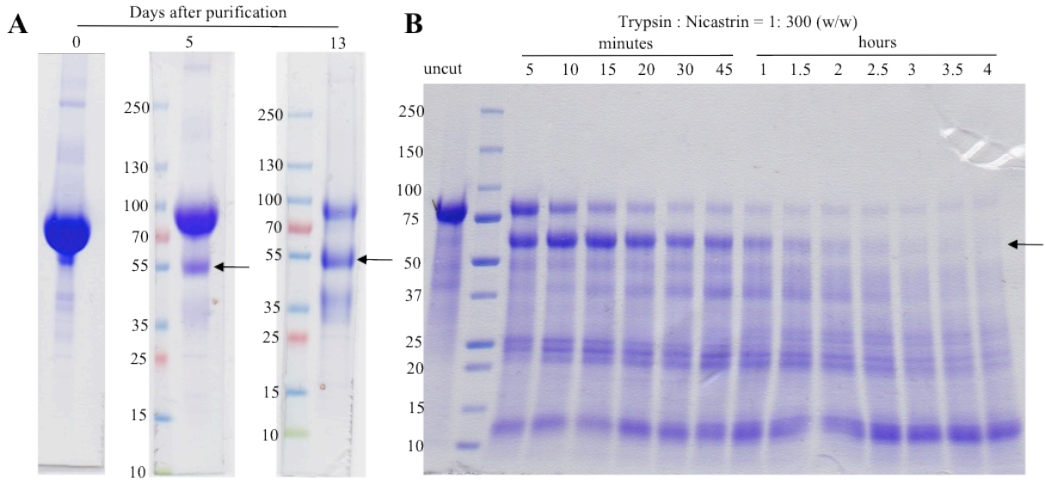

Figure 6. Degradation pattern and limited proteolysis of nicastrin. (A) Purified nicastrin was monitored by SDS-PAGE gel. A ~55 kD degradation product appeared within days after the purification (arrows). Approximately two weeks after the purification, more than half of the purified protein was degraded. (B) Limited proteolysis by trypsin revealed a band of about 60 kD (arrow) early on during the digestion, which is similar to the size of the degradation product in (A).

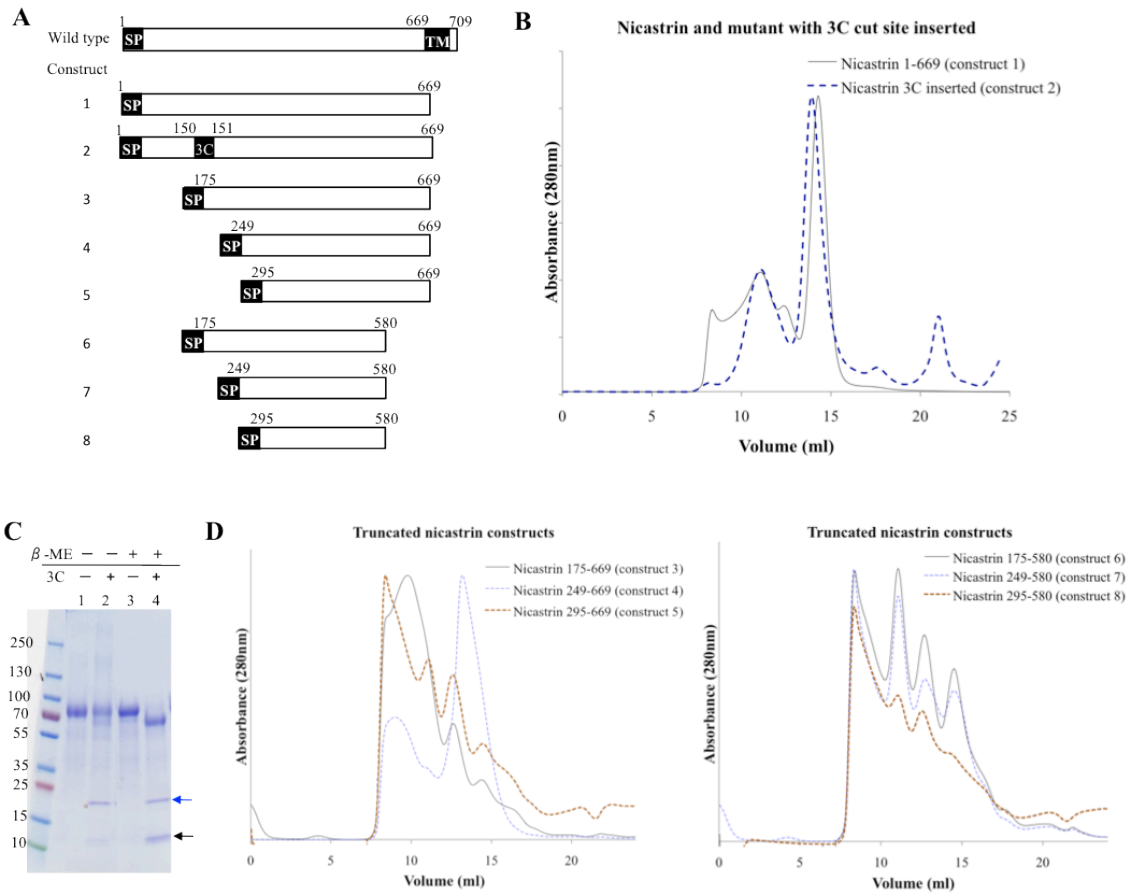

Figure 7. Construct design and behaviors of the mutated and/or truncated nicastrin. (A) The gene organizations of all the constructs described in this chapter are listed. (B) The size exclusion profiles of nicastrin full length (black line) and mutant with 3C cut site insertion at residue 150 (dashed blue line) are compared. The monomer of the two constructs both eluted at about 14 ml, suggesting that they are similar in size. (C) Nicastrin with 3C insertion was digested with 3C protease. In the absence of β-ME, the protein appeared to be the same in size (lane 1 and 2). 3C protease is marked with a blue arrow. In the presence of β-ME, the digestion

products were separated into two bands (lane 4). (D) Size exclusion profiles of all the nicastrin appeared to exist in multiple oligomeric states in solution except for construct 4, which was relatively homogenous (dashed blue line on left).

Another observation on the purified nicastrin was the emergence of some high molecular weight bands on SDS-PAGE over time (Figure 8 A, arrows). Heating or the use of β-ME could dissolve these high molecular weight species to the size of a monomer, so it is likely nicastrin formed non-specific intermolecular disulfide bonds (Figure 8 B). To prevent the formation of these disulfide bonds, purified nicastrin was treated with 2 mM iodoacetamide before the final step of purification. Iodoacetamide can covalently react with free sulfides on protein surface and thereby prevent intermolecular disulfide bonds. Unfortunately, purified nicastrin continued to form disulfide aggregate based on SDS-PAGE (Figure 8 C). As an alternative, TCEP was added to the final step of nicastrin purification, before setting up crystallization screens. Surprisingly, it turned out that nicastrin forms a different high molecular weight species in solution in the presence of reducing agent, both TCEP and dithiothreitol (DTT). When protein from monomer peak in figure 8 E (left arrow) was incubated with 2 mM TCEP for more than an hour, a new oligomer peak was observed in the size exclusion profile (Figure 8 E, right arrow). This high molecular weight species appeared as a monomer on SDS-PAGE (Figure 8 D “uncut” lane) and as a hexamer or

heptamer on size exclusion column (Figure 8 E, right arrow). This large oligomer of nicastrin was significantly more stable than the monomer based on limited proteolysis (Figure 6 B and 8 D). Crystallization screens were set up for this oligomer but no crystal has been observed.

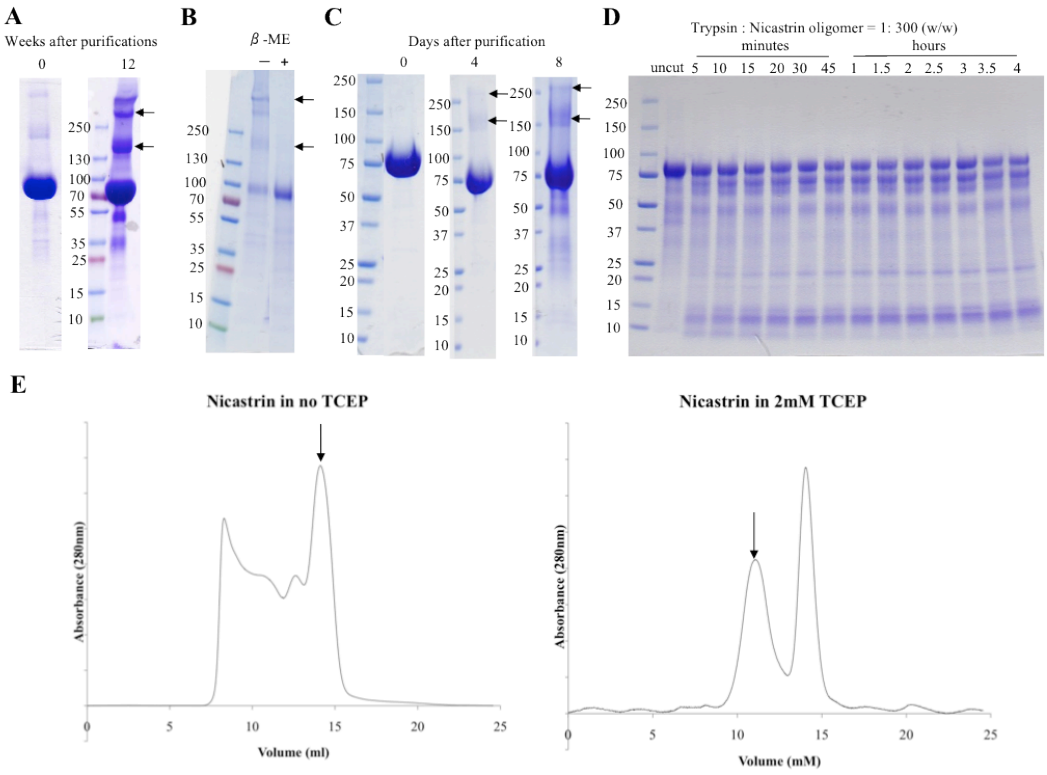

Figure 8. Aggregation of nicastrin and solution behavior of nicastrin in the presence of TCEP. (A) High molecular weight bands were observed weeks after purification (arrows). (B) The high molecular weight bands (arrows) collapsed into the monomer band when the nicastrin protein sample was exposed to 5% β-ME. This indicates that the high molecular weight aggregates were formed by

intermolecular disulfide bonds. (C) Nicastrin purified in the presence of 2 mM iodoacetamide formed high molecular weight aggregates similar to the one in (A) about 1 week after the protein purification, suggesting that iodoacetamide cannot prevent aggregation. (D) The oligomer of nicastrin, which formed in the presence of TCEP, was much more resistant to trypsin digestion as seen in the slow degradation of the protein compared to figure 6 B. (E) *Left* Nicastrin appeared predominantly as a monomer in size exclusion profile. The arrow on left indicates the position of the monomer peak. *Right* After incubating the monomer with 2 mM TCEP, an oligomer peak emerged in the size exclusion profile in addition to the monomer peak. The arrow on right indicates the position of the oligomer peak.

Nicastrin has a tendency to degrade and aggregate. Its flexibility and the lack of stability may have been the reason for its inability to crystallize. Therefore, the use of antibody to facilitate the crystallization of nicastrin was explored. Antibodies against nicastrin were generated at OHSU. Ten IgG's that bound strongly to the native nicastrin were selected and purified. The Fab fragments of all the selected IgG also bound to native nicastrin, and the Fab-nicastrin complex was used for crystallization screens. Although all ten purified Fab's formed stable complexes with nicastrin, none of the complexes were able to crystallize.

E. Discussions

Even though the goal of crystallizing nicastrin was not achieved, insights on the biochemical properties of nicastrin were attained. First, glycosylation is clearly important for the folding or trafficking of nicastrin, when the protein was heterologously expressed in Sf9 cells. When glycosylation was inhibited by tunicamycin, the expressed nicastrin was insoluble. On the other hand, glycosylation did not appear to be particularly important for the solubility or stability of the purified protein. Deglycosylated nicastrin was stable for days after purification and, in the presence of EDTA, for weeks after purification. A previous *in vivo* study have also found that glycosylation on nicastrin was important for trafficking but not for γ-secretase activity (Herreman et al., 2003). Second, nicastrin is highly soluble. Nicastrin has a relatively weak tendency to aggregate based on its size exclusion profile and almost never precipitated during protein purifications. It also tended to remain soluble in the crystallization drops even at very high concentration (>35 mg/ml). Third, the cysteine residues are important for the structure of nicastrin. This is inferred from three interesting observations. 1. Nicastrin forms intermolecular disulfide aggregates, but covalently protecting free cysteine on the surface by iodoacetamide was not sufficient to prevent the aggregation. 2. Treating nicastrin with reducing agent led to the formation of a nicastrin oligomer that is not linked by disulfide bonds. 3.

Disulfide bond(s) certainly play a role in maintaining the structure of nicastrin because when nicastrin was cleaved at around residue 150, the N-terminal domain and C-terminal domain did not dissociate from each other unless it was treated with reducing agent. Inferring from the three observations, some cysteine residues are likely located on the solvent accessible surface of nicastrin, but they are likely engaged in disulfide bonds. These disulfide bonds are probably the key to maintain nicastrin as a monomer, which is the physiologically relevant species.

The question remains as to what prevented the crystallization of nicastrin. The secondary structure prediction suggests that human nicastrin possesses many loops, which may make nicastrin flexible and dynamic in nature. The mobility of the loop regions may have prevented crystal packing. Another possibility is the heterogeneity in conformation due to different disulfide-bond combinations. In one of the deglycosylation experiments, the deglycosylated nicastrin appeared as two bands on SDS-PAGE. The two bands merged into the upper band in the presence of a reducing agent, suggesting that they have different combinations of disulfide bond(s). In light of these two possibilities, some of the unexplored experimental strategies such as deleting some of the long loops or co-crystallization with another γ-secretase component may prove to be a viable approach to the structure determination of nicastrin.

CHAPTER 2

BARIUM BLOCKAGE IN POTASSIUM CHANNELS

A. Summary

Barium is a heavy metal known to be a permeating blocker of potassium channels. Having a radius almost identical to K^+ but twice the charge, Ba^{2+} blocks by binding tightly to the K^+ binding site inside the pore of potassium channels, thus prevent the passage of K^+. The duration of the Ba^{2+} block can be modulated by the presence of a low concentration of K^+ at the external or internal side of the channel. This unique blocking property has been the key to determine the multi-ion nature of the potassium channel ion conduction pore before the first structure of a potassium channel was determined. In this study, the Ba^{2+} blocking properties of a potassium channel called NaK2K were studied using electrophysiology and X-ray crystallography. From a functional perspective, Ba^{2+} blocks NaK2K in the same manner as in other potassium channels. Blocking was short in the absence of low concentration of K^+ and the presence of low concentration K^+ significantly extended the internal Ba^{2+} blocking duration. From a structural perspective, Ba^{2+} binds to NaK2K in a pattern similar to potassium channels such as KcsA and MthK, but the binding varies in details. In the presence of K^+, Ba^{2+} blocks NaK2K at site 3 in conjunction with a K^+ at site 1. This binding configuration leads to a prolonged blocking effect on the channel, known as the external K^+-dependent

Ba^{2+} lock-in state. In the absence K^+, Ba^{2+} binds at sites 0 or 1 in addition to site 3. This pattern implies that the blocking duration is shorter because Ba^{2+} can enter the filter from intracellular side and exit from the extracellular side. The difference in binding pattern in the presence and absence of K^+ correlates well with the different blocking properties of Ba^{2+} and provides strong structural evidence of the mechanism of Ba^{2+} blocking in potassium channels.

B. Literature review

1. Ion channels

a. Discovery of ion channels

Ion channels are pore-forming proteins that allow diffusion of ions across cell membranes. Activities of ion channels have garnered scientific interest long before the molecule itself was first discovered. The road to understanding ion channel began with the discovery of excitability of nerve and muscle by ions. Back in the nineteenth century, scientists studied electrical signaling in nerve cells and tissues and speculated the existence of membrane with selective permeability (most notably the Bernstein's membrane hypothesis) (Behrends, 2012). Sidney Ringer found that a certain combination of potassium, sodium and calcium was sufficient to keep an isolated frog's heart beating. This solution, dubbed "Ringer's solution," was later used in numerous electrophysiological studies of ion channels (Hille, 2001; Miller, 2004).

In the twentieth century, our knowledge on ion channels was advanced through a series of findings on the electrical excitability of giant squid axons (Figure 9 A). The large axon from squid *Loligo* permitted the insertion of an electrode. As a result, a quantitative electrical recording of the action potential was, for the first time, available (Figure 9 B). Studies by Curtis and Cole on action potentials led to

the conclusion that the permeability of the membrane can change and propagate (Behrends, 2012). Hodgkin and Katz identified that inward sodium current and outward potassium current were components of action potential (Hille, 2001; Behrends, 2012). These findings confirmed the existence of a permeable cell membrane and build the foundations of the field of ion channels.

Later in the twentieth century, the development of the voltage clamp method marked the start of the rapid expansion on the understanding of ion channels. Modified from the voltage clamp, the gigaseal and whole-cell patch clamp techniques are probably the most common tools for functional studies of ion channels (Figure 9 C). All functional data of this project were also derived from these two techniques. Patch clamp experiments allow accurate measurements of single-channel current, with easy manipulation of experimental conditions. In conjunction with the modern cloning and sequencing techniques, numerous ion channels have been identified. The ion channel family is now among one of the biggest protein families.

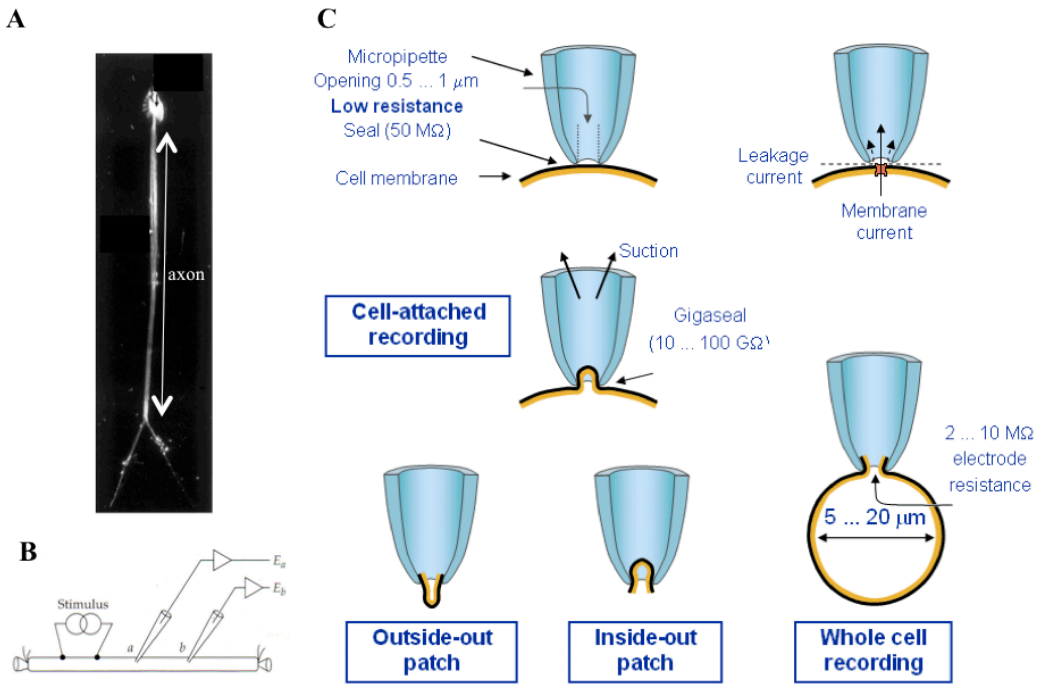

Figure 9. Classical techniques to study ion channels. (A) Neurons isolated from squid showing its long axon. Many of the early studies on ion channels took advantage the giant squid axon and developed the foundation of our current understanding on ion channels (Modified from Grant et al., 2006). (B) A sample set up for action potentials recording from the axon (Hille, 2001). (C) Developed in the late 1970s, patch clamp has been a key technique for functional study of ion channels. Depicted in the figure are the four major modes of patch clamp currently used (modified from Malmivuo and Plonsey, 1995).

b. Functions and taxonomy of ion channels

Ion channels can be found in all organisms and cells. Ions, which are not permeable to the hydrophobic lipid bilayers of membrane, traverse down the electro-chemical gradient through ion channels to enter or leave a cell or a cell compartment. Ion channels play essential role in maintaining the homeostasis of ions in a cell. The activity of an ion channels is therefore specific and regulated. Most ion channels are permeable to mainly one or a few ions under physiological conditions, and such selective permeation is termed selectivity. Most channels can also enter different functional states such as the opened, closed or inactivated state. The mechanism that switches a channel from one state to another is termed gating. Common gating mechanisms are membrane potential, mechanical distortion of membrane and chemical stimuli.

Ion channels are classified by their selectivity and gating mechanism. Among the gating mechanisms, channels can be classified into voltage-gated, intracellular ligand-gated and extracellular ligand-gated. More often, channels are named after and classified by the ions that they are selectively permeable to. Potassium channels, sodium channels, calcium channels, chloride channels and non-selective channels represent the major ion channels presently known in nature.

2. Potassium channels

a. Discovery and taxonomy of potassium channels

Potassium channels are ion channels that can selectively conduct K^+ and exclude the slightly smaller Na^+. K^+ current was first observed in studies of the action potential in giant squid axon, in which K^+ current was found to restore the membrane potential in the latter half of an action potential. Scientists speculated the K^+ and Na^+ currents were conducted by two separate molecular entities because they found that tetraethylammonium (TEA) can block K^+ current but not Na^+ current and vice versa for tetrodotoxin (TTX) (Hille, 2001). Interestingly, the first potassium channel gene ever identified was from a behavioral and genetic study of *Drosophila melanogaster*, completely independent of the functional study of K^+ channel. This *Drosophila* mutant, Shaker, has a phenotype of shaking appendages under ether anesthesia (Pongs, 1992). Molecular cloning of the Shaker locus revealed that the mutated gene was actually a potassium channel.

After the discovery of Shaker, many more potassium channels were subsequently cloned and sequenced. Potassium channel family was found to be highly diverse, much more so than its counterparts such as the sodium channels and calcium channels (Figure 10). The diversity has led to the hypothesis that potassium channels are ancient proteins that existed long before the emergence of other ion channels (Miller, 2000). Based on the evolutionary relationships between the

channels, potassium channels are divided into four classes, according to the number of transmembrane helices that they have - 2TM, 4TM or 6TM. The subfamilies are called inwardly rectifying potassium channels (K_{ir})(2TM), two-pore potassium channels (K_{2P})(4TM), voltage-gated potassium channels (K_v)(6TM) and calcium-activated potassium channels (K_{Ca})(6TM) (Alexander et al., 2013).

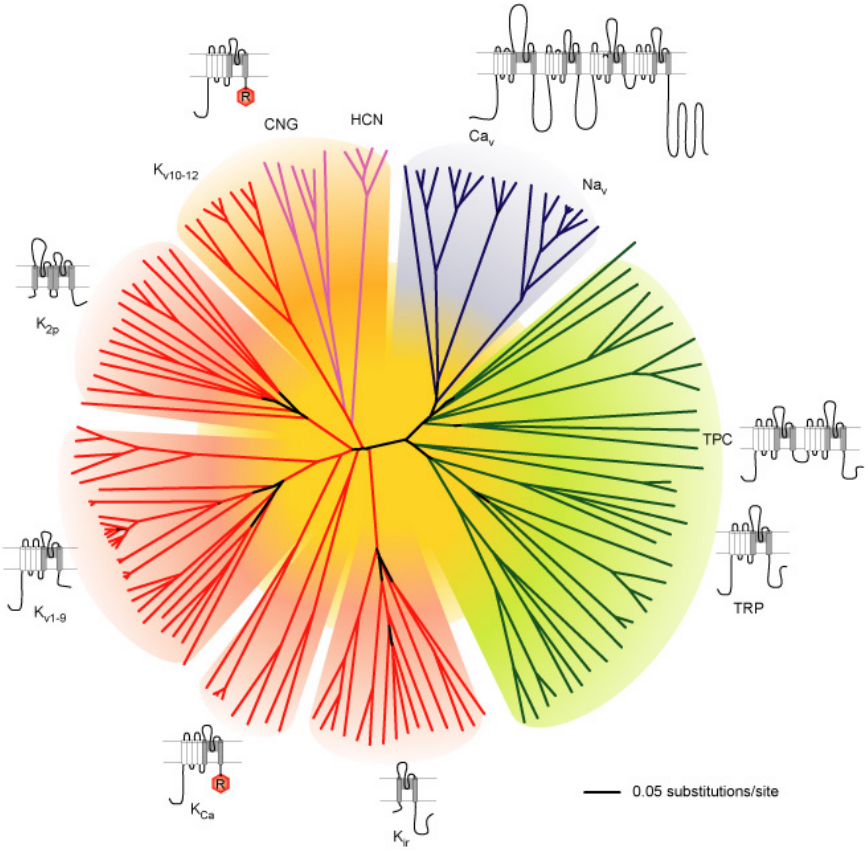

Figure 10. Evolutionary relationship and diversity of potassium channels relative to other cation channels (Yu and Catterall, 2004). Potassium channels are more diverse than other cation channel families.

b. Functions and common features of potassium channels

Virtually all organisms have potassium channels. Most higher organisms have all four classes of potassium channels. The functions of potassium channels span a broad spectrum of crucial physiological process. This includes nerve excitation, muscle cell contraction, signal transduction and hormone secretion. To serve the many different functions, potassium channels have evolved to have different conductance, gating mechanisms, and regulatory domains.

The major unifying features of all potassium channels are the topology of the pore domain and the signature sequence T(I/V)GYG in that region. The pore domain of a potassium channel consists of two transmembrane helices and, in between them, a short pore helix followed by a pore loop. The pore loop encompasses the signature sequence that is key to the selectivity of the channel. In addition, with the exception of K_{2P} being dimeric, all potassium channels are tetramers (Miller, 2000). While tetramers can be either homomeric or heteromeric (Sepulveda et al., 2015), they are often symmetrically arranged, with the four pore loops facing each other in the central axis forming an ion conduction pore (Figure 11 A). K_{2P}, which has two pore domains in tandem, also forms ion conduction pore similar to tetrameric potassium channels (Sepulveda et al., 2015); the two pore loops of each monomer constitute half of the pore. The ion conduction pore of a potassium

channel, also known as the selectivity filter, permits K^+ to exclusively pass through. The molecular details of our current understanding on the selectivity filter will be discussed below.

3. Ion conduction pore and selectivity

a. Understanding potassium channels through blockage studies

The mechanisms of selectivity and ion conduction have been a major subject of interests in potassium channel research. Early studies have shown that some potassium channels can conduct ions at a rate close to the diffusion limit while maintaining high selectivity for K^+ over Na^+. The coexistence of these two properties is not intuitive; high selectivity is supposedly achieved by high affinity ion binding, whereas the opposite is required for a high flux rate. To understand the molecular basis of such efficient selective permeation in potassium channels, the ion conduction of the channel was extensively characterized. In the mid- to late-twentieth century, channel blockers were intensively used in conjunction with the patch clamp to investigate selectivity.

A number of "classical principles" on potassium channels were established through the study of channel blockers and non-natural permeants. The basic, initial observations can be summarized as follow: 1. Quaternary ammonium salts such as tetrabutylammonium (TBA) and TEA block almost all potassium

channels, and in most cases, they block only either the internal or external side of the channel. 2. Ions that are smaller than K^+ such as Na^+ or Li^+ cannot pass through potassium channels. 3. Ions that are slightly larger than K^+ such as Rb^+, $NH4^+$ and Tl^+ can permeate the channels to some extent. 4. Cs^+, which is monovalent but larger than K^+ is a channel blocker. 5. Ba^{2+}, which has a ionic radius almost identical to K^+ (Shannon, 1976) but twice the charge, is also a blocker to potassium channels.

Based on the above observations, many follow up studies on the mechanism of blockage and permeation were reported, and here are some key findings: The rate of ion conduction and the shape of the ion conduction pore of potassium channels on giant squid axon were inferred from TEA blockage studies (Hille, 2001). The external side of pore was thought to be much narrower than the cytoplasmic side (Hille, 2001). A combination of tracer flux measurements and blockage studies provided the initial experimental evidence that multiple ions pass through the conduction pore in a single-filed manner (Hille and Schwarz, 1978). By comparing the permeability of 12 different ions or inorganic small molecules, Hille estimated the diameter of selectivity filter to be approximately 3 - 3.3 Å (Hille, 1973). By the 1970s, the snug-fit model for K^+ selectivity is proposed by thought leaders of the channel field. The model suggests that the ion conduction pore is rigid and has a diameter that perfectly fits K^+ (Andersen, 2011). It is also

proposed that the pore coordinates K^+ in a manner similar to how water coordinates the ion in aqueous solution, so that K^+ passes through with little energetic cost from dehydration (Dixit and Asthagiri, 2011b). A detailed Ba^{2+} blockage study by Neyton and Miller provided experimental evidence that the ion conduction pore has four contiguous ion-binding sites. Each site has a different affinity for K^+ and Ba^{2+} (Neyton and Miller, 1988b, a).

b. Understanding potassium channels through structural studies and molecular dynamics

The first structure of a potassium channel drastically advanced our understandings on the channel pore. In 1998, a crystal structure of a potassium channel, KcsA, from the gram-positive bacterium *Streptomyces lividans* was reported (Doyle et al., 1998) (Figure 11). The structure of the ion conduction pore confirmed many conclusions and models previously inferred from blocking and permeation studies. For examples, the ion conduction pore was indeed narrow and conducted ions in a single-file manner (Figure 11 A and B). Four ion-bindings sites were observed as Neyton and Miller had suggested, and they were formed by the residues of the signature sequence, TVGYG (Figure 11 C). What had not been predicted was the architecture of the ion-binding sites. Except for the site nearest to the internal side, each ion-binding site was formed by eight backbone carbonyl groups of the four TVGYG sequences from the tetrameric channel. The carbonyl groups were

in a cuboid (a rectangular cube) arrangement with an oxygen atom from each carbonyl group in each corner (Figure 11 C). A K^+ was caged in the center of the cuboid. However, with the proximity of the K^+ observed in the structure, the four K^+ ions were not expected to occupy the four binding sites at the same time. Rather, K^+ ions were speculated to simultaneously occupy either site 1 and 3 or site 2 and 4 (Figure 12). Previous blockage studies have also predicted the occupancy of 2-2.5 ions inside the channel at a given time (Hille and Schwarz, 1978; French and Shoukimas, 1985).

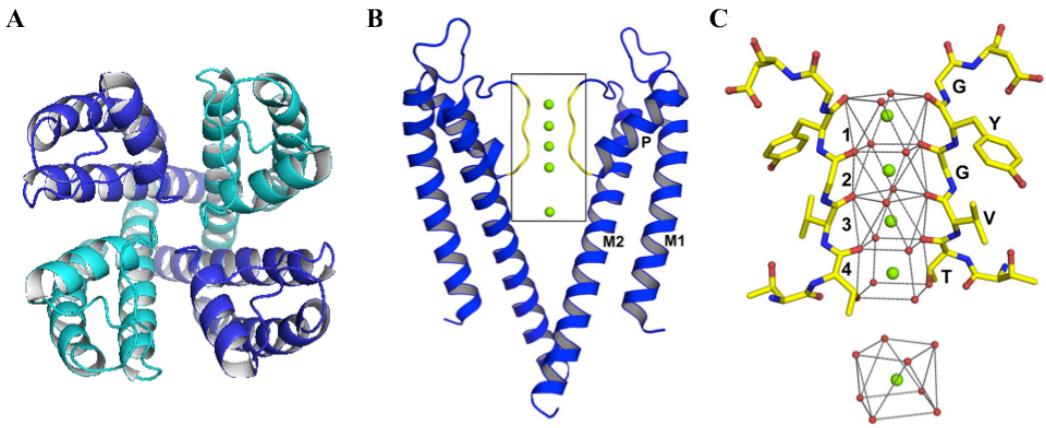

Figure 11. Structure of KcsA (1J95 and Alam and Jiang, 2011). (A) Overall structure of the tetrameric channel with each subunit colored in cyan or blue. The hole in the center of the four chains is the ion conduction pore. (B) Side view of KcsA channel with the front and back subunits removed. The boxed region is the selectivity filter with four ions inside the pore. (C) Zoomed-in view of the boxed

selectivity filter in (B). The oxygen atoms on the backbone carbonyl of the signature sequence "TVGYG" are arrayed in planes to coordinate the potassium ions.

To date, many the structures of many more potassium channels have been determined in high-resolution. Multiple structures have been obtained for each of the four classes of potassium channels, and all of them have ion conduction pores similar to that of KcsA. The availability of high-resolution structures has brought the field of potassium channel into a new era when studies are no longer dominated by patch clamp experiments and blockers. Molecular dynamics (MD) and structural studies are among some of the most popular new techniques to understand ion channels, especially for selectivity.

Studies on MD simulations were developed mainly based on the structures of potassium channels and thermodynamic theory. The methodology of MD varies and multiple models of selectivity have been generated. The main consensus from MD simulations is that the channel pore is more flexible than it appears in a crystal structure (Berneche and Roux, 2000; Shrivastava et al., 2002; Noskov et al., 2004; Noskov and Roux, 2007). The idea of a dynamic and flexible channel pore opposes the classic snug-fit model, in which the existence of rigid ion-binding sites is the major assumption. Many computational studies show that

selectivity arises from an energetically more favorable binding of K^+ than Na^+ in at least one of the ion-binding sites (Dixit and Asthagiri, 2011b). Some also reported that the number of coordination and the mode of coordination were likely the key factors for selectivity (Thomas et al., 2007; Dixit et al., 2009; Dixit and Asthagiri, 2011a). With multiple distinct models of selectivity presented, MD simulations have yet to generate a clear consensus on the origin of selectivity. Nonetheless, this is a powerful technique that can potentially provide unique perspectives to ion selectivity that is otherwise impossible from other methods.

X-ray crystallography is another popular alternative method to study ion channels. Mechanistic insights from structural studies on ion channels often come from structures with alternative conformations or ion-binding characteristics. For example, in the case of KcsA, the two structures obtained from high and low K^+ concentrations revealed the conductive and non-conductive conformations of the ion conduction pore (Zhou et al., 2001). However, similar structural changes were not observed in other potassium channels such as MthK (Jiang et al., 2002; Ye et al., 2010). A series of KcsA structures obtained from different concentrations of Rb^+ has provided experimental evidence for the hopping model of K^+ conduction proposed in the early days of ion channel research (Hille and Schwarz, 1978; Morais-Cabral et al., 2001). The hopping model was described as two K^+ ions moving in concert and hopping from site 1 and 3 configuration to site 2 and 4

configurations or the reverse (Figure 12). The change in configuration is promoted by the entrance of a third K^+ into site 1 (or 4), which repulses the K^+ in site 2 (3) (Morais-Cabral et al., 2001). This structural study with Rb^+ has confirmed the hopping model and permitted a more detailed description of K^+ conduction.

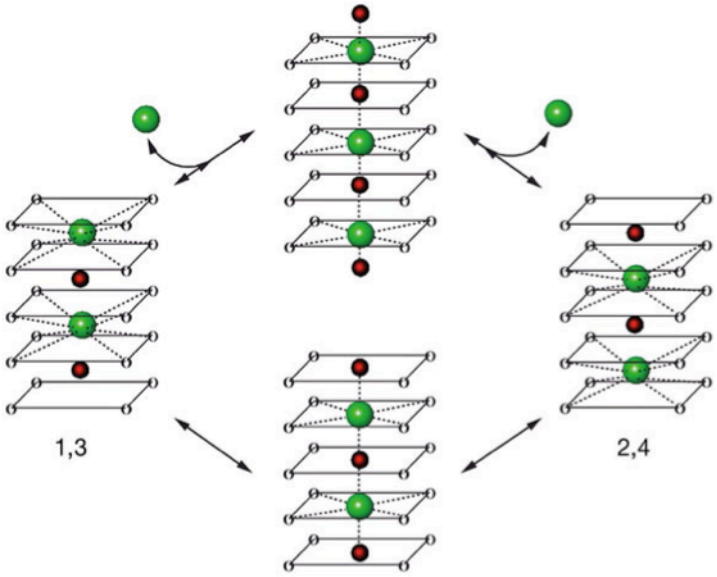

Figure 12. Model of K^+ conduction in potassium channels (Morais-Cabral et al., 2001). The selectivity filter is depicted as layers of oxygen atoms (white spheres) coordinating the K^+ (green spheres) inside with water molecules (red spheres) sandwiched in between. Entrance of a K^+ at one side drives the exit of a K^+ in the other side.

Another structural study on a non-selective channel, NaK, has also led to insights on K^+ selectivity. Two mutations on NaK were found to be sufficient to convert the non-selective cation channel into a potassium-selective channel (Derebe et al., 2011a). Structural studies on this mutant, NaK2K, showed that having four, but not one, two or three, binding sites is crucial for potassium channel to possess K^+ selectivity (Derebe et al., 2011a) (Figure 13). In a follow up study, structures of NaK2K from different concentrations of K^+ revealed that that the channel has two high-affinity binding sites for K^+, while a non-selective channel has only one (Sauer et al., 2013). This observations have led Sauer et al. to propose that the presence of two high-affinity sites create an energy barrier that allows the channel to be selectively permeable to K^+ even at a very low $[K^+]/[Na^+]$ ratio (Sauer et al., 2013). Together, these structural studies on NaK and NaK2K have justified the importance for potassium channel to have a multi-ion pore such that it is conserved in all potassium channels.

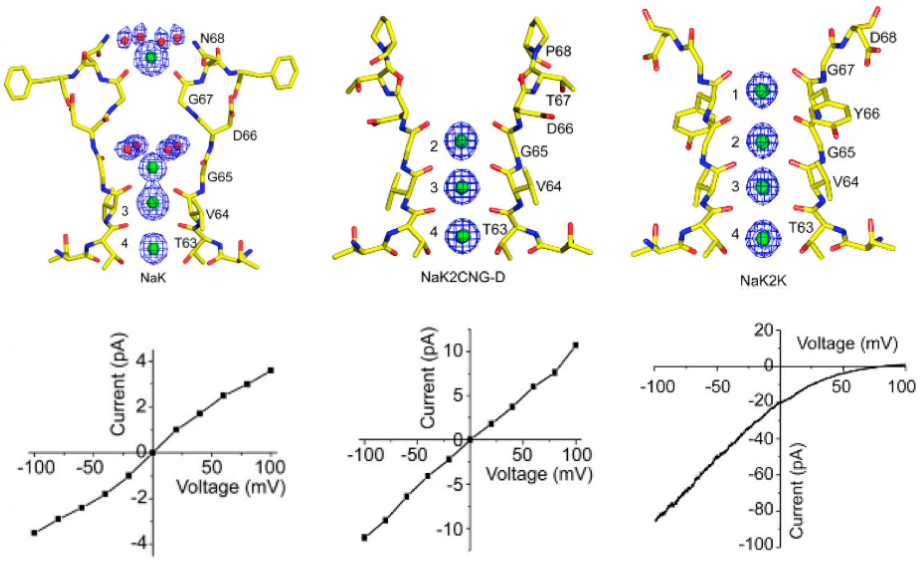

Number of binding site	Two	Three	Four
Selectivity	Non-selective	Non-selective	K^+ selective

Figure 13. Ion selectivity and the number of ion-binding sites. Studies on NaK and its mutants show that having four ion-binding sites gives rise to K^+ selectivity (Modified from Derebe et al., 2011a).

C. Methodology

1. Overall goal and strategy

This project aims to use a "modern" technique, X-ray crystallography, to study a "classic" problem – the molecular mechanism of Ba^{2+} blockage in potassium channel. Ba^{2+} has been reported to be a potassium channel blocker decades ago (Standen and Stanfield, 1978; Hermann and Gorman, 1979; Armstrong and Taylor, 1980; Armstrong et al., 1982; Vergara and Latorre, 1983). With an ionic radius similar to that of K^+ but twice the charge, Ba^{2+} blocks potassium channels by acting as a competitive inhibitor and binding at the ion-binding sites inside the ion conduction pore. A detailed characterization of Ba^{2+} blockage has shown that both the external and internal concentrations of K^+ affect the efficacy of Ba^{2+} block (Neyton and Miller, 1988a, b) (Figure 14). To further our understanding on Ba^{2+} blockage, we used the K^+-selective NaK mutant, NaK2K, to examine the ion binding as well as permeation properties of Ba^{2+}. NaK and its K^+-selective mutant NaK2K have been a very powerful tool for precise examination of ion binding and selectivity of both K^+-selective and non-selective channels. These proteins readily crystallize, and the crystals can be manipulated in various salt solutions without compromising their crystal diffraction qualities (Sauer et al., 2013). Besides, purified channel can be functionally characterized by single-channel recording using giant liposome patches (Derebe et al., 2011a; Derebe et al.,

2011b; Sauer et al., 2011; Sauer et al., 2013). Taking advantage of these properties, a combination of X-ray crystallography and giant liposome patch were used to characterize Ba^{2+} blockage in NaK2K.

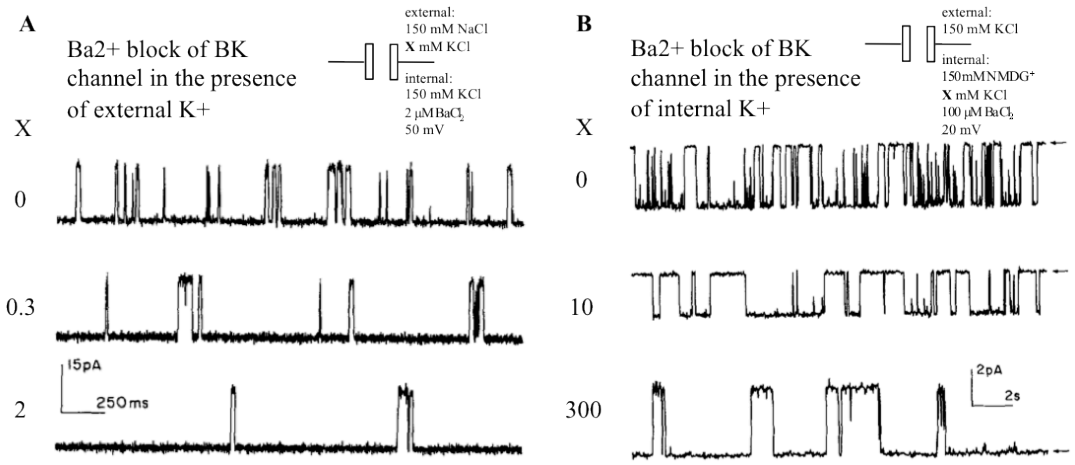

Figure 14. Ba^{2+} block in BK channels. (A) Single-channel recordings of BK channels with 2 μM Ba^{2+} at the internal side and various external K^+ concentrations (modified from Neyton and Miller, 1988b). As the concentration of K^+ increases from 0 to 2 mM, the blocking duration significantly increases. (B) Single-channel recordings of BK channel with 100 μM Ba^{2+} blocking at the internal side (modified from Neyton and Miller, 1988a). As the concentration of internal K^+ increases from 0 to 300 mM, the duration of block significantly increases.

2. Cloning, protein expression and purification

Wild-type NaK is a non-selective sodium-potassium channel from *Bacillus cereus*. The K^+-selective channel NaK2K is a double mutant of NaK, containing the mutations D66Y and N68D (Derebe et al., 2011a). For functional studies, the construct has an additional mutation, F92A, which increases flux through the channel but has no effect on selectivity (Alam and Jiang, 2009a, b).

To obtain protein for crystallization or liposome reconstitution, NaK2K (or NaK2K F92A for liposome reconstitution) was cloned into pQE-60 vector and transformed into *Escherichia coli* strain SG13009. The transformed cells were inoculated in Luria-Bertani (LB) broth at 37 °C until the OD reached 0.6-0.8 and were induced with 0.4 mM isopropyl β-D-1-thiogalactopyranoside (IPTG). Upon induction, 5 mM $BaCl_2$ was added to culture, which was previously found to enhance protein expression. After 18 hours of induction at 25 °C, cells were lysed in 100 mM KCl, 50 mM Tris-HCl pH 8.0 by sonication. The cell lysate was then solublized with 40 mM n-Decyl-β-D-maltoside (DM) (Anatrace) and gently agitated at room temperature for 3 hours. To remove the unsolublized fraction, the lysate was then centrifuged at 14000 rpm for 25 minutes. The supernatant was purified on Talon IMAC column (Clontech). NaK2K proteins were eluted with lysis buffer with 300 mM imidazole. To remove the 6x histidine tag, the eluted protein was digested with thrombin (Roche) overnight at 4 °C. The digested

protein was further purified on a Superdex-200 (10/30) size exclusion column (GE Life Sciences) that had been equilibrated in 100 mM KCl, 20 mM Tris-HCl pH 8.0, and 4 mM DM.

3. NaK2K crystallization and crystal soaking.

Purified NaK2K channels were concentrated to ~20 mg ml^{-1} with an Amicon Ultra centrifugal filtration device (50 kDa molecular mass cut-off). All crystals were initially grown by mixing equal volumes of protein solution (which contained the buffer used in the size exclusion column) with a well solution of 67.5-72.5 % (v/v) (±)-2-methyl-2, 4-pentanediol (MPD), and 100 mM MES for pH 6.0-6.5, 100 mM KCl, and 100 – 300 mM potassium citrate pH 6.5. The crystallization drops were set up in sitting drop fashion and stored at 20 °C. When the crystals grew to their maximum sizes after about two weeks, they were used for soaking experiments. In all soaking experiments, crystals were soaked overnight in stabilization solution containing 70% MPD, 10 mM DM, 100 mM MES-NaOH, pH 6.0, 100 mM NaCl or KCl, and 20 mM $BaCl_2$. All crystals were flash-cooled in liquid nitrogen with the stabilization solution serving as cryoprotectant.

4. Data collection and structure determination

X-ray diffraction data were collected at the Advanced Light Source (ALS) beamlines 8.2.1 and 8.2.2 and the Advanced Photon Source (APS) beamlines 19-ID and 23-ID. All crystals had the symmetry of space group I4 with unit cell dimensions of a = b = 68 Å, c = 89 Å. Data were processed and scaled in HKL2000 (Otwinowski and Minor, 1997). Since all crystals for the soaking experiment were obtained from the same crystallization conditions as the previously determined NaK2K structure, the NaK2K-K^+ complex structure (PDB code 3OUF) was directly used in the refinement against the diffraction data of each soaked crystal in Phenix (Adams et al., 2010) with solvent molecules omitted. Before the final round of refinement, the filter ions from soaking conditions and the solvent molecules were added in COOT (Emsley and Cowtan, 2004) using F_o-F_c ion omit maps. Data from all soaked crystals were scaled against the original NaK2K-K^+ complex crystal before refinement and map calculation. Each asymmetric unit contained two molecules (subunits A and B). The four-fold axis of channel tetramer coincided with the crystallographic tetrad. Since subunit A has lower and much more stable B factors than subunit B, only the tetramer generated from subunit A was used for structural analysis in this study.

5. Data Analysis

One dimensional (1-D) electron density profiles through the filter were calculated as previously described (Morais-Cabral et al., 2001) by sampling the F_o-F_c ion omit maps (all calculated at 1.85 Å) along the C axis (which coincides with the molecular four-fold axis of channel tetramer) using MAPMAN (Kleywegt and Jones, 1996). For occupancy estimation, the total area of the four peaks above the baseline in 1-D electron density profile were set to represent electrons from two K^+ ions and two water molecules in NaK2K-K^+ complex (total of 56 electrons). The area of individual peak in the 1-D profile was then normalized against the peaks of the NaK2K-K^+ complex to calculate the number of electrons each peak represents. Ion occupancy at each site was then calculated using the following equation assuming a total occupancy of 1 for water (10 e^-) and ion (number of electron of Na^+, K^+ or Ba^{2+}) at each site.

number of electrons calculated from the peak area = $N \times Y + 10 \times (1\text{-}Y)$ (1)

where N is the number of electrons for each filter ion (18 for K^+, 36 for Rb^+, 54 for Cs^+ and Ba^{2+}), and Y is the occupancy for the respective ion.

6. Proteoliposomes reconstitution and electrophysiology

All single-channel recordings were performed using giant liposome patches as previously described (Derebe et al., 2011a; Derebe et al., 2011b). Lipid vesicles were prepared for reconstitution. For each experiment, 10 mg total of 3:1 (w/w)

ratio of 1-palmitoyl-2-oleoyl-phosphatidylethanolamine (POPE) and 1-palmitoyl-2-oleoyl-phosphatidylglycerol (POPG) (Avanti Polar Lipids) was first air dried in argon gas and further dried with SpeedVac for 1.5 – 2 hours. Dried lipid was resuspended in 100 mM KCl and 20 mM Tris pH 8.0 and sonicated in water bath until the lipid vesicles were homogenized and became transparent. 10 mM DM was then added to the lipid solution and mixed. Purified proteins were then added into the lipid mixture in a protein/lipid ratio of 0.05-0.1 μg/mg and mixed for another hour. Reconstituted liposomes were dialyzed in 100 mM KCl, 20 mM Tris pH 8.0 for 72 hours, with buffer change every 24 hours.

Giant liposomes were obtained by air drying 2-3 μl of liposome sample on a clean cover slip overnight at 4^{o}C. Next day, the liposomes were rehydrated at room temperature in bath solution containing 150 mM KCl, 10 mM HEPES and 1 mM EGTA, pH 7.4 buffered with Tris. Patch pipettes were pulled from Borosilicate glass (Harvard Apparatus) to a resistance of 8-12 MΩ filled with pipette solution containing 150 mM NaCl and/or KCl (as indicated in result section), 1 mM EGTA and 10 mM HEPES pH 7.4 buffered with NaOH. A gigaseal (> 10 GΩ) was obtained by gentle suction when the patch pipette attached to the giant liposome. To get a single layer of membrane in the patch, the pipette was pulled away from the giant liposome and the tip was exposed to air for 1-2 seconds. Membrane voltage was controlled, and currents were recorded using an

Axopatch 200B amplifier with a Digidata 1322A digitizer (Axon Instruments). Currents were low-pass filtered at 1 kHz and sampled at 20 kHz. Upon the observation of single-channel activity, the bath solution with 150 mM KCl was replaced by another salt as indicated in each experiment. All chemicals used for solution preparation were purchased from Sigma.

In the study of intracellular Ba^{2+} blocking, the free Ba^{2+} concentration was controlled by mixing 5 mM EGTA with an appropriate amount of $BaCl_2$ calculated using the software MAXCHELATOR (Patton et al., 2004; Bers et al., 2010). Owing to the two possible orientations of reconstituted NaK2K in the liposomes, 30 mM tetrapentyl ammonium (TPeA), an intracellular pore blocker, was added to the bath solution to ensure that the channel in the recording had its intracellular side facing the bath solution. TPeA was later removed through bath solution exchange before Ba^{2+} block measurements.

D. Results

1. External K^+-dependent barium block of the NaK2K channel

Ba^{2+}, which has an identical ionic radius as K^+, is known to bind K^+ channel filters and block the K^+ current. It has been shown that the kinetics of internal Ba^{2+} blocking (mean blocking dwell time) depends on the presence of external K^+ (Neyton and Miller, 1988a, b; Piasta et al., 2011). To test if this also occurs in NaK2K, a similar blocking assay was performed on NaK2K using giant liposome patch clamps. In this assay, the extracellular solution (in the pipette) contained 150 mM NaCl with or without K^+, and the intracellular solution (bath) contained 150 mM KCl with and without $BaCl_2$. Shown in Figure 15 A are sample single-channel recording traces of outward NaK2K currents without Ba^{2+} (control in bi-ionic condition), with 10 μM internal Ba^{2+} but no external K^+, and with 10 μM internal Ba^{2+} and 5 mM external K^+. In the absence of Ba^{2+} (Figure 15 A, top trace), NaK2K exhibits two closing states, as demonstrated by the nonconducting dwell time histogram: brief closings with a time constant of ~0.7 ms (τ1) and longer closings with a time constant of ~5 ms (τ2). The rapid closings are an intrinsic property of the pore and were also observed in other K^+ channels with a submillisecond time constant (Li et al., 2007; Piasta et al., 2011). These spontaneous closings are likely a result of the fast gating at the filter region. The longer closings can be attributed to gating at the intracellular bundle crossing. The

addition of 10 μM Ba^{2+} at the intracellular side (Figure 15 A, middle trace) does not change the kinetics of brief closings. However, it increases the time constant for the longer closings (τ2) to ~18 ms. This increase of closing time can be attributed to Ba^{2+} block, which lasts longer than the kinetics of the intracellular gating. When 5 mM K^+ is included in the extracellular solution (5 mM KCl/145 mM NaCl), a third extremely long closing state with a time constant in the order of seconds (τ3, ~3,200 ms in this measurement) is observed. The two Ba^{2+}-induced closing states (τ2 and τ3; Figure 15 A, bottom trace) in the presence of external K^+ are reminiscent of the two Ba^{2+} block states with fast and slow time constants (termed τf and τs) observed in KcsA (Piasta et al., 2011). Similar to KcsA, the time constant of fast Ba^{2+} block (τ2) in NaK2K appears to be independent of external K^+, as it remains almost unchanged in the presence or absence of external K^+. The slow Ba^{2+} block (τ3), however, depends on external [K^+]. It represents an external K^+-induced Ba^{2+} lock-in state in which external K^+ binding prevents the Ba^{2+} ion in the filter from escaping to the extracellular side and prolongs Ba^{2+} block to a timescale of seconds.

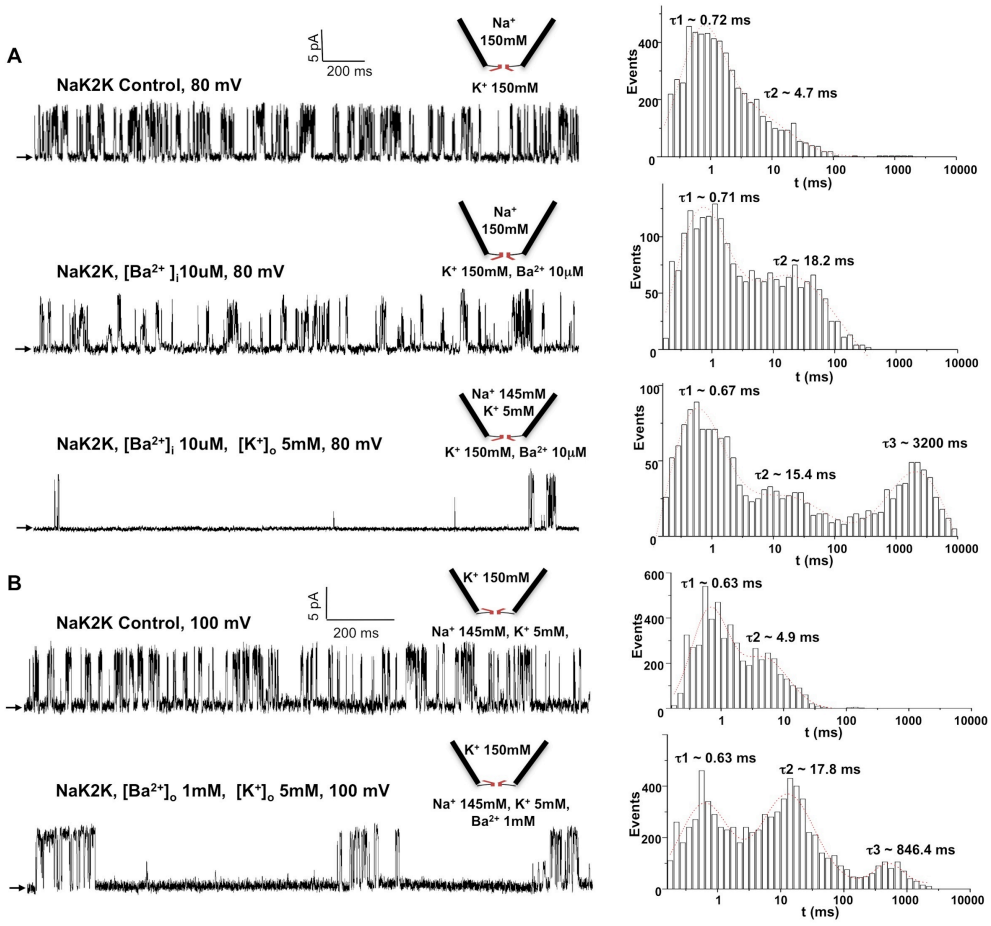

Figure 15. Ba^{2+} block in NaK2K. (A) Internal Ba^{2+} block in the presence and absence of external K^+. The nonconducting dwell time histograms with exponential fits for each recording are shown beside each trace. Only the patch that contains a channel with its intracellular side facing the bath solution was used in the recording. (B) External Ba^{2+} block in the presence of 5 mM external K^+. Only the patch that contains a channel with its extracellular side facing the bath solution was used in the recording.

The effect of external Ba^{2+} block in NaK2K (Figure 15 B) was also measured. In this assay, the channel in the patch has its extracellular side facing the bath solution containing 145 mM NaCl and 5 mM KCl, with or without Ba^{2+}, and the intracellular solution (in pipette) contained 150 mM KCl. Similar to other K^+ channels, the Ba^{2+} block in NaK2K is also much weaker from the external side, as shown in the sample trace of outward currents with 1 mM Ba^{2+} (Figure 15 B). However, the external Ba^{2+} still induces two block states with fast and slow time constants in the presence of external K^+, as seen in KcsA.

2. Barium binding in the NaK2K filter in the presence of potassium

To examine the structural basis of the K^+-dependent Ba^{2+} block in the NaK2K channel, we soaked NaK2K crystals in a stabilization solution containing 20 mM Ba^{2+} in addition to 100 mM K^+ and determined the structure to 1.82 Å resolution (Protein Data Bank accession no. 4PDV). Although the filter structure is virtually the same as that of the NaK2K–K^+ complex, the electron density of bound ions within the filter is unevenly distributed, with the strongest density at site 3 and much weaker density at sites 2 and 4 (Figure 16 A). As confirmed by the anomalous difference map (Figure 16 B), Ba^{2+} binds almost exclusively at site 3, a finding that is very different from Ba^{2+} binding in KcsA, which occurs mainly at site 4 with weaker binding at site 2 when K^+ is absent (Jiang and MacKinnon, 2000; Lockless et al., 2007). Analysis of site 3 intensity in the one-dimensional

electron-density profile yielded a Ba^{2+} occupancy of 0.74 (Figure 16 A). The presence of site 3 Ba^{2+} excludes the K^+ binding at neighboring sites, resulting in weak density at sites 2 and 4. Interestingly, even with Ba^{2+} occupying site 3, K^+ remains bound at site 1, as indicated by the strong electron density without obvious anomalous signal, eliminating the possibility of this density coming from Ba^{2+}. The exclusion of K^+ at sites 2 and 4 upon Ba^{2+} binding actually enhances the occupancy of site 1 K^+ to ~0.95 as estimated based on the peak height in the one-dimensional electron density profile. The high occupancy of site 1 K^+ (close to unity) and site 3 Ba^{2+} indicates that their binding at these two sites can take place simultaneously. This co-residence of Ba^{2+} at site 3 and K^+ at site 1 is a snapshot of the lock-in state, which explains how K^+ prevents Ba^{2+} from exiting to the extracellular side and prolongs the Ba^{2+} blockage observed in our electrophysiology data. Two observations indicate that Ba^{2+} and Na^+ are also partially occupying site 4 in the crystal in addition to K^+, resulting in a stronger site 4 density than that of site 2. One observation is that the site 4 ion has some weak anomalous signals, indicating the presence of Ba^{2+} at low occupancy. The other observation is that the site 4 density is diffuse and extended toward the bottom of site 4 where Na^+ typically binds (Alam and Jiang, 2009b), and the soaking solution did contain Na^+ from NaOH used to adjust the pH of the MES buffer. In the structure of the NaK2K–Ba^{2+} complex in NaCl (discussed in the next section D.3.), we did demonstrate that Na^+ can co-reside at the bottom of site

4 with Ba^{2+} occupying site 3. An additional anomalous difference-density peak, although weak, was observed on the extracellular face of the channel just above site 0, indicating a second weak Ba^{2+} site. The presence of external Ba^{2+} can also be confirmed by the strong electron density that was not observed in the NaK2K–K^+ complex. Unlike the site 0 Ba^{2+} seen in the NaK2K–Ba^{2+} complex in NaCl (discussed in the next section), this bound Ba^{2+} is further outside on the central axis and fully hydrated (Figure 16 A, inset). Similar weak binding of a fully hydrated divalent cation at the external entrance has also been observed in other NaK mutants, such as a hydrated Ca^{2+} in the cyclic nucleotide gated channel mimic mutant of NaK (Derebe et al., 2011b).

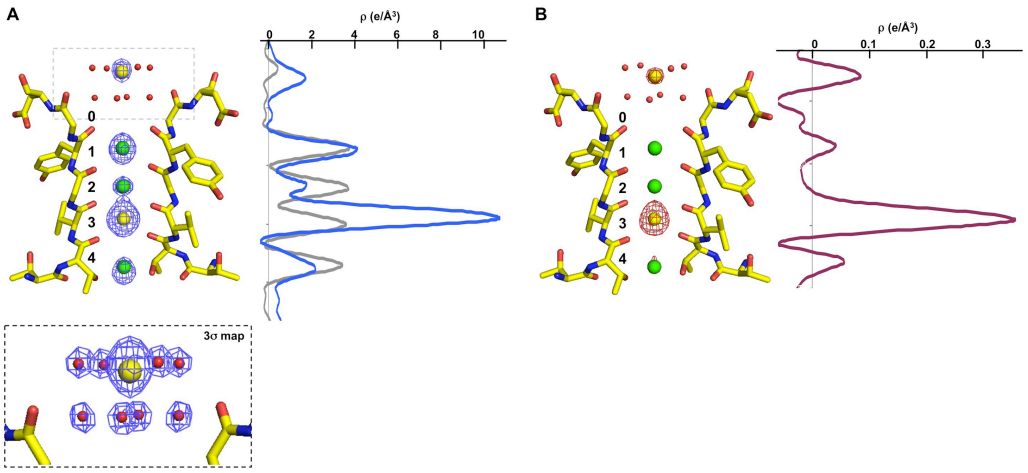

Figure 16. Ba^{2+} binding in the NaK2K filter in the presence of K^+. (A) F_o–F_c ion omit map (6σ) of the NaK2K–Ba^{2+} complex and the one-dimensional electron-density profile along the filter. The Ba^{2+} ions are modeled as yellow spheres. The

density at sites 1, 2, and 4 is modeled as K^+ ions (green spheres) for simplicity. The inset (boxed) is a magnified view of the external Ba^{2+} with the F_o–F_c ion omit map contoured at 3σ to show the density of water molecules. (B) Anomalous difference Fourier map (7σ) of the NaK2K–Ba^{2+} complex and the one-dimensional anomalous difference density profile at the selectivity filter region.

3. Barium binding in the NaK2K filter in the absence of potassium

To reveal the structural basis of fast Ba^{2+} blockage in the absence of external K^+, we performed a Ba^{2+} soaking experiment in the presence of 100 mM NaCl in stabilization solution instead of KCl and determined the structure of the Ba^{2+}/Na^+-soaked NaK2K crystal to 1.85 Å (Protein Data Bank accession no. 4PDR). In the absence of K^+, Ba^{2+} binds at three positions, as demonstrated in the anomalous difference map (Figure 17 B). Even though site 3 is still the major Ba^{2+} site with full occupancy (~1.0), Ba^{2+} also binds at site 1 and site 0. Because of the close proximity of these two sites (approximately 2.8 Å apart), Ba^{2+} is unlikely to simultaneously occupy both of them. As indicated by the stronger anomalous signal, site 0 Ba^{2+} has a higher occupancy (~0.44) than that of site 1 (~0.24). Despite multiple binding sites, the likelihood of having two divalent Ba^{2+} ions within the NaK2K filter is low because of the strong electrostatic repulsion. Thus, the low probability of Ba^{2+} binding at site 1 could be the result of high Ba^{2+}

occupancy at site 3. Nevertheless, without K^+ competition, Ba^{2+} binding at site 3 as well as site 1 or 0 reveals the steps along the path of Ba^{2+} release to the extracellular side. Although fully occupied site 3 Ba^{2+} almost completely excludes the binding of any other ion at site 2, Na^+ can still reside at the bottom edge of site 4 with the coordination of Thr63 hydroxyl groups and a water molecule in the cavity as commonly seen in multiple NaK mutant structures (Figure 17 A, inset). As sites 0 and 1 become the main secondary sites for Ba^{2+} in the absence of K^+ competition, Ba^{2+} binding is no longer observed at the external entrance above site 0.

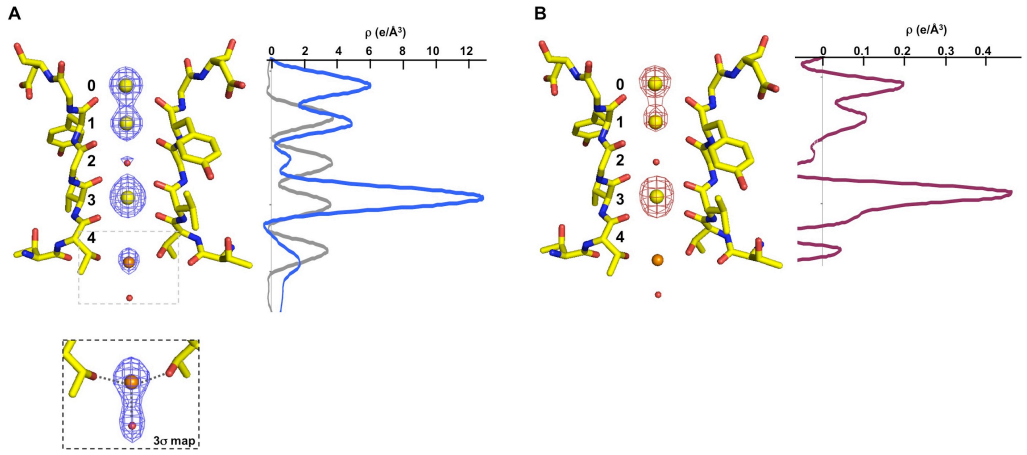

Figure 17. Ba^{2+} binding in the NaK2K filter in the absence of K^+. (A) F_o–F_c ion omit map (6σ) of the NaK2K–Ba^{2+} complex in NaCl and the one-dimensional electron-density profile along the filter. The Ba^{2+} ions are modeled as yellow spheres. Site 2 density is modeled as water (red spheres), and site 4 density is

modeled as a Na^+ ion (orange spheres). The inset (boxed) is a magnified view of site 4 Na^+ with the F_o–F_c ion omit map contoured at 3σ to show the density of the cavity water molecule. (B) Anomalous difference Fourier map (7σ) of the NaK2K–Ba^{2+} complex in NaCl and the one-dimensional anomalous difference density profile at the selectivity filter region.

Table 1. Data collection and refinement statistics for NaK2K in complex with Ba^{2+}

Statistic	NaK2K-Ba^{2+} (in KCl)	NaK2K-Ba^{2+} (in NaCl)
Data Collection		
Space group	I_4	I_4
Cell Dimensions a=b, c (Å)	68.065, 89.614	68.042, 89.627
Wavelength (Å)	0.9999	0.9793
Resolution (Å)	50 - 1.821	50 - 1.85
R_{sym} (%)	5.4 (99.8)	6.3 (93.1)
$I/\sigma I$	37.0 (1.8)	39.2 (2.3)
No. reflections- total (unique)	128478 (18212)	130140 (17542)
Completeness (%)	99.53 (100.00)	99.24 (99.9)
Redundancy	7.1 (7.2)	7.4 (7.0)
Refinement		
Resolution (Å)	1.82	1.85
R_{work}/R_{free}	0.2053/0.2371	0.1998/0.2266
No. of atoms		
Protein	1589	1588
MPD/ion	4/9	4/8
Water	63	63
R.m.s.d.		
Bond angles (°)	1.20	1.09
Bond lengths (Å)	0.008	0.008

E. Discussions

From a functional perspective, the Ba^{2+} blockage response in NaK2K is qualitatively identical to other potassium channels reported previously (Neyton and Miller, 1988a, b; Harris et al., 1998; Piasta et al., 2011). Similar to BK, MthK and KcsA, Ba^{2+} blocks NaK2K, and the mean blocking time is significantly lengthened in the presence of low concentrations of external or internal K^+. While wild-type NaK is not a potassium-selective channel, the potassium-selective mutant NaK2K very likely uses a molecular mechanism identical to prototypical potassium channels to selectively conduct K^+ such that they exhibit similar Ba^{2+} blocking behaviors.

Interestingly, NaK2K has a binding profile of Ba^{2+} different from KcsA and MthK, which are the only two potassium channels with their Ba^{2+} binding sites structurally determined (Jiang and MacKinnon, 2000; Guo et al., 2014). In NaK2K, site 3 is the primary site for Ba^{2+} in the presence of potassium, but in the case of KcsA and MthK, site 4 is the primary site. In the absence of K^+, Ba^{2+} can access site 0 and 1 in NaK2K but site 2 and 3 in MthK and site 2 in KcsA. Despite the differences in binding-site preferences, the binding patterns of NaK2K, KcsA and MthK do share some key similarities. One of them is the fact that Ba^{2+} can bind to multiple sites in the presence of Na^+. This implies that most sites have a

higher affinity for Ba^{2+} than Na^{+}. Na^{+} is almost completely absent and was out-competed by Ba^{2+} in a potassium channel filter. Another common feature is that there is always a high-affinity binding site for K^{+}. In NaK2K, K^{+} can bind to site 1 and completely exclude the binding of Ba^{2+}. Similarly, site 1 in MthK was shown to have higher affinity for K^{+} and Ba^{2+} (Guo et al., 2014). Other studies have also inferred that a ion-binding site external to the Ba^{2+} binding site has high selectivity for K^{+} in various potassium channels (Neyton and Miller, 1988a, b; Harris et al., 1998; Spassova and Lu, 1999). These two observations imply that the Ba^{2+} blocks NaK2K and other potassium channels with the same mechanism even though they display different ion-binding profiles.

Neyton and Miller previously proposed a general model for Ba^{2+} blockage, and their model is verified by the Ba^{2+} binding profile we observed here in NaK2K (Neyton and Miller, 1988a, b). In the absence of external K^{+}, frequent but short blocking events were observed. Ba^{2+} blocks outward current by binding at site 3. Under strong electrochemical outward driving force, Ba^{2+} can be dislocated from site 3 and depart the channel via the secondary site (site 1). The structure of NaK2K in Ba^{2+}/Na^{+} illustrates this scenario (Figure 17 A). In the presence of a low concentration of external K^{+}, the blocking duration was significantly lengthened. This is because site 1 has high selectivity for K^{+}, and external K^{+} will bind to site 1 tightly. The strong binding of K^{+} at site 1 prevents Ba^{2+} from

leaving site 3 by passing site 1. Ba^{2+} could depart the channel only when K^+ at site 1 transiently leaves site 1 or if Ba^{2+} moves inward against the electrochemical gradient. The binding configuration of K^+ at site 1 and Ba^{2+} at site 3 is very stable and locks the channel in closed state for lengthy durations. Neyton and Miller termed this configuration the "locked-in state," and this is the dominant binding configuration observed in our NaK2K structure in Ba^{2+}/K^+. For other K^+ channels, the K^+-selective site may not necessarily be site 1. They can achieve the locked-in state by having the K^+-selective site external to the primary Ba^{2+} binding site. For example, given the primary Ba^{2+} site to be site 4, the locked-in site in KcsA can be site 2. The channel will be in a locked-in state in a binding configuration of K^+ at site 2 and Ba^{2+} at site 4. Different potassium channels can have different Ba^{2+} binding profiles yet the same mechanism of Ba^{2+} blockade.

The question that is yet to solve is the origin of the difference in Ba^{2+} binding profiles among different potassium channels despite a virtually identical selectivity filter and mechanism of ion selection. Understanding this will require in-depth investigation of factors that impact properties of each ion-binding site. If we can determine what gives rise to the difference in ion affinity/selectivity of the different ion-binding sites, then we are certainly one step closer to understanding the age-old problem – the origin of selectivity.

CHAPTER 3

CALCIUM BLOCKAGE IN CYCLIC NUCLEOTIDE-GATED CHANNELS

A. Summary

Cyclic nucleotide-gated (CNG) channels are key components of the visual and olfactory signaling pathways. They are non-selective cation channel permeable to Ca^{2+}, K^{+} and Na^{+}, but preferentially conduct Ca^{2+}. When Ca^{2+} permeates, the monovalent ion current is blocked. This Ca^{2+}-blocking phenomenon is observed in all CNG channels, but to various extents. A glutamate residue in the selectivity filter sequence is known to modulate Ca^{2+} blockage. However, it cannot account for the blockage diversity because the glutamate residue is conserved in most CNG channels. The *Drosophila* CNG channel, for instance, is found to have exceptionally weak calcium blockage despite having the highly conserved glutamate. Interestingly, the selectivity filter sequence of *Drosophila* CNG channel differs at residue 318, having a threonine at that position instead of a proline like most vertebrate CNG channels. To determine if this threonine is associated with the weak Ca^{2+} block in *Drosophila* CNG channel, we took advantage of a previously developed CNG channel pore-modeling system and constructed a chimera channel to model *Drosophila* CNG channel. The selectivity filter sequence of a bacterial sodium potassium channel (NaK) was replaced with that of the *Drosophila* CNG channel, and the resulting mutant was named

NaK2CNG-Dm. The threonine that distinguished *Drosophila* CNG channels from other CNG channels was found to be crucial to the conformation of the selectivity filter of NaK2CNG-Dm and rendered the mutant weakly sensitive to Ca^{2+} blockage. To confirm the importance of this threonine, we replaced it (T318) with proline in *Drosophila* CNG channel. The mutant has a 16 times stronger Ca^{2+} block than the wild-type channel. These results implied that having a threonine instead of proline at residue 318 has likely given rise to a distinct selectivity filter conformation and is the cause of the weak Ca^{2+} blockage in *Drosophila* CNG channel.

B. Literature review

1. Discovery of cyclic nucleotide-gated (CNG) channels

Cyclic nucleotide-gated channels are non-selective cation channels gated by 3', 5'-cyclic adenosine monophosphate (cAMP) or 3', 5'- cyclic guanosine monophosphate (cGMP). The channel was first identified in 1985 as the source of cGMP-dependent conductance in the retina of frog *Rana temporaria* (Fesenko et al., 1985). CNG channels in retinal rod cells play a key role in converting chemical signals induced by photons into electrical ones. Similarly behaved channels were subsequently found in olfactory sensory neurons. In the last three decades, dozens of CNG channels have been cloned and studied in different tissues and organisms. CNG channels are actually very common in animals and plants but relatively rare in prokaryotes.

CNG channels are relatives of voltage-gated potassium channels (Figure 10). They share similar oligomeric states and domain organization. CNG channels are categorized as CNGA or CNGB, and they function as heterotetramers in different combinations of CNGA and CNGB *in vivo*. Except for CNGA4, all CNGAs can form homotetramers and function as ion channels when expressed alone. CNGBs, however, cannot form functional tetramers without CNGA. In terms of domain organization, all CNG channels have a voltage-sensing domain at the N-terminus,

followed by the pore domain and a nucleotide-binding domain at the C-terminus (Figure 18 C). In addition to these three basic domains, some CNG channels have calmodulin-binding domain (Figure 18 C). CNGB1, a CNG channel specifically expressed in rod cells, is unique among all other CNGA and CNGB channels and has a glutamic-acid-rich region at the N-terminus. These extra domains enable the channels to have an additional layer of regulation in channel activities.

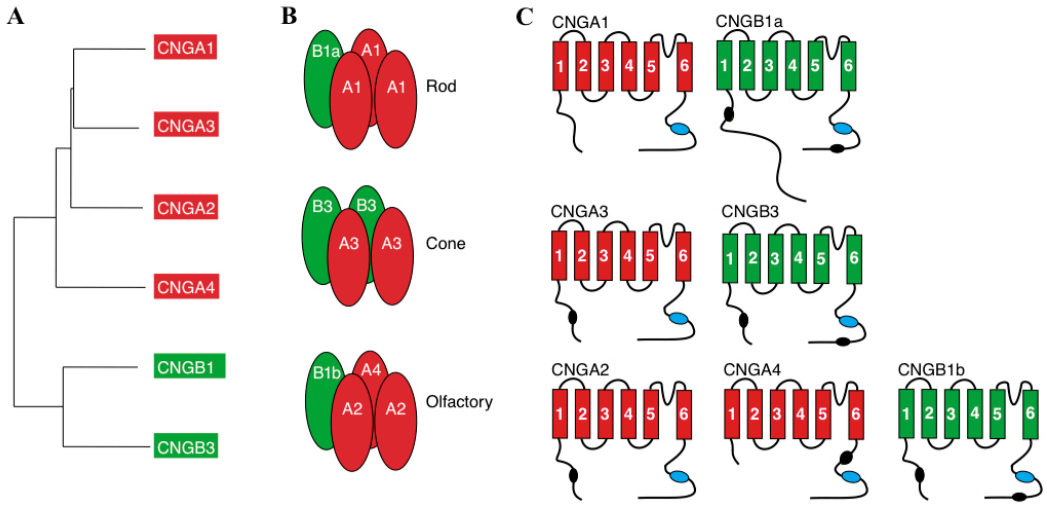

Figure 18. Subunits and stoichiometry of vertebrate CNG channels (Modified from Bradley et al., 2005). (A) Evolutionary relationship of the different CNG channel subunits. (B) Subunit composition of the most well studied CNG channels, rod, cone and olfactory CNG channels. (C) Domain organization and topology of the different CNG channel subunits. The transmembrane domains (TMs) are numbered, and the loop between TM5 and TM6 constitutes the pore of

the channel. Cyclic nucleotide binding domains and calmodulin-binding sites are indicated with blue and black, respectively.

2. Physiological roles

a. Visual signal transduction in vertebrate

The functional roles of CNG channels in visual and olfactory sensory signaling have been thoroughly studied and reviewed (Baylor, 1996; Ashcroft, 2000; Hille, 2001; Chen, 2005). In rod cells, photons induce the activated state of rhodopsin. The activated rhodopsin is enzymatically active and catalyzes the exchange of GDP for GTP in the α-subunit of the G-protein coupled receptor (GPCR). When the α-subunit is GTP-bound, it dissociates from the rest of the GPCR (the β and γ-subunits) and binds to the γ-subunit of a phosphodiesterase. The binding causes another dissociation, in which the γ-subunit of the phosphodiesterase is separated from the α and β subunit of the enzyme. Without the γ-subunit, the phosphodiesterase becomes active and catalyzes the hydrolysis of cGMP into GMP. The reduction of cGMP concentration closes CNG channels on the membrane, blocking the entry of extracellular Na^+ and Ca^{2+}. Meanwhile, the Na^+/Ca^{2+} exchangers continue to export Ca^{2+} outside the cell, resulting in a reduction of intracellular Ca^{2+} concentration and hyperpolarization of the membrane. While the above exchanges and enzymatic activities are highly localized in the outer segment of rod cells, the hyperpolarization relays the signal

to the synapse. This in turn decreases the release of neurotransmitter glutamate, transferring the signals to the neighboring cells. Signal transduction in cones cells follows the same cascade. However, cones cells are less sensitive to light, and the signal transduction is much faster. One of the key differences between the signaling cascade of rod and cone cells is that their CNG channels are made up of different combinations of subunits. CNG channels in rod cells are tetramers of CNGA1 and CNGB1, whereas in cones CNG channels consist of CNGA3 and CNGB3 (Figure 18 B). While this difference is often speculated to be the reason for the differences in the sensitivity and speed of light response between rod and cone cells, no molecular mechanism is currently available to account for it (Frings et al., 1995).

b. Olfactory signal transduction in vertebrate

Odor sensing follows a similar scheme as photon signal transduction in the visual system but varies in details. Activities of ordorant receptors are coupled to GPCR. Upon the binding of an ordorant to an odor receptor, the α-subunit of GPCR becomes GTP-bound and dissociates from the β and γ-subunit (Nakamura, 2000). α-GTP binds to adenylate cyclase, activating it to convert AMP into cAMP. The increase in cAMP concentration opens the nearby CNG channels. As Ca^{2+} enters the cells through CNG channels, the increase in Ca^{2+} concentration opens Ca^{2+}-

gated Cl^- channels. The outward flux of Cl^- depolarizes the cell membrane and triggers an action potential that passes the signal downstream (Pifferi et al., 2006).

c. Plant innate immunity

CNG channels have been implicated as one of the major entry points of Ca^{2+} in plant cells. Ca^{2+} is a critical signaling molecule in various plant signal-transduction cascades. One of the first plant CNG channels identified was AtCNGC2 from the *Arabidopsis thaliana* mutant *dnd1* (death, no defense 1) (Ma, 2011; Moeder et al., 2011). Unlike wild-type plants, *dnd1* mutant doesn't exhibit a hypersensitive response when infected by pathogen. The molecular mechanism of how CNG channels react to bacterial infections is still under active research. Nonetheless, it is clearly crucial for innate immunity because mutants of multiple homologs of CNG channels display phenotypes similar to that of *dnd1*.

3. Gating

Without exception, every monomer of CNG channel has a cyclic nucleotide-binding domain (CNBD). Each domain can bind to one molecule of cNMP (i.e. cGMP and/or cAMP). The opening of the tetrameric channel, however, depends on the degree of saturation of the four CNBDs. In most cases, CNG channels tend to remain in closed state when 1-2 cNMP molecules are bound and open only when 3-4 cNMPs are bound (Ashcroft, 2000). Recently, an exception to this

behavior has been reported. Binding of a single cNMP molecule suffices to open the bacterial CNG channels (Cukkemane et al., 2011). In addition to the differences in gating cooperativity, CNBDs also vary in sensitivity to ligand. Sensitivity, here, is defined as the dose-response to channel opening. CNG channels in olfactory neurons are sensitive to both cGMP and cAMP. In contrast, CNG channels in rod cells are much more sensitive to cGMP than cAMP, while CNG channels in cones are more sensitive to cAMP than cGMP. The K_d's for the binding of cNMP to the cNMP-binding domains of most vertebrate CNG channels were estimated to be in the micromolar level (Cukkemane et al., 2011). The relatively low affinity is thought to be important for a rapid response to the change in cellular cNMP concentrations. Some bacteria and invertebrate CNG channels, on the other hand, was found have nanomolar levels of affinity for cNMP. Although the molecular bases that give rise to all these diversities are not known, different CNG channels have clearly evolved to facilitate their specific functional roles.

4. Ion selectivity and Ca^{2+} blockage

The ion conduction pore of CNG channels has a topology that closely resembles that of the potassium channels. Yet, the selectivity filter sequences of the two channels diverge. Instead of being T(I/V)GYG, the filter sequence of most CNG channels is TIGETPP. The difference makes CNG channels permeable to K^+, Na^+

and Ca^{2+}. Under physiological conditions, CNG channels conduct mainly Na^{+} and Ca^{2+}. One study estimated that 80% of the rod CNG channel current was carried by Na^{+}, 15% by Ca^{2+} and 5% by Mg^{2+} (Yau, 1994). Considering the fact that Na^{+} is 70 times more concentrated than Ca^{2+} in the extracellular region, CNG channels actually have higher permeability to Ca^{2+} than Na^{+}. Such preferential permeation of Ca^{2+} is crucial to visual and olfactory signaling, as both pathways require Ca^{2+} for downstream signaling. The high selectivity for Ca^{2+} is associated with a slow permeation rate of the ion in CNG channels. In the presence of Ca^{2+}, the slow Ca^{2+} permeation rate drastically reduces the Na^{+} current, resulting in an apparent Ca^{2+} block. The small current due to the slow Ca^{2+} permeation is thought to create low membrane potential noise, so that photoreceptor cells can detect light with high sensitivity (Yau and Baylor, 1989).

Ca^{2+} blockage of monovalent ion current is a characteristic of all CNG channels. Properties of this blocking phenomenon have been studied in the last two decades, and the major findings and interpretations are summarized as follow: 1. Ca^{2+} blockage is always voltage-dependent. Maximum blockage occurs at 0 mV, and either depolarization or hyperpolarization can relieve the blocking effect (Picones and Korenbrot, 1995). This observation suggests that Ca^{2+} blocks by interacting with the ion conduction pore. 2. The blockage is pH-dependent (Dzeja et al., 1999), with higher pH correlating with stronger Ca^{2+} blockage. The observation

implies that charged residue(s) with carboxylate group is involved. 3. A glutamate residue in the filter sequence is key to control Ca^{2+} blockage (Eismann et al., 1994). Mutation of the glutamate residue in the filter sequence TIGETPP can modulate the Ca^{2+} blocking effect on CNG channel. Neutralizing this Glu by mutating it to asparagine abolishes Ca^{2+} blockage, while mutating it to aspartate enhances the blocking effect (Root and MacKinnon, 1993). 4. Different CNG channels exhibit a wide range of Ca^{2+} blocking ability (Frings et al., 1995; Picones and Korenbrot, 1995; Dzeja et al., 1999) (Figure 19). Despite the high conservation in sequence, CNG channels in cones are at least two times more permeable to Ca^{2+} compared to CNG channels in rod cells. The higher permeability in cones is speculated to be the reason for the faster signal transduction in cone cells than rod cells (Frings et al., 1995). The molecular basis of the diversity is currently unknown. The research described in this chapter examines one of the reasons for the diversity of Ca^{2+} blocking capability in CNG channels.

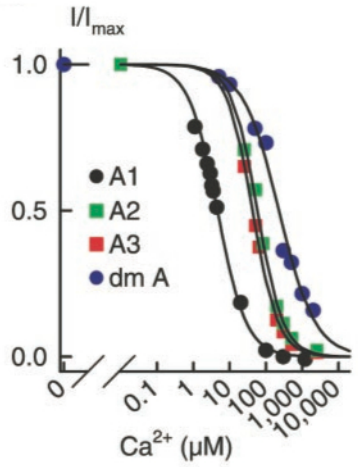

Figure 19. Variability of Ca^{2+} block observed in different CNG subunits (Kaupp and Seifert, 2002). CNGA1 exhibits the most sensitive Ca^{2+} blockage, while *Drosophila* CNGA displays weak Ca^{2+} blockage.

Although structure of CNG channel pore domain is not available, the bacterial sodium potassium channel (NaK) has been used to model the channel pore of vertebrate CNG channels. The topology of NaK is similar to the predicted topology of CNG ion conduction pore, but the selectivity filter sequences differ. To model CNG channels, the selectivity filter sequence of NaK, TVGDGNFSP, was mutated to TVGETPPP (Derebe et al., 2011b) (Figure 20 A). The resulting mutant, termed NaK2CNG-E, has a selectivity filter distinct from both the wild-type NaK and prototypical potassium channels. The unique selectivity filter bears properties of typical CNG channels. NaK2CNG-E is permeable to Na^{+}, K^{+} and Ca^{2+}, and Ca^{2+} promptly blocks monovalent ion current. The Ca^{2+} blockage can

be similarly modulated by changing the glutamate residues in the filter to aspartate (NaK2CNG-D) or asparagine (NaK2CNG-N) (Derebe et al., 2011b) (Figure 20 B-C).

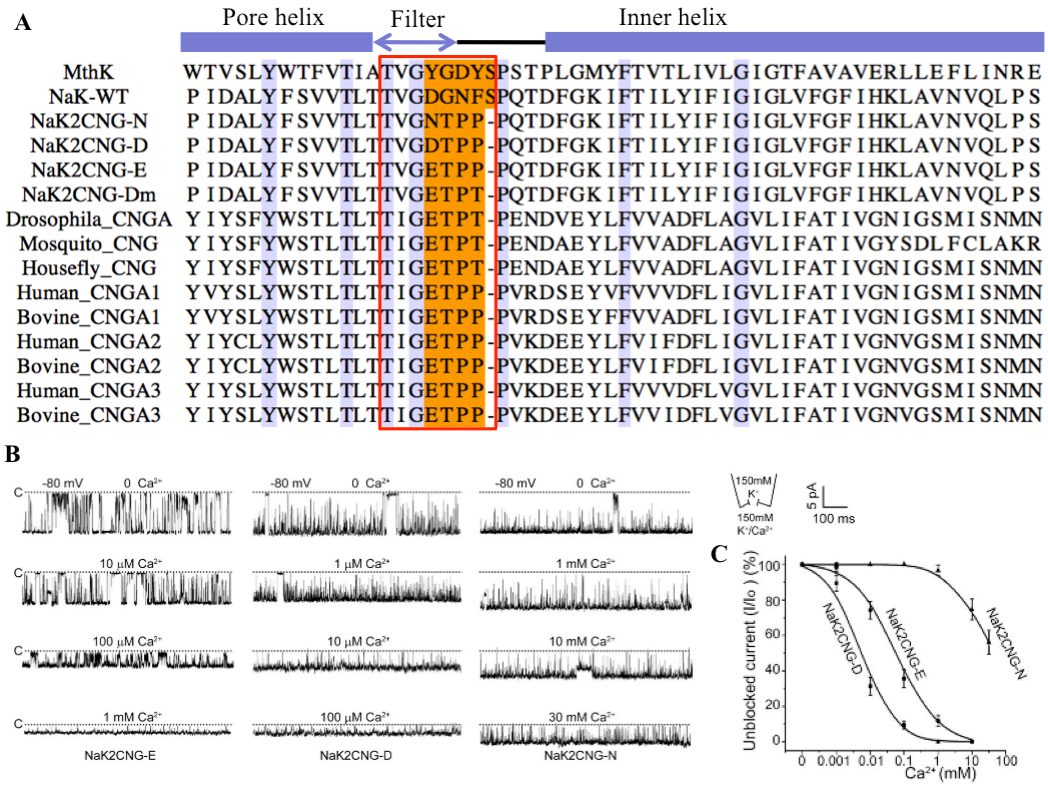

Figure 20. Sequence alignment of potassium and CNG channels and Ca^{2+} blockage of NaK2CNG channels. (A) Partial sequence alignment of potassium channel MthK, NaK, NaK2CNG chimeras, CNG channels of *Drosophila*, mosquito, housefly, human and bovine. Residues conserved in all channels are shaded in violet. Boxed in red are the selectivity filter sequences. Residues shaded in orange in the NaK sequence are replaced by the

respectively shaded residues in CNG channels. (B) Single-channel recordings of NaK2CNG in the presence of various Ca^{2+} concentrations. NaK2CNG-D has the strongest sensitivity to Ca^{2+} blockage, followed by NaK2CNG-E and then NaK2CNG-N. (C) Fraction of unblocked current (I/I_{max}) at -80 mV as a function of Ca^{2+} concentration. NaK2CNG-D is more than 9 times more sensitive to Ca^{2+} blocking than NaK2CNG-E (modified from Derebe et al., 2011b).

As inferred from the structure of NaK2CNG-E, the selectivity filter of CNG channels has three ion-binding sites. The sites are named site 2-4. Site 3 appears to be the major binding site for Ca^{2+} (Derebe et al., 2011b). Interestingly, the glutamate residue that was previously found to control Ca^{2+} blockage does not directly involve in Ca^{2+} binding to the pore. Rather, it maintains the structure of the filter by making important interactions with the pore helix. While it is yet to be confirmed whether this glutamate plays a similar role in wild-type CNG channels, it is unlikely to be the only factor that governs Ca^{2+} blockage. Even though the glutamate is conserved in most CNG channels, the degree of Ca^{2+} blockage can be dramatically different. The half-maximal Ca^{2+} blockage of *Drosophila* CNG channel, for example, was reported to be 10 times weaker than that of bovine rod CNG channels (Dzeja et al., 1999). Additional factors that control Ca^{2+} blockage have yet to be found, but the scope of search should be

limited to the ion conduction pore domain. This is because domain-swapping studies have found that neither the voltage-sensing domain nor the CNBD has any influence on Ca^{2+} blockage. The ion conduction pore alone dictates the Ca^{2+} blockage phenomenon of a CNG channel (Seifert et al., 1999). Taking advantage of this finding, research in this chapter intend to take advantage of NaK, which has a topology similar to that of CNG channels, to understand Ca^{2+} block in CNG channels.

C. Methodology

1. Overall goal and strategy

This study aims to understand the weak Ca^{2+} block in *Drosophila* CNG channels. Although *Drosophila* CNG channel (DmCNGA) has the highly conserved glutamate in its filter sequence, the channel shows weak Ca^{2+} blockage. Sequence alignment of the different CNG channels shows that *Drosophila* and a few other insect CNG channels have a second threonine in the signature sequence, TIGETP**T**P, while most other CNG channels have a proline in the equivalent site, making the sequence TIGETP**P**P. To determine if the presence of threonine in the filter is the cause of the reduced Ca^{2+} blockage in *Drosophila* CNG channels, we created a *Drosophila* CNG channel pore-mimicking mutant of NaK. This NaK mutant contained a filter sequence of TVGETPTP and was named NaK2CNG-Dm. The filter sequence of this mutant and the signature sequence of *Drosophila*, TIGETPTP, differs by one residue at the second position (Val versus Ile), but we expected the difference make no functional or structural difference. This assumption is backed by a previous study on NaK2CNG-E, in which mutants with the filter sequence of TVGETPPP and TIGETPPP share identical structural and functional properties (Derebe et al., 2011b). NaK2CNG-Dm was subjected to structural and functional studies using X-ray crystallography and giant liposome patches. The results were compared to NaK2CNG-E, which mimics the pore of

typical vertebrate CNG channels, and verified with wild-type and mutated *Drosophila* CNGA.

2. Protein expression and purification

NaK2CNG-Dm was generated by making a P69T point mutation of NaK2CNG-E. The construct is in the background of NaKN Δ 19 in vector pQE60. For functional studies, both NaK2CNG-E and NaK2CNG-Dm have an extra F92A mutation, which increased the flux and facilitated channel recording (Alam and Jiang, 2009a, b). All constructs were expressed in *E. coli* XL1blue strain. To achieve optimal expression, 5 mM of $BaCl_2$ was added to media when cells were inoculated. After about 8-10 hours of inoculation at 37 °C, the cell density plateaued at OD = ~0.45. Protein expression was subsequently induced with 0.4 mM IPTG at 25 °C for 16 hours. Cells were then harvest and resuspended in lysis buffer containing 100 mM KCl, 50 mM Tris pH 8.0, DNaseI and protease inhibitors including leupeptin, pepstatin, aprotinin, and PMSF (Sigma). Upon lysis of cells by sonication, the expressed protein was solublized with 40 mM n-decyl- β -D-maltoside (DM) (Anatrace) for 3 hours at room temperature and then centrifuged at 14000 rpm for 25 minutes at 4 °C to remove the insoluble debris. The soluble portion of the lysate was further purified on a Talon Co^{2+} affinity column (Clontech). Protein was eluted upon the addition of lysis buffer containing 300 mM imidazole. The eluted protein was incubated overnight in 4 °C with 2 units of thrombin (Roche)

for the removal of the histidine tag. The cleaved protein was then further purified by a Superdex 200 (10/30) size exclusion column (GE Life Sciences) equilibrated with 100 mM KCl, 20 mM Tris pH 8.0, and 4 mM DM.

3. Protein crystallization, data collection and structural determination

The protein was concentrated to about 15 mg/ml using an Amicon Ultra centrifugal filtration device (50 kDa molecular mass cut-off) and crystallized at 20 °C using the sitting drop vapor diffusion method. Equal volumes of concentrated protein and well solution containing 65–72.5% (v/v) (±)-2-methyl-2, 4-pentanediol (MPD), 100 mM buffer of pH 8-9.5 (Tris • HCl for pH 8.0–8.5 and glycine for pH 9.0-9.5), 100 mM KCl. All crystals were flash-cooled in liquid nitrogen with the crystallization solution serving as the cryoprotectant. All crystals had the symmetry of space group I4 with unit cell dimensions of a = b = 68 Å, c = 89 Å, and contained two protein molecules per asymmetric unit. Multiple X-ray diffraction data sets were collected at various synchrotron facilities and the data used for final refinement were collected at the Advanced Photon Source (APS) beamline 23ID. Diffraction data were processed and scaled in HKL2000 (Otwinowski and Minor, 1997). The structures were determined by molecular replacement in Phenix using the A subunit in the structure of NaK2CNG-E as an initial search model. The initial structure model was refined

by repeated cycles of model refinement using Phenix (Adams et al., 2010). All structural figures were generated in Pymol (Schrodinger, 2010).

Although the channel was crystallized in the presence of K^+ salt, the electron density at site 3 is too strong to be solely K^+, indicating a partial occupancy of a heavy atom. Similar strong density was also observed in NaK channel previously (Alam and Jiang, 2009a). We suspected that the heavy atom contaminant is Ba^{2+}, which is known to bind NaK and K^+ channel pores, and was added to the cell cultures during protein expression. Nevertheless, in this study, the density at site 3 was still model as K^+ for simplicity.

4. Liposome reconstitution and electrophysiology

To compare the functional difference between NaK2CNG-E and NaK2CNG-Dm, constructs with the F92A mutation were purified and reconstituted into liposomes composed of 3:1 (w/w) ratio of 1-palmitoyl-2-oleoyl-phospha-tidylethanolamine (POPE) and 1-palmitoyl-2-oleoyl-phosphatidylglycerol (POPG) (Avanti Polar Lipids). The lipid mixture was first air dried in argon gas and then further dried in a SpeedVac for 1.5 – 2 hours. Dried lipid was resuspended in 100 mM KCl and 20 mM Tris pH 8.0. To ensure proper mixing, lipids were sonicated in a water bath until the solution turned clear; it was then incubated with 10 mM DM for two hours. Purified proteins were then added into the lipid mixture in a protein/lipid

ratio of 0.1-1 μg⁄mg. Reconstituted liposomes were dialyzed in 1 liter of 100 mM KCl, 20 mM Tris pH 8.0 for 72 hours, with buffer change every 24 hours. After dialysis, liposomes were stored in -80 °C.

Single-channel currents were recorded on proteoliposomes using giant liposome patch clamp method. To make giant liposome, proteoliposomes at 1:1000-10000 (w/w) protein to lipid ratio were air dried on a clean coverslip overnight at 4 °C and then rehydrated with bath solution at room temperature. The standard bath solution contained 150 mM KCl, 0.5 mM EGTA, 10 mM HEPES-KOH pH 7.4. In the study of extracellular Ca^{2+} blocking, various concentrations of Ca^{2+} were added to the bath solution. The free Ca^{2+} concentration in the range of 0–100 μM was controlled by mixing 5 mM EGTA with an appropriate amount of $CaCl_2$ calculated using the software MAXCHELATOR (Patton et al., 2004; Bers et al., 2010). No EGTA was added in the bath solution for [Ca^{2+}] above 100 μM. The patch pipettes were pulled from Borosilicate glass (Harvard Apparatus) with a resistance of 8–12 MΩ and filled with 150 mM NaCl, 0.5 mM EGTA, 10 mM HEPES-NaOH pH 7.4. The patch pipette was then attached to the giant liposome. With gentle suction, a gigaseal (>10 GΩ) was formed. To get a single layer of membrane patch, the pipette was pulled away from the giant liposome, and the patch pipette tip was exposed to air for 1–2 sec. Owing to the two possible orientations of reconstituted NaK2CNG mutants in the liposomes, 30 μM TPeA,

an intracellular pore blocker for NaK CNG channels, was also added in the bath solution to ensure that the channel in the recording had its extracellular side facing the bath solution. Data were acquired using an AxoPatch 200B amplifier (Molecular Devices) with the low-pass analogue filter set to 1 kHz. The current signal was sampled at a rate of 20 kHz using a Digidata 1322A digitizer (Molecular Devices) and further analyzed with pClamp 9 software (Molecular Devices).

5. Functional expression in HEK 293 cells

Drosophila and bovine CNG channels were individually cloned into pEGFP-C1 vector. The T318P mutation in *Drosophila* and P366T mutation in bovine CNG channels were subsequently generated from a polymerase chain reaction using Pfu Turbo Polymerase (Agilent) and primers containing the mutations. HEK 293 cells were used to express *Drosophila* or bovine CNG-GFP fusion protein and measure CNG channels current. Cells transiently transfected with plasmids using lipofectamine 2000 (Invitrogen) according to the manufacturer's manual. Recordings were performed 24–48 hrs after the transfection. For the outside-out and whole-cell configurations, the pipette contained 140 mM KCl, 5 mM EGTA, 10 mM HEPES pH 7.4 and 1 mM cGMP. For the inside-out and cell-attach configurations, the pipette contained 140 mM NaCl, 4 mM KCl, 1 mM EGTA, 10 mM HEPES pH 7.4, while the bath solution contained 140 mM KCl, 5 mM

EGTA, 10 mM HEPES pH 7.4. The bath solution contained 140 mM NaCl, 4 mM KCl, 1 mM EGTA, 10 mM HEPES pH 7.4. For the extracellular Ca^{2+}-blocking study, various concentrations of Ca^{2+} were added to the bath solution. The free Ca^{2+} concentration in the range of 0–100 μM were controlled by mixing 5 mM EGTA with an appropriate amount of $CaCl_2$ as described in section C.4 above. Data were also acquired using identical methods as described in section C.4 above.

D. Results

1. NaK2CNG-Dm has a unique filter structure

To model the *Drosophila* CNG channel pore, we replaced the selectivity filter of NaK with that of *Drosophila* CNG channel and named the construct NaK2CNG-Dm. NaK2CNG-Dm has a filter sequence of $_{63}$TVGETPT$_{69}$, which, in essence, is a P69T mutation of NaK2CNG-E. The structure of NaK2CNG-Dm in complex with K^+ was determined at a resolution of 1.9 Å (Table 2). While NaK2CNG-Dm maintains the same overall structure as NaK (Figure 21 A), the selectivity filter of NaK2CNG-Dm adopts a novel conformation distinct from that of wild-type NaK, our previous NaK2CNG chimeras, and potassium channel NaK2K (Figure 21 B-C). The first two filter residues (Thr63 and Val64) of NaK2CNG-Dm form two ion-binding sites (site 3 & 4) at the internal half of the filter, which are virtually identical to those of other channels. However, the NaK2CNG-Dm filter has a unique external half, where the $_{65}$GET filter residues adopt a novel main-chain conformation and generate a funnel-shaped entrance filled with layers of ordered water molecules and hydrated K^+ ions (Figure 21 B). This entrance is much wider than that of the other NaK2CNG mutants such as NaK2CNG-E, to which the detailed structural comparison will be made below.

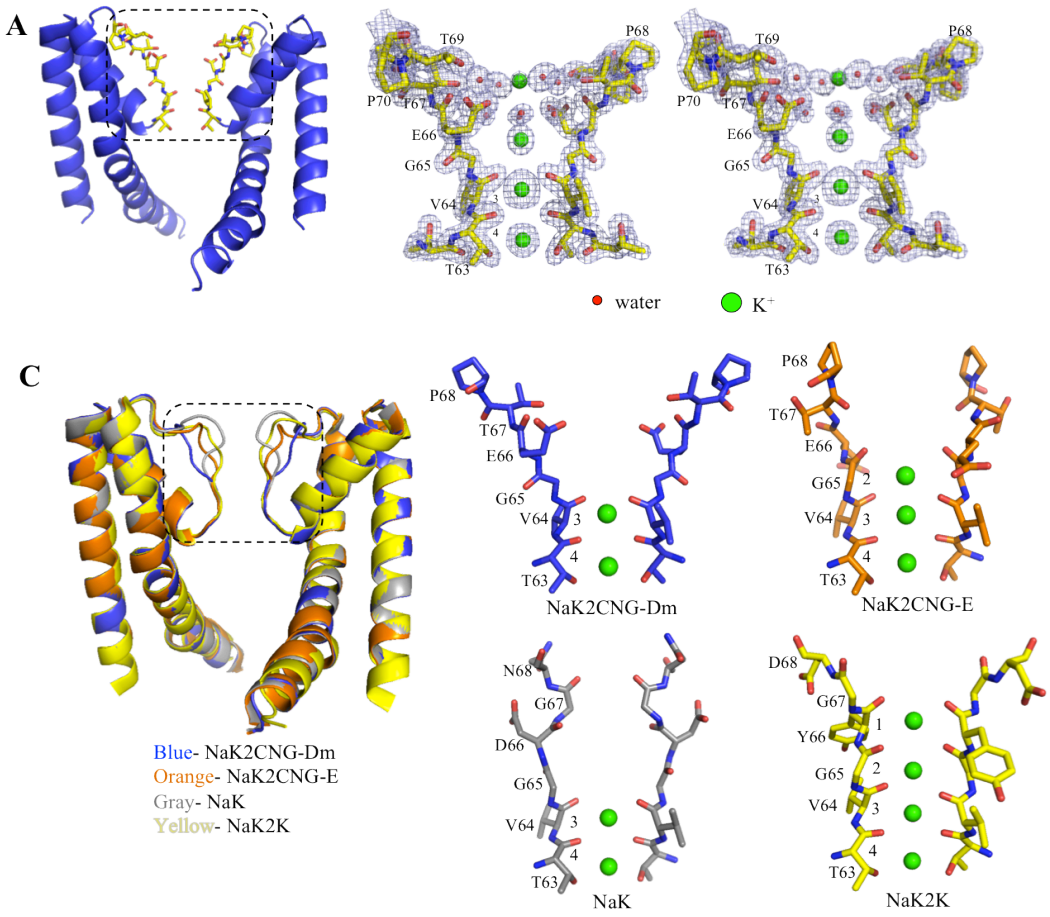

Figure 21. Structure of NaK2CNG-Dm. (A) Overall structure of NaK2CNG-Dm with front and back subunit removed for clarity. (B) A stereo view of the selectivity filter region boxed in (A). A $2F_o$-F_c (2σ) electron density map is shown in mesh. (C) Superimposition of NaK2CNG-Dm (blue), NaK2CNG-E (orange), wt NaK (gray) and potassium channel NaK2K (yellow) shows that the four channels differ mainly at the filter region (boxed). (D) The selectivity filters of NaK2CNG-Dm, NaK2CNG-E, NaK and NaK2K adopt different conformations at the external half and consequently have varying numbers of ion-binding sites.

Although NaK2CNG-E and NaK2CNG-Dm differs only at residue 69, the major structural divergence occurs at the $_{65}$GET region, several residues before Thr69 where both channels have identical sequence. As shown in the structural superimposition, the $_{65}$GET peptides of the two channel filters adopt a nearly inverted main chain conformation, and the structural change involves an almost 180^{o} rotation of the GET peptide with the pivot point at the Ca of Gly65 (Figure 22 A). Consequently, there are four major structural differences between the filters of the two channels. First, in NaK2CNG-E, the backbone carbonyl oxygen atom of Gly65 points towards the center of the ion-permeation pathway and forms the top layer of the ion ligand at site 2, yet in NaK2CNG-Dm, it flips away from the center, abolishing the ion-binding site. Second, the side chain of Glu66 points downward towards the pore helix in NaK2CNG-E but points outward to the external solution and lies on the surface of external funnel entrance in NaK2CNG-Dm. Third, the reorientation of Glu66 is associated with the formation of a completely new set of packing interactions (Figure 22 B-C). In NaK2CNG-E, the Glu66 carboxylate side chain forms hydrogen bonds with Thr60 of the neighboring subunit and its backbone carbonyl forms a hydrogen bond with Tyr55 of the same subunit. In NaK2CNG-Dm, the carboxylate group of Glu66 forms a new hydrogen-bonding network with Thr67 and Tyr55 of the neighboring subunit as well as Thr69 of the same subunit. Fourth, to accommodate the

dramatic main-chain conformational change, the peptide bond between Thr67 and Pro68 changes from the trans configuration in NaK2CNG-E to the cis configuration in NaK2CNG-Dm. The significance of all these structural differences can be implied from the differences in the ion-permeation properties between the two channels as described below.

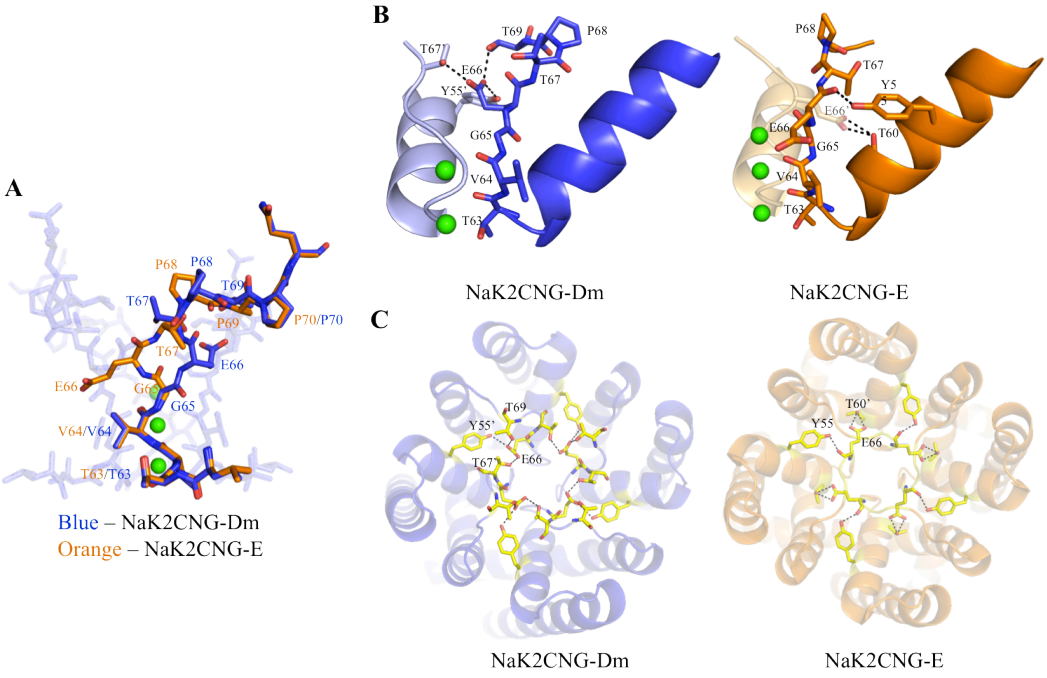

Figure 22. Structural comparison of NaK2CNG-Dm and NaK2CNG-E. (A) Superimposition of NaK2CNG-Dm (blue) and NaK2CNG-E (orange) at the selectivity filter region, showing the divergence of the main-chain backbones at the $_{65}$GET region. The superimposition is highlighted for the front subunit and the other subunits of NaK2CNG-Dm are shaded in light blue in the background. (B)

Comparison of the selectivity filter of one subunit from NaK2CNG-Dm and NaK2CNG-E. Dashed lines indicate the hydrogen bonds between Glu66 and surrounding residues. Residues from a neighboring subunit are marked with single quotation marks. (C) A comparison of the hydrogen-bonding network of NaK2CNG-Dm and NaK2CNG-E viewing from the external side of the channel tetramers. Residues involved in the hydrogen bonds are displayed as yellow sticks.

Table 2. Data collection and refinement statistics of NaK2CNG-Dm

Statistic	NaK2CNG-Dm
Data Collection	
Space group	I_4
Cell Dimensions a=b, c (Å)	67.907, 89.799
Wavelength (Å)	1.0000
Resolution (Å)	50 - 1.90
R_{sym} (%)	8.6 (66.8)
$I/\sigma I$	19.0 (0.97)
No. of reflections- total (unique)	283595 (15224)
Completeness (%)	95
Refinement	
Redundancy	6.5 (2.2)
Resolution (Å)	1.90
R_{work}/R_{free}	0.2038/0.2361
No. of atoms	
Protein	1448
ion	7
Water	102
R.m.s.d.	
Bond angles (°)	0.966
Bond lengths (Å)	0.005
Values in parenthesis are for the highest resolution shell. 5% of the data were used in the R_{free} calculation.	

2. Ion permeation and Ca^{2+} blockage in NaK2CNG-Dm.

The giant liposome patch clamp method was employed to assay the ion-permeation and Ca^{2+}-blocking properties of the NaK2CNG-Dm channel. Similar to NaK2CNG-E, NaK2CNG-Dm has a high open probability and exhibits some subconductance states (Figure 23 A). Under a bi-ionic condition with 150 mM KCl in the bath and 150 mM NaCl in the pipette, NaK2CNG-Dm has a single-channel conductance of about 56 pS for inward K^+ current at -100 mV, significantly smaller than that of NaK2CNG-E (~100 pS) previously measured under the same condition (Derebe et al., 2011b). Interestingly, NaK2CNG-Dm is weakly selective for K^+ with a reversal potential of 25 mV, corresponding to P_K/P_{Na} of about 2.7 (Figure 23 B). This is in contrast to NaK2CNG-E, which was previously reported to be non-selective (Derebe et al., 2011b). The Ca^{2+} blockage of NaK2CNG-Dm was measured with various concentrations of Ca^{2+} added to the external side of the channel (i.e. the bath solution). As shown in Figure 23 C and D, Ca^{2+} only weakly blocked the monovalent ion current in NaK2CNG-Dm with a K_i of about 4 ± 0.6 mM, which is in stark contrast with the K_i of 59 ± 10 μM in NaK2CNG-E.

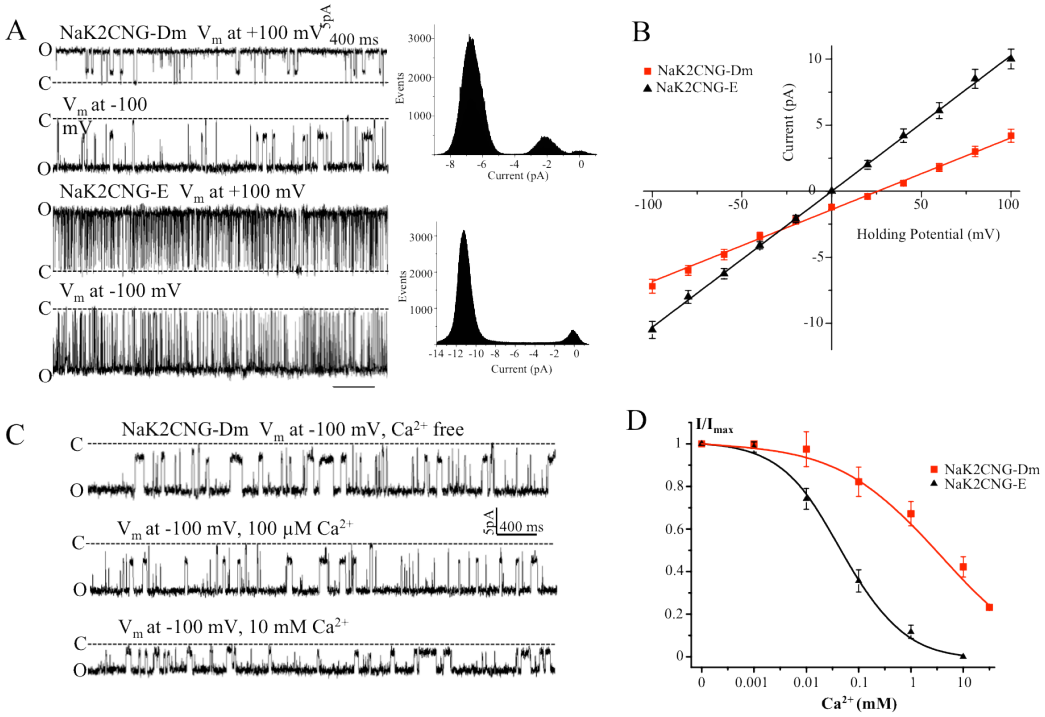

Figure 23. Ion conduction and Ca^{2+} block of NaK2CNG-Dm. (A) *Left* Sample traces of single-channel recordings of NaK2CNG-Dm and NaK2CNG-E at ± 100 mV. *Right* Histogram of single-channel current at -100 mV. (B) Ion selectivity and conductance of NaK2CNG-Dm and NaK2CNG-E are compared in a I/V plot. Each point is the mean ± SEM of 5 independent measurements. (C) Sample traces of single-channel recordings at -100 mV at different external (bath) Ca^{2+} concentrations. (D) Fraction of unblocked current (I/I_{max}) at -100 mV as a function of Ca^{2+} concentration. Data are fitted to the Hill equation with K_i of 4 ± 0.6 mM and Hill coefficient n of 0.52 for

NaK2CNG-Dm and K_i of 59 ± 10 μM and n of 0.98 for NaK2CNG-E. Data points are mean ± SEM from 5 measurements.

3. T318P mutation strengthens Ca^{2+} blockage in *Drosophila* CNG channels

To test if the presence of threonine instead of proline is responsible for the weak Ca^{2+} blockage in *Drosophila* CNG channel as in the NaK2CNG model system, we mutated threonine 318 (equivalent to T69 in NaK2CNG-Dm) in DmCNGA to proline (T318P) so that its filter sequence became TIGETP$\underline{P}_{318}$P. The mutant channel was heterologously expressed in HEK293 cells. Single-channel recordings in the cell-attached configuration demonstrated that the mutant channel has kinetic properties similar to those of the wild-type channel, but the single-channel conductance increased from 17 pS in the wild-type channel to 21 pS in T318P mutant at -100 mV (Figure 24 A). The dose response to cGMP-regulated gating, on the other hand, was not affected by the mutation, as confirmed by the $[cGMP]_i$-dependent inward currents in inside-out patches (Figure 24 B). However, based on the whole-cell recording results, the single mutation resulted in a significant enhancement in external Ca^{2+} blockage as demonstrated in the I-V curves of wt DmCNGA and T318P mutant in the presence of varying external $[Ca^{2+}]$ (Figure 24 C). A fit of the unblocked inward current at -80 mV as a function of external $[Ca^{2+}]$ yields a K_i of 229 ± 25 μM for wild-type DmCNGA and 13.7 ± 2.2 μM for the T318P mutant (Figure 24 D). The 16-fold increase in

Ca^{2+}-block is a reminiscent of the difference in Ca^{2+}-blocking sensitivity between NaK2CNG-E and NaK2CNG-Dm, implying that the altered filter structure observed in NaK2CNG-Dm is probably the reason for the weak Ca^{2+} blockage in *Drosophila* CNGA.

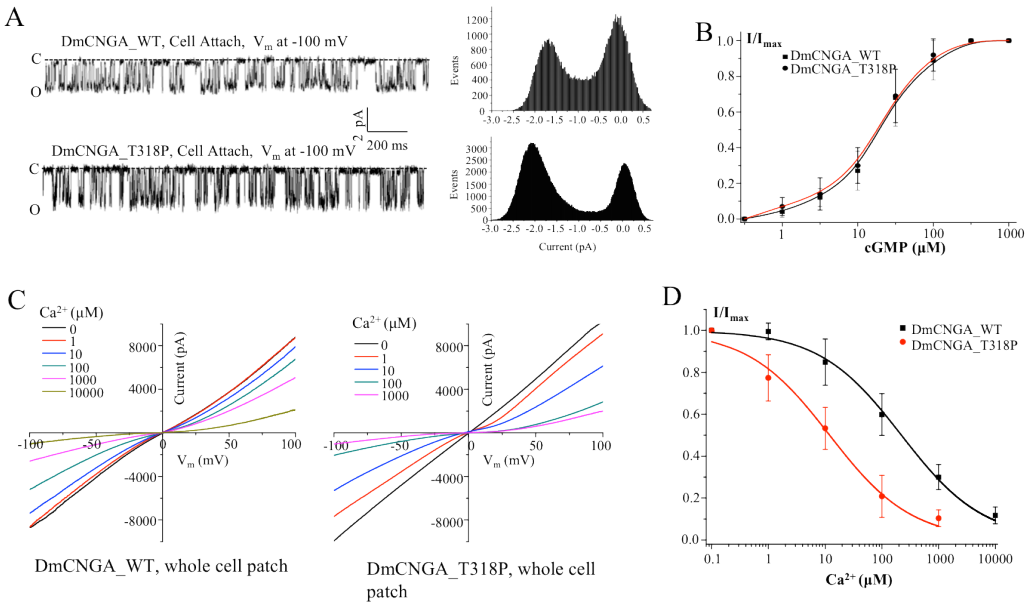

Figure 24. Functional comparison of DmCNGA and T318P mutant. (A) *Left*: Sample traces of single-channel recordings of DmCNGA and T318P mutant at -100 mV in cell-attached configuration. *Right:* Histogram of single-channel current at -100 mV. (B) Normalized macroscopic currents of wild-type DmCNGA and the T318P mutant as a function of $[cGMP]_i$ measured in inside-out patches at -100 mV. Data are fitted to the Hill equation. The $K_{1/2}$ and n of DmCNGA are 16.4 ± 1.8 μM and 1.3, respectively. The $K_{1/2}$ and n of T318P mutant are 15.2 ± 2.1 μM

and 1.2 respectively. (C) I/V curves of DmCNGA and T318P mutant measured from whole-cell recordings at different external (bath) Ca^{2+} concentrations. (D) Fraction of unblocked current (I/I_{max}) at -100 mV as a function of external Ca^{2+} concentration. Data are fitted into Hill equation with K_i of 229.5 ± 25 μM and n of 0.62 for DmCNGA and K_i of 13.7 ± 2.2 μM and n of 0.59 for T318P. All data points presented are mean ± SEM from 5 measurements.

4. P366T mutation has weak affect Ca^{2+} blockage in bovine CNGA1.

Since threonine 318 in *Drosophila* was found to be the key in gauging Ca^{2+} blockage, we asked whether the equivalent residue in mammalian CNG channels is important for the blockage. This was tested on bovine CNGA1 channel by replacing the equivalent proline (P366) with threonine, resulting in a selectivity filter sequence of TIGETPTP. The P366T mutation in bovine CNGA1 has no obvious effect on single-channel conductance and kinetics or cGMP-regulated gating (Figure 25 A-B). However, contrary to our prediction based on the NaK2CNG mutants as well as the mutation on *Drosophila* CNGA, the Pro-to-Thr replacement in bovine CNGA1 has almost no effect on Ca^{2+} blockage. Outside-out patch recordings show that mutation only results in a subtle decrease of Ca^{2+} affinity (K_i = 3.5 ± 0.5 μM for the wild-type channel and K_i = 6.0 ± 0.7 μM for P366T) (Figure 25 C-D), suggesting that the equivalent Thr/Pro swap in

CNGA1 does not compromise the structure integrity of the filter, and the channel thereby retains its strong Ca^{2+} blockage.

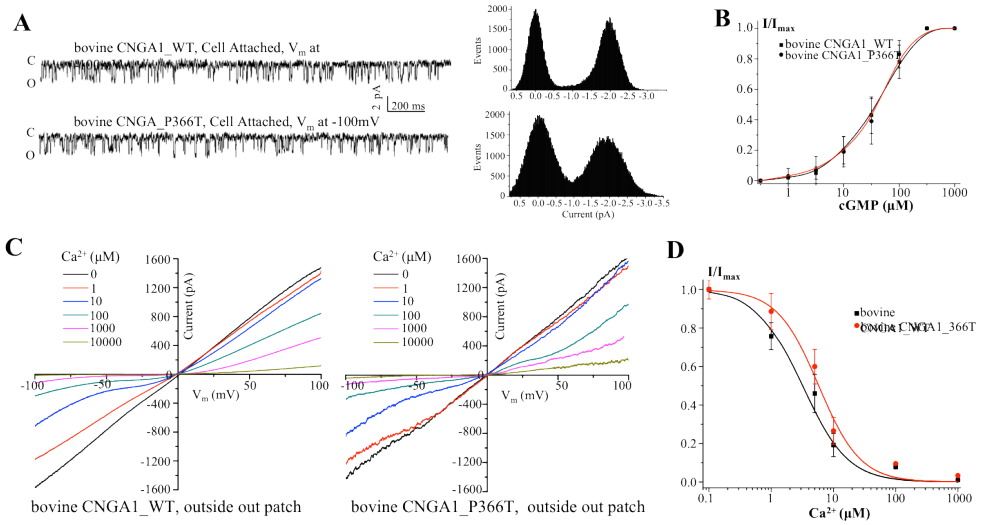

Figure 25. Functional comparison of bovine CNGA1 and P366T mutant. (A) *Left:* Sample traces of single-channel recordings of bovineCNGA1 and P366T at -100 mV in cell-attached configuration. *Right:* Histogram of single-channel current at -100 mV. (B) Normalized macroscopic currents of wild-type bovine CNGA1 and P366T mutant as a function of $[cGMP]_i$ measured in inside-out patches at -100 mV. Data are fitted to the Hill equation. The $K_{1/2}$ and n of bovineCNGA1 are 39.5 ± 3.6 μM and 1.2 respectively. The $K_{1/2}$ and n of P366T are 41.2 ± 4.7 μM and 1.3 respectively. (C) I/V curves of bovineCNGA1 and P366T mutant measured from outside-out patches at different external (bath) Ca^{2+} concentrations. (D) Fraction of unblocked current (I/I_{max}) at -100 mV as a function of Ca^{2+}

concentration. Data are fitted into Hill equation with K_i of 3.5 ± 0.5 μM and n of 1.03 for bovine CNGA1 and K_i of 6.0 ± 0.7 μM and n of 1.36 for P366T. All data points presented are mean ± SEM from 5 measurements.

E. Discussions

This study aims to understand the weak Ca^{2+} block observed in *Drosophila* CNG channels (Baumann et al., 1994; Dzeja et al., 1999). Ca^{2+} blocks monovalent ion current to different degree in different CNG channels, and such variation is often seen as an adaptation for the particular function that a CNG channel serves. Although a glutamate residue in the selectivity filter sequence is known to control Ca^{2+} blockage in the selectivity filter, this residue alone cannot account for the diversity of Ca^{2+}-blocking efficacies because it is conserved in almost all CNG channels (Root and MacKinnon, 1993; Eismann et al., 1994; Dzeja et al., 1999; Gavazzo et al., 2000). Hence, there must be other residue(s) that modulates Ca^{2+} blockage and permeability in CNG channels.

Hinted at by a sequence alignment that reveals a one-residue difference in the selectivity filter sequences between *Drosophila* and most other vertebrate CNG channels, we set out to determine if the difference in sequence has a functional consequence. By modeling *Drosophila* CNG channel pore with NaK2CNG-Dm, we were able to gain structural insights on the origins of the weak Ca^{2+} block in *Drosophila*. The selectivity filter of NaK2CNG-Dm adopts a conformation distinct from NaK2CNG-E, the NaK mutant that mimics typical vertebrate CNG channels. Based on the electrophysiology studies, this unique filter structure is associated with a 14-times weaker Ca^{2+} block compared to NaK2CNG-E. Such a

dramatic change in structure and Ca^{2+} block were unexpected, considering that there was only a single proline to threonine mutation immediately outside of the selectivity filter.

One possible reason for the conformational change is the difference in structural flexibility. The selectivity filter sequence of canonical CNG channels, TIGETPPP, has three consecutive proline residues. Given the unique side chain of proline, the structure of that region is likely to be rigid and restricted. *Drosophila* CNG channels, which have a threonine in place of the middle proline (i.e. TIGETPTP), probably enjoy a considerably larger degree of freedom at that particular region. Even though this threonine is not positioned inside the ion conduction pore, it is pivotal to the conformation of the selectivity filter.

NaK2CNG-Dm has qualitatively recapitulated the weak Ca^{2+} block observed in *Drosophila* CNG channel. This implies that *Drosophila* CNG channels may have a selectivity filter different from canonical CNG channels because of the threonine. To confirm the importance of the threonine, threonine 318 in *Drosophila* CNGA was replaced with proline. A 16-fold increase in Ca^{2+} blockage was observed in DmCNGA T318P mutant as well as a moderate increase in single-channel conductance. This gain of function phenotype strongly

supports the argument that the weak Ca^{2+} block of *Drosophila* CNG channels may be ascribed to its unique filter structure.

Interestingly, the equivalent mutation in bovine CNGA1, P366T, did not exhibit reduced Ca^{2+} block and behaved like the wild-type channel. This indicates that the selectivity filter of P366T mutant is mostly likely identical to that of the wild-type channel. As Ca^{2+} blockage of CNG channels appears to be governed by multiple factors and residues, this result is not entirely unexpected. There may be additional structural elements in DmCNGA and NaK that permit the significantly altered conformation of the selectivity filter that are not available in bovine CNGA1. Since most selectivity filters of CNG channels are highly similar in sequence, future studies should focus on residues that are outside of the selectivity filter but interact with residues inside or surrounding the filter. These residues are likely to exert an impact on the conformation and charge on the filter, and thus the best candidates to provide leads that will allow us to further dissect the mechanism of Ca^{2+} blockage in CNG channels.

BIBLIOGRAPHY

Adams, P.D., P.V. Afonine, G. Bunkoczi, V.B. Chen, I.W. Davis, N. Echols, J.J. Headd, L.W. Hung, G.J. Kapral, R.W. Grosse-Kunstleve, A.J. McCoy, N.W. Moriarty, R. Oeffner, R.J. Read, D.C. Richardson, J.S. Richardson, T.C. Terwilliger, and P.H. Zwart. 2010. PHENIX: a comprehensive Python-based system for macromolecular structure solution. *Acta crystallographica. Section D, Biological crystallography*. 66:213-221.

Alam, A., and Y. Jiang. 2009a. High-resolution structure of the open NaK channel. *Nature structural & molecular biology*. 16:30-34.

Alam, A., and Y. Jiang. 2009b. Structural analysis of ion selectivity in the NaK channel. *Nature structural & molecular biology*. 16:35-41.

Alam, A., and Y. Jiang. 2011. Structural studies of ion selectivity in tetrameric cation channels. *The Journal of general physiology*. 137:397-403.

Alexander, S.P., H.E. Benson, E. Faccenda, A.J. Pawson, J.L. Sharman, W.A. Catterall, M. Spedding, J.A. Peters, A.J. Harmar, and C. Collaborators. 2013. The Concise Guide to PHARMACOLOGY 2013/14: ion channels. *British journal of pharmacology*. 170:1607-1651.

Andersen, O.S. 2011. Perspectives on: Ion selectivity. *The Journal of general physiology*. 137:393-395.

Armstrong, C.M., R.P. Swenson, Jr., and S.R. Taylor. 1982. Block of squid axon K channels by internally and externally applied barium ions. *The Journal of general physiology*. 80:663-682.

Armstrong, C.M., and S.R. Taylor. 1980. Interaction of barium ions with potassium channels in squid giant axons. *Biophysical journal*. 30:473-488.

Ashcroft, F.M. 2000. Ion channels and disease : channelopathies. Academic Press, San Diego. xxi, 481 p. pp.

Baker, R.P., K. Young, L. Feng, Y. Shi, and S. Urban. 2007. Enzymatic analysis of a rhomboid intramembrane protease implicates transmembrane helix 5 as the lateral substrate gate. *Proceedings of the National Academy of Sciences of the United States of America*. 104:8257-8262.

Baumann, A., S. Frings, M. Godde, R. Seifert, and U.B. Kaupp. 1994. Primary structure and functional expression of a Drosophila cyclic nucleotide-gated channel present in eyes and antennae. *The EMBO journal*. 13:5040-5050.

Baylor, D. 1996. How photons start vision. *Proceedings of the National Academy of Sciences of the United States of America*. 93:560-565.

Behrends, J.C. 2012. Evolution of the ion channel concept: the historical perspective. *Chemical reviews*. 112:6218-6226.

Ben-Shem, A., D. Fass, and E. Bibi. 2007. Structural basis for intramembrane proteolysis by rhomboid serine proteases. *Proceedings of the National Academy of Sciences of the United States of America*. 104:462-466.
Berneche, S., and B. Roux. 2000. Molecular dynamics of the KcsA K(+) channel in a bilayer membrane. *Biophysical journal*. 78:2900-2917.
Bers, D.M., C.W. Patton, and R. Nuccitelli. 2010. A practical guide to the preparation of Ca(2+) buffers. *Methods in cell biology*. 99:1-26.
Bradley, J., J. Reisert, and S. Frings. 2005. Regulation of cyclic nucleotide-gated channels. *Current opinion in neurobiology*. 15:343-349.
Bray, S.J. 2006. Notch signalling: a simple pathway becomes complex. *Nature reviews. Molecular cell biology*. 7:678-689.
Brooks, C.L., C. Lazareno-Saez, J.S. Lamoureux, M.W. Mak, and M.J. Lemieux. 2011. Insights into substrate gating in H. influenzae rhomboid. *Journal of molecular biology*. 407:687-697.
Brown, M.S., and J.L. Goldstein. 1997. The SREBP pathway: regulation of cholesterol metabolism by proteolysis of a membrane-bound transcription factor. *Cell*. 89:331-340.
Brown, M.S., J. Ye, R.B. Rawson, and J.L. Goldstein. 2000. Regulated intramembrane proteolysis: a control mechanism conserved from bacteria to humans. *Cell*. 100:391-398.
Chen, C.K. 2005. The vertebrate phototransduction cascade: amplification and termination mechanisms. *Reviews of physiology, biochemistry and pharmacology*. 154:101-121.
Chiang, P.M., R.R. Fortna, D.L. Price, T. Li, and P.C. Wong. 2012. Specific domains in anterior pharynx-defective 1 determine its intramembrane interactions with nicastrin and presenilin. *Neurobiology of aging*. 33:277-285.
Cukkemane, A., R. Seifert, and U.B. Kaupp. 2011. Cooperative and uncooperative cyclic-nucleotide-gated ion channels. *Trends in biochemical sciences*. 36:55-64.
De Strooper, B. 2003. Aph-1, Pen-2, and Nicastrin with Presenilin generate an active gamma-Secretase complex. *Neuron*. 38:9-12.
Deng, M., Z. Lu, J. Zheng, X. Wan, X. Chen, K. Hirayasu, H. Sun, Y. Lam, L. Chen, Q. Wang, C. Song, N. Huang, G.F. Gao, Y. Jiang, H. Arase, and C.C. Zhang. 2014. A motif in LILRB2 critical for Angptl2 binding and activation. *Blood*. 124:924-935.
Derebe, M.G., D.B. Sauer, W. Zeng, A. Alam, N. Shi, and Y. Jiang. 2011a. Tuning the ion selectivity of tetrameric cation channels by changing the number of ion binding sites. *Proceedings of the National Academy of Sciences of the United States of America*. 108:598-602.

Derebe, M.G., W. Zeng, Y. Li, A. Alam, and Y. Jiang. 2011b. Structural studies of ion permeation and Ca2+ blockage of a bacterial channel mimicking the cyclic nucleotide-gated channel pore. *Proceedings of the National Academy of Sciences of the United States of America*. 108:592-597.

Dixit, P.D., and D. Asthagiri. 2011a. The role of bulk protein in local models of ion-binding to proteins: comparative study of KcsA, its semisynthetic analog with a locked-in binding site, and valinomycin. *Biophysical journal*. 100:1542-1549.

Dixit, P.D., and D. Asthagiri. 2011b. Thermodynamics of ion selectivity in the KcsA K+ channel. *The Journal of general physiology*. 137:427-433.

Dixit, P.D., S. Merchant, and D. Asthagiri. 2009. Ion selectivity in the KcsA potassium channel from the perspective of the ion binding site. *Biophysical journal*. 96:2138-2145.

Doyle, D.A., J. Morais Cabral, R.A. Pfuetzner, A. Kuo, J.M. Gulbis, S.L. Cohen, B.T. Chait, and R. MacKinnon. 1998. The structure of the potassium channel: molecular basis of K+ conduction and selectivity. *Science*. 280:69-77.

Dries, D.R., S. Shah, Y.H. Han, C. Yu, S. Yu, M.S. Shearman, and G. Yu. 2009. Glu-333 of nicastrin directly participates in gamma-secretase activity. *The Journal of biological chemistry*. 284:29714-29724.

Dzeja, C., V. Hagen, U.B. Kaupp, and S. Frings. 1999. Ca2+ permeation in cyclic nucleotide-gated channels. *The EMBO journal*. 18:131-144.

Eismann, E., F. Muller, S.H. Heinemann, and U.B. Kaupp. 1994. A single negative charge within the pore region of a cGMP-gated channel controls rectification, Ca2+ blockage, and ionic selectivity. *Proceedings of the National Academy of Sciences of the United States of America*. 91:1109-1113.

Emsley, P., and K. Cowtan. 2004. Coot: model-building tools for molecular graphics. *Acta Crystallogr D Biol Crystallogr*. 60:2126-2132.

Feng, L., H. Yan, Z. Wu, N. Yan, Z. Wang, P.D. Jeffrey, and Y. Shi. 2007. Structure of a site-2 protease family intramembrane metalloprotease. *Science*. 318:1608-1612.

Fesenko, E.E., S.S. Kolesnikov, and A.L. Lyubarsky. 1985. Induction by cyclic GMP of cationic conductance in plasma membrane of retinal rod outer segment. *Nature*. 313:310-313.

French, R.J., and J.J. Shoukimas. 1985. An ion's view of the potassium channel. The structure of the permeation pathway as sensed by a variety of blocking ions. *The Journal of general physiology*. 85:669-698.

Frings, S., R. Seifert, M. Godde, and U.B. Kaupp. 1995. Profoundly different calcium permeation and blockage determine the specific function of distinct cyclic nucleotide-gated channels. *Neuron*. 15:169-179.

Gavazzo, P., C. Picco, E. Eismann, U.B. Kaupp, and A. Menini. 2000. A point mutation in the pore region alters gating, Ca(2+) blockage, and permeation of olfactory cyclic nucleotide-gated channels. *The Journal of general physiology*. 116:311-326.

Grant, P., Y. Zheng, and H.C. Pant. 2006. Squid (Loligo pealei) giant fiber system: a model for studying neurodegeneration and dementia? *The Biological bulletin*. 210:318-333.

Guo, R., W. Zeng, H. Cui, L. Chen, and S. Ye. 2014. Ionic interactions of Ba2+ blockades in the MthK K+ channel. *The Journal of general physiology*. 144:193-200.

Haapasalo, A., and D.M. Kovacs. 2011. The many substrates of presenilin/gamma-secretase. *Journal of Alzheimer's disease : JAD*. 25:3-28.

Harris, R.E., H.P. Larsson, and E.Y. Isacoff. 1998. A permanent ion binding site located between two gates of the Shaker K+ channel. *Biophysical journal*. 74:1808-1820.

Hasegawa, H., N. Sanjo, F. Chen, Y.J. Gu, C. Shier, A. Petit, T. Kawarai, T. Katayama, S.D. Schmidt, P.M. Mathews, G. Schmitt-Ulms, P.E. Fraser, and P. St George-Hyslop. 2004. Both the sequence and length of the C terminus of PEN-2 are critical for intermolecular interactions and function of presenilin complexes. *The Journal of biological chemistry*. 279:46455-46463.

Hermann, A., and A.L. Gorman. 1979. Blockade of voltage-dependent and Ca2+-dependent K+ current components by internal Ba2+ in molluscan pacemaker neurons. *Experientia*. 35:229-231.

Herreman, A., G. Van Gassen, M. Bentahir, O. Nyabi, K. Craessaerts, U. Mueller, W. Annaert, and B. De Strooper. 2003. gamma-Secretase activity requires the presenilin-dependent trafficking of nicastrin through the Golgi apparatus but not its complex glycosylation. *Journal of cell science*. 116:1127-1136.

Hille, B. 1973. Potassium channels in myelinated nerve. Selective permeability to small cations. *The Journal of general physiology*. 61:669-686.

Hille, B. 2001. Ion channels of excitable membranes. 3rd.ed. Sinauer, Sunderland, Mass. xviii, 814 p. pp.

Hille, B., and W. Schwarz. 1978. Potassium channels as multi-ion single-file pores. *The Journal of general physiology*. 72:409-442.

Holmes, O., S. Paturi, D.J. Selkoe, and M.S. Wolfe. 2014. Pen-2 is essential for gamma-secretase complex stability and trafficking but partially dispensable for endoproteolysis. *Biochemistry*. 53:4393-4406.
Jiang, Y., A. Lee, J. Chen, M. Cadene, B.T. Chait, and R. MacKinnon. 2002. Crystal structure and mechanism of a calcium-gated potassium channel. *Nature*. 417:515-522.
Jiang, Y., and R. MacKinnon. 2000. The barium site in a potassium channel by x-ray crystallography. *The Journal of general physiology*. 115:269-272.
Jurisch-Yaksi, N., R. Sannerud, and W. Annaert. 2013. A fast growing spectrum of biological functions of gamma-secretase in development and disease. *Biochimica et biophysica acta*. 1828:2815-2827.
Kaupp, U.B., and R. Seifert. 2002. Cyclic nucleotide-gated ion channels. *Physiological reviews*. 82:769-824.
Kimberly, W.T., M.J. LaVoie, B.L. Ostaszewski, W. Ye, M.S. Wolfe, and D.J. Selkoe. 2002. Complex N-linked glycosylated nicastrin associates with active gamma-secretase and undergoes tight cellular regulation. *The Journal of biological chemistry*. 277:35113-35117.
Kleywegt, G.J., and T.A. Jones. 1996. xdlMAPMAN and xdlDATAMAN - programs for reformatting, analysis and manipulation of biomacromolecular electron-density maps and reflection data sets. *Acta Crystallogr D Biol Crystallogr*. 52:826-828.
Kong, C., W. Zeng, S. Ye, L. Chen, D.B. Sauer, Y. Lam, M.G. Derebe, and Y. Jiang. 2012. Distinct gating mechanisms revealed by the structures of a multi-ligand gated K(+) channel. *eLife*. 1:e00184.
Kroos, L., and Y. Akiyama. 2013. Biochemical and structural insights into intramembrane metalloprotease mechanisms. *Biochimica et biophysica acta*. 1828:2873-2885.
Lai, M.T., E. Chen, M.C. Crouthamel, J. DiMuzio-Mower, M. Xu, Q. Huang, E. Price, R.B. Register, X.P. Shi, D.B. Donoviel, A. Bernstein, D. Hazuda, S.J. Gardell, and Y.M. Li. 2003. Presenilin-1 and presenilin-2 exhibit distinct yet overlapping gamma-secretase activities. *The Journal of biological chemistry*. 278:22475-22481.
Lam, Y.L., W. Zeng, D.B. Sauer, and Y. Jiang. 2014. The conserved potassium channel filter can have distinct ion binding profiles: structural analysis of rubidium, cesium, and barium binding in NaK2K. *The Journal of general physiology*. 144:181-192.
LaPorte, S.L., Z.S. Juo, J. Vaclavikova, L.A. Colf, X. Qi, N.M. Heller, A.D. Keegan, and K.C. Garcia. 2008. Molecular and structural basis of cytokine receptor pleiotropy in the interleukin-4/13 system. *Cell*. 132:259-272.

LaVoie, M.J., P.C. Fraering, B.L. Ostaszewski, W. Ye, W.T. Kimberly, M.S. Wolfe, and D.J. Selkoe. 2003. Assembly of the gamma-secretase complex involves early formation of an intermediate subcomplex of Aph-1 and nicastrin. *The Journal of biological chemistry*. 278:37213-37222.

Lazarov, V.K., P.C. Fraering, W. Ye, M.S. Wolfe, D.J. Selkoe, and H. Li. 2006. Electron microscopic structure of purified, active gamma-secretase reveals an aqueous intramembrane chamber and two pores. *Proceedings of the National Academy of Sciences of the United States of America*. 103:6889-6894.

Lemberg, M.K., and M. Freeman. 2007. Cutting proteins within lipid bilayers: rhomboid structure and mechanism. *Molecular cell*. 28:930-940.

Lemieux, M.J., S.J. Fischer, M.M. Cherney, K.S. Bateman, and M.N. James. 2007. The crystal structure of the rhomboid peptidase from Haemophilus influenzae provides insight into intramembrane proteolysis. *Proceedings of the National Academy of Sciences of the United States of America*. 104:750-754.

Li, X., S. Dang, C. Yan, X. Gong, J. Wang, and Y. Shi. 2013. Structure of a presenilin family intramembrane aspartate protease. *Nature*. 493:56-61.

Li, Y., I. Berke, L. Chen, and Y. Jiang. 2007. Gating and inward rectifying properties of the MthK K+ channel with and without the gating ring. *The Journal of general physiology*. 129:109-120.

Lockless, S.W., M. Zhou, and R. MacKinnon. 2007. Structural and thermodynamic properties of selective ion binding in a K+ channel. *PLoS biology*. 5:e121.

Lu, P., X.C. Bai, D. Ma, T. Xie, C. Yan, L. Sun, G. Yang, Y. Zhao, R. Zhou, S.H. Scheres, and Y. Shi. 2014. Three-dimensional structure of human gamma-secretase. *Nature*. 512:166-170.

Ma, W. 2011. Roles of Ca2+ and cyclic nucleotide gated channel in plant innate immunity. *Plant science : an international journal of experimental plant biology*. 181:342-346.

Malmivuo, J., and R. Plonsey. 1995. Bioelectromagnetism : principles and applications of bioelectric and biomagnetic fields. Oxford University Press, New York. xxii, 482 p. pp.

Miller, C. 2000. An overview of the potassium channel family. *Genome biology*. 1:REVIEWS0004.

Miller, D.J. 2004. Sydney Ringer; physiological saline, calcium and the contraction of the heart. *The Journal of physiology*. 555:585-587.

Moeder, W., W. Urquhart, H. Ung, and K. Yoshioka. 2011. The role of cyclic nucleotide-gated ion channels in plant immunity. *Molecular plant*. 4:442-452.

Morais-Cabral, J.H., Y. Zhou, and R. MacKinnon. 2001. Energetic optimization of ion conduction rate by the K+ selectivity filter. *Nature*. 414:37-42.

Nakamura, T. 2000. Cellular and molecular constituents of olfactory sensation in vertebrates. *Comparative biochemistry and physiology. Part A, Molecular & integrative physiology*. 126:17-32.

Neyton, J., and C. Miller. 1988a. Discrete Ba2+ block as a probe of ion occupancy and pore structure in the high-conductance Ca2+ -activated K+ channel. *The Journal of general physiology*. 92:569-586.

Neyton, J., and C. Miller. 1988b. Potassium blocks barium permeation through a calcium-activated potassium channel. *The Journal of general physiology*. 92:549-567.

Niimura, M., N. Isoo, N. Takasugi, M. Tsuruoka, K. Ui-Tei, K. Saigo, Y. Morohashi, T. Tomita, and T. Iwatsubo. 2005. Aph-1 contributes to the stabilization and trafficking of the gamma-secretase complex through mechanisms involving intermolecular and intramolecular interactions. *The Journal of biological chemistry*. 280:12967-12975.

Noskov, S.Y., S. Berneche, and B. Roux. 2004. Control of ion selectivity in potassium channels by electrostatic and dynamic properties of carbonyl ligands. *Nature*. 431:830-834.

Noskov, S.Y., and B. Roux. 2007. Importance of hydration and dynamics on the selectivity of the KcsA and NaK channels. *The Journal of general physiology*. 129:135-143.

Ogura, T., K. Mio, I. Hayashi, H. Miyashita, R. Fukuda, R. Kopan, T. Kodama, T. Hamakubo, T. Iwatsubo, T. Tomita, and C. Sato. 2006. Three-dimensional structure of the gamma-secretase complex. *Biochemical and biophysical research communications*. 343:525-534.

Osenkowski, P., H. Li, W. Ye, D. Li, L. Aeschbach, P.C. Fraering, M.S. Wolfe, D.J. Selkoe, and H. Li. 2009. Cryoelectron microscopy structure of purified gamma-secretase at 12 A resolution. *Journal of molecular biology*. 385:642-652.

Otwinowski, Z., and W. Minor. 1997. Processing of X-ray diffraction data collected in oscillation mode. *Methods Enzymology*. 276:307-326.

Pardossi-Piquard, R., S.P. Yang, S. Kanemoto, Y. Gu, F. Chen, C. Bohm, J. Sevalle, T. Li, P.C. Wong, F. Checler, G. Schmitt-Ulms, P. St George-Hyslop, and P.E. Fraser. 2009. APH1 polar transmembrane residues regulate the assembly and activity of presenilin complexes. *The Journal of biological chemistry*. 284:16298-16307.

Patton, C., S. Thompson, and D. Epel. 2004. Some precautions in using chelators to buffer metals in biological solutions. *Cell calcium*. 35:427-431.
Piasta, K.N., D.L. Theobald, and C. Miller. 2011. Potassium-selective block of barium permeation through single KcsA channels. *The Journal of general physiology*. 138:421-436.
Picones, A., and J.I. Korenbrot. 1995. Permeability and interaction of Ca2+ with cGMP-gated ion channels differ in retinal rod and cone photoreceptors. *Biophysical journal*. 69:120-127.
Pifferi, S., A. Boccaccio, and A. Menini. 2006. Cyclic nucleotide-gated ion channels in sensory transduction. *FEBS letters*. 580:2853-2859.
Pongs, O. 1992. Molecular biology of voltage-dependent potassium channels. *Physiological reviews*. 72:S69-88.
Renzi, F., X. Zhang, W.J. Rice, C. Torres-Arancivia, Y. Gomez-Llorente, R. Diaz, K. Ahn, C. Yu, Y.M. Li, S.S. Sisodia, and I. Ubarretxena-Belandia. 2011. Structure of gamma-secretase and its trimeric pre-activation intermediate by single-particle electron microscopy. *The Journal of biological chemistry*. 286:21440-21449.
Root, M.J., and R. MacKinnon. 1993. Identification of an external divalent cation-binding site in the pore of a cGMP-activated channel. *Neuron*. 11:459-466.
Sauer, D.B., W. Zeng, J. Canty, Y. Lam, and Y. Jiang. 2013. Sodium and potassium competition in potassium-selective and non-selective channels. *Nature communications*. 4:2721.
Sauer, D.B., W. Zeng, S. Raghunathan, and Y. Jiang. 2011. Protein interactions central to stabilizing the K+ channel selectivity filter in a four-sited configuration for selective K+ permeation. *Proceedings of the National Academy of Sciences of the United States of America*. 108:16634-16639.
Schrodinger, LLC. 2010. The PyMOL Molecular Graphics System, Version 1.3r1. *In*.
Seifert, R., E. Eismann, J. Ludwig, A. Baumann, and U.B. Kaupp. 1999. Molecular determinants of a Ca2+-binding site in the pore of cyclic nucleotide-gated channels: S5/S6 segments control affinity of intrapore glutamates. *The EMBO journal*. 18:119-130.
Sepulveda, F.V., L. Pablo Cid, J. Teulon, and M.I. Niemeyer. 2015. Molecular aspects of structure, gating, and physiology of pH-sensitive background K2P and Kir K+-transport channels. *Physiological reviews*. 95:179-217.

Shah, S., S.F. Lee, K. Tabuchi, Y.H. Hao, C. Yu, Q. LaPlant, H. Ball, C.E. Dann, 3rd, T. Sudhof, and G. Yu. 2005. Nicastrin functions as a gamma-secretase-substrate receptor. *Cell*. 122:435-447.

Shannon, R. 1976. Revised effective ionic radii and systematic studies of interatomic distances in halides and chalcogenides. *Acta Crystallographica Section A*. 32:751-767.

Shirotani, K., D. Edbauer, S. Prokop, C. Haass, and H. Steiner. 2004. Identification of distinct gamma-secretase complexes with different APH-1 variants. *The Journal of biological chemistry*. 279:41340-41345.

Shrivastava, I.H., D.P. Tieleman, P.C. Biggin, and M.S. Sansom. 2002. K(+) versus Na(+) ions in a K channel selectivity filter: a simulation study. *Biophysical journal*. 83:633-645.

Sobhanifar, S., B. Schneider, F. Lohr, D. Gottstein, T. Ikeya, K. Mlynarczyk, W. Pulawski, U. Ghoshdastider, M. Kolinski, S. Filipek, P. Guntert, F. Bernhard, and V. Dotsch. 2010. Structural investigation of the C-terminal catalytic fragment of presenilin 1. *Proceedings of the National Academy of Sciences of the United States of America*. 107:9644-9649.

Spassova, M., and Z. Lu. 1999. Tuning the voltage dependence of tetraethylammonium block with permeant ions in an inward-rectifier K+ channel. *The Journal of general physiology*. 114:415-426.

Standen, N.B., and P.R. Stanfield. 1978. A potential- and time-dependent blockade of inward rectification in frog skeletal muscle fibres by barium and strontium ions. *The Journal of physiology*. 280:169-191.

Thomas, M., D. Jayatilaka, and B. Corry. 2007. The predominant role of coordination number in potassium channel selectivity. *Biophysical journal*. 93:2635-2643.

Urban, S. 2009. Making the cut: central roles of intramembrane proteolysis in pathogenic microorganisms. *Nature reviews. Microbiology*. 7:411-423.

Vergara, C., and R. Latorre. 1983. Kinetics of Ca2+-activated K+ channels from rabbit muscle incorporated into planar bilayers. Evidence for a Ca2+ and Ba2+ blockade. *The Journal of general physiology*. 82:543-568.

Wang, Y., and Y. Ha. 2007. Open-cap conformation of intramembrane protease GlpG. *Proceedings of the National Academy of Sciences of the United States of America*. 104:2098-2102.

Wang, Y., Y. Zhang, and Y. Ha. 2006. Crystal structure of a rhomboid family intramembrane protease. *Nature*. 444:179-180.

Wu, Z., N. Yan, L. Feng, A. Oberstein, H. Yan, R.P. Baker, L. Gu, P.D. Jeffrey, S. Urban, and Y. Shi. 2006. Structural analysis of a rhomboid family intramembrane protease reveals a gating mechanism for substrate entry. *Nature structural & molecular biology*. 13:1084-1091.

Xie, T., C. Yan, R. Zhou, Y. Zhao, L. Sun, G. Yang, P. Lu, D. Ma, and Y. Shi. 2014. Crystal structure of the gamma-secretase component nicastrin. *Proceedings of the National Academy of Sciences of the United States of America*. 111:13349-13354.

Yau, K.W. 1994. Cyclic nucleotide-gated channels: an expanding new family of ion channels. *Proceedings of the National Academy of Sciences of the United States of America*. 91:3481-3483.

Yau, K.W., and D.A. Baylor. 1989. Cyclic GMP-activated conductance of retinal photoreceptor cells. *Annual review of neuroscience*. 12:289-327.

Ye, S., Y. Li, and Y. Jiang. 2010. Novel insights into K+ selectivity from high-resolution structures of an open K+ channel pore. *Nature structural & molecular biology*. 17:1019-1023.

Yu, F.H., and W.A. Catterall. 2004. The VGL-chanome: a protein superfamily specialized for electrical signaling and ionic homeostasis. *Science's STKE : signal transduction knowledge environment*. 2004:re15.

Zhou, Y., J.H. Morais-Cabral, A. Kaufman, and R. MacKinnon. 2001. Chemistry of ion coordination and hydration revealed by a K+ channel-Fab complex at 2.0 A resolution. *Nature*. 414:43-48.